



# Engineering Novel Silicon-Based Functional Nanomaterials

Sugimoto, Hiroshi

---

(Degree)

博士 (工学)

(Date of Degree)

2016-03-25

(Date of Publication)

2017-03-01

(Resource Type)

doctoral thesis

(Report Number)

甲第6635号

(URL)

<https://hdl.handle.net/20.500.14094/D1006635>

※ 当コンテンツは神戸大学の学術成果です。無断複製・不正使用等を禁じます。著作権法で認められている範囲内で、適切にご利用ください。



博 士 論 文

Engineering Novel Silicon-Based  
Functional Nanomaterials

シリコンベース機能性ナノ材料の開発  
に関する研究

平成 28 年 1 月

神戸大学大学院工学研究科

杉本 泰

Doctoral Dissertation

博士論文

Engineering Novel Silicon-Based  
Functional Nanomaterials

シリコンベース機能性ナノ材料の開発に関する研究

January, 2016

平成 28 年 1 月

for the Degree of  
Doctor of Philosophy in Engineering

Graduate School of Engineering, Kobe University

神戸大学大学院工学研究科

Hiroshi Sugimoto

杉本 泰

# Abstract

This thesis focuses on the development of silicon based functional nanomaterials targeting for a variety of applications in optoelectronics and biology. The thesis consists of 9 chapters as summarized below.

In Chapter 1, we first describe the background and the motivation of this thesis. Following the introduction of colloidal semiconductor nanocrystals, we explain the remaining problems of commercially available semiconductor nanocrystals and discuss the advantages of colloidal Si nanocrystals as alternatives. Then, the recent studies on the development of colloidal Si nanocrystals aiming at further functionalities, *e. g.*, impurity doping, surface functionalization and coupling with surface plasmons, are summarized.

In Chapter 2, we develop a new type of all-inorganic colloidal Si nanocrystals, which is achieved by simultaneous doping of boron (B) and phosphorus (P). In order to fully understand the mechanism of solution-dispersibility, we first systematically study the structural properties of B and P codoped colloidal Si nanocrystals using electron microscope, X-ray photoelectron and Raman spectroscopies. We show that heavily codoping of B and P on Si nanocrystal surface results in unique properties such as excellent colloidal stability without organic surface functionalization. The codoped Si nanocrystals exhibit efficient size-controllable photoluminescence spanning visible to near-IR ranges. Chapter 3 is an extension of the work in Chapter 2. We develop a new synthetic route of codoped Si nanocrystals for the mass-production without vacuum

processes. By thermal decomposition of chemicals containing hydrogen silsesquioxane, boric acid and phosphoric acid, codoped colloidal Si nanocrystals are successfully prepared.

Chapter 4 focuses on the applications of the Si nanocrystals as fluorescent probes in bioimaging. The preparation of colloidal Si nanocrystals in water and their controlled PL properties are shown. The photoluminescence- and colloidal-stability of codoped Si nanocrystals in water with different pH are studied in detail.

In Chapter 5 and 6 for the enhanced light emission performance of Si nanocrystals, we try to synthesize Si nanocrystal-based plasmonic coupled structures and systematically investigate the photoluminescence properties. Chapter 5 focuses on the engineering of radiative decay rate of Si nanocrystals by the coupling with Au nanorods. We successfully demonstrate the enhanced emission quantum efficiency in Au nanorods decorated with Si nanocrystals. Additionally, in Chapter 6, the enhanced luminescence of Si nanocrystals embedded in cellulose nanofibers by the coupling with plasmonic nanoparticles are demonstrated. These works have been done in collaboration with the groups of Prof. Luca Dal Negro (fabrication of cellulose nanofibers) and Prof. Björn M. Reinhard (synthesis of Si nanocrystal-Au nanorod composites) at the Photonics Center in Boston University.

In Chapter 7, by extending the preparation method of codoped Si nanocrystals introduced in Chapter 2, we for the first time, present the size-controlled growth of cubic boron phosphide (BP) nanocrystals. Cubic BP is a III-V semiconductor with

zinc-blend crystal structure and known to be wide-gap (2.0 eV) indirect semiconductor. The structural and optical properties are systematically studied.

Chapter 8 focuses on development of new materials promising for Boron Neutron Capture Therapy (BNCT). By controlling Si, B and P concentrations in the preparation method of codoped Si nanocrystals, we successfully develop ternary alloy Si-B-P nanocrystals with a large content of B while maintaining solution-dispersibility and photoluminescence properties.

In Chapter 9, we summarize all the results and present a brief outlook for further study of Si-based functional nanomaterials.

# Contents

Chapter 1 General Introduction .....	1
1-1 Colloidal semiconductor nanocrystals.....	1
1-2 All-inorganic colloidal nanocrystals.....	3
1-3 Case of Colloidal Si Nanocrystals .....	5
1-4 n- or p-type Impurity Doping in Si Nanocrystals .....	8
1-5 B and P Codoped and Compensated Si Nanocrystals .....	9
1-6 Coupling with Surface Plasmon Resonance of Metal Nanostructures .....	12
1-7 Chapter Overview and Goals of This Thesis.....	15
Chapter 2 Structural and Optical Properties of All-Inorganic Colloidal Si Nanocrystals Codoped with Boron and Phosphorus .....	17
2-1 Introduction .....	17
2-2 Materials and Methods .....	18
2-3 Codoped Si nanocrystals in silicate matrices .....	21
2-4 Codoped Si nanocrystals in solution .....	23
2-5 Conclusion.....	38
Chapter 3 Synthetic Route of B and P codoped Colloidal Si Nanocrystals from Hydrogen Silsesquioxane.....	39
3-1 Introduction .....	39

3-2	Materials and Methods .....	40
3-3	Results and Discussion .....	42
3-4	Conclusions .....	52

## Chapter 4 Water-Dispersible Si Nanocrystals: Photoluminescence

Properties and Stability .....		53
4-1	Introduction .....	53
4-2	Materials and Methods .....	54
4-3	Results and Discussion .....	55
4-4	Conclusion .....	65

## Chapter 5 Plasmonic-Coupled Nanocomposites Based on Gold

Nanorods Decorated with Si Nanocrystals .....		66
5-1	Introduction .....	66
5-2	Materials and Methods .....	67
5-3	Results and Discussion .....	69
5-4	Conclusion .....	89

## Chapter 6 Enhanced Photoluminescence of Si Nanocrystals Doped

Cellulose Nanofibers .....		90
6-1	Introduction .....	90
6-2	Experimental Results .....	91
6-3	Conclusion .....	101



## Chapter 7 Size-Controlled Growth of Cubic Boron Phosphide

Nanocrystals .....	102
7-1 Introduction .....	102
7-2 Materials and Methods .....	104
7-3 Results and Discussion .....	107
7-4 Conclusions .....	117

## Chapter 8 Growth of Boron-Rich Nanocrystals from

### Oxygen-Deficient Borophosphosilicate Glasses for Boron Neutron

Capture Therapy .....	118
8-1 Introduction .....	118
8-2 Materials and Method .....	121
8-3 Results and Discussion .....	124
8-4 Conclusion .....	134

## Chapter 9 Outlook..... 136

## References..... 139

## List of Achievements ..... 159

Journal Papers .....	159
International Conferences .....	163
Patent .....	164
Award.....	165

Acknowledgements .....	166
------------------------	-----

# Chapter 1

## General Introduction

### 1-1 Colloidal semiconductor nanocrystals

Semiconductor nanocrystals with diameters smaller than twice of the exciton Bohr radius exhibit unique optical and electrical properties because of the quantum confinement effects. The electronic state structures of nanocrystals can be controlled by size, shape, composition (alloying) and surface chemistry.<sup>1</sup> Among different kinds of semiconductor nanocrystals, those dispersed in solution, *i. e.*, colloidal semiconductor nanocrystals or nanocrystal inks, are essential building blocks for the future optoelectronic devices such as solar cells, thin film transistors and light-emitting diodes (Figure 1-1).<sup>2-8</sup> Colloidal dispersion of nanocrystals is useful for the formation of thin films by a simple solution-method such as spin-coating and roll-to-roll printing without vacuum and high-temperature process. As shown in Figure 1-1 (b) and (c), the smooth films in which nanocrystals are closely packed, is obtained by controlled solution-based deposition processes and thin-film transistor is produced by using nanocrystal films (Figure 1-1 (d)). A fascinating aspect of such nanocrystal films in terms of both fundamental physics and device performances is the interaction between nanocrystals in three-dimensional arrays. In densely-packed nanocrystal films, the electronic wavefunctions overlap each other, which leads to the attractive physical phenomena by electronic coupling between nanocrystals.<sup>5</sup> For instance, fluorescence

resonant energy transfer or exciton migration, which is the non-radiative transfer of excitations, occurs by dipole-dipole interactions between neighbouring nanocrystals.<sup>9,10</sup> Furthermore, the multiple exciton generation is predicted to become more efficient in such systems than bulk semiconductor materials and thus the coupled nanocrystals are considered to be a breakthrough for the next generation solar cells with extremely high conversion efficiency.<sup>4,11</sup>

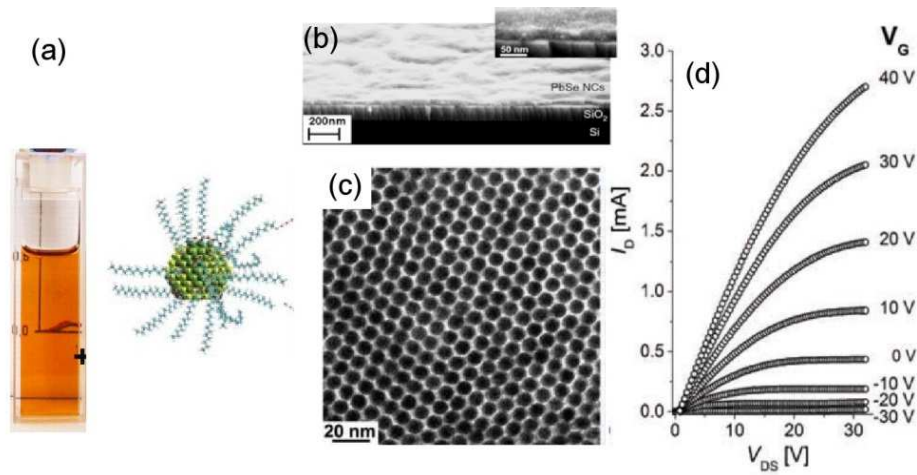


*Figure 1-1 (a) Photograph of colloidal dispersion of ligand-stabilized semiconductor nanocrystals.<sup>3</sup> (b) Scanning electron microscope image of PbSe nanocrystal film prepared by spin-coating. (c) Transmission electron microscope image of nanocrystal mono-layer. (d)  $I_D$ - $V_{DS}$  characteristic of nanocrystal thin film transistor.<sup>2</sup>*

## 1-2 All-inorganic colloidal nanocrystals

A common feature of colloidal semiconductor nanocrystals is the capping of the surface by organic molecules, which protects the surface and prevents the agglomeration by steric barriers or electrostatic repulsion. Thanks to the absence of agglomeration, high-quality nanocrystal films can be formed just by simple coating and printing processes. However, these surface ligands are typically very long carbon chains ( $C > 8$ : more than 1 nm),<sup>12</sup> which act as insulating tunneling barriers between nanocrystals and significantly degrade the electrical transport properties.<sup>13</sup> Moreover, since in many cases, colloidal nanocrystals are prepared in nonpolar solvents using long organic chains, they are not dispersible in water and thus inapplicable to the bioimaging and biosensing.

These problems have been known as “ligand problem” and there have been numerous efforts to create the nanocrystal films with narrowed barriers between nanocrystals (see Figure 1-2).<sup>13,14</sup> An approach is to exchange the long ligands with shorter ones that improve the carrier transport between nanocrystals.<sup>14</sup> Talapin *et al.*, have pioneered the use of inorganic ligands instead of organic ligands.<sup>15,16</sup> Such new class of materials are called “all-inorganic nanocrystals”, in which the surface of nanocrystals is capped with chalcogenides ( $S^{2-}$ ,  $Se^{2-}$ ,  $Te^{2-}$ )<sup>15</sup> and metal chalcogenides ( $Sn_2S_6^{4-}$ ,  $In_2Se_4^{2-}$ ).<sup>16</sup> In addition, Kagan and Murray group synthesized nanocrystals capped with ammonium thiocyanate ( $NH_4SCN$ ).<sup>17</sup> As shown in the transmission electron microscope image in Figure 1-2 (a), the distance between nanocrystals is apparently reduced after the

ligand-exchange. The inorganic ligand-capped nanocrystals ensure a higher conductivity of the nanocrystal solids and a band-like transport between atomic-ligand-passivated nanocrystals is reported.<sup>16</sup> As a result, electron mobility as high as  $16 \text{ cm}^2 \text{V}^{-1} \text{S}^{-1}$  is achieved in nanocrystal solids.<sup>16</sup>

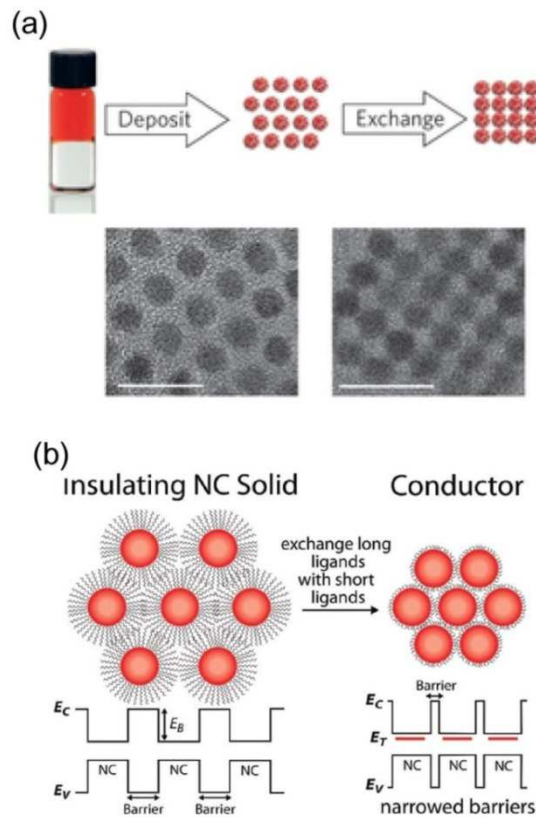


Figure 1-2 (a) Schematic of synthesized 3.9 nm CdSe nanocrystals dispersed in the hexane phase of a biphasic solution with dimethylsulphoxide, followed by nanocrystal deposition and solid-state exchange. TEM images of 6 nm PbSe QD films before (left) and after (right) solid-state exchange of long-chain with thiocyanate ligands (Scale bars: 20 nm).<sup>14</sup> (b) Surface treatment effects on colloidal nanocrystal films: Long-chain ligands are replaced with short chain ligands to produce a conductive film by decreasing the inter nanocrystal distance.<sup>13</sup>

### 1-3 Case of Colloidal Si Nanocrystals

Up to now, the scope was the progress in the research of “colloidal” form nanocrystals. Here we go into the material choice for consumer optoelectronic and biomedical applications. The great advancement mentioned in the previous section has been made in cadmium (Cd)- and lead (Pb)-chalcogenide nanocrystals. However, the toxicity of these nanocrystals systems raises concerns for the applications in biology and consumer optoelectronic devices and then demands focused efforts aimed at developing alternative solutions.

Silicon (Si) nanocrystals are the most promising alternatives to toxic Cd- and Pb chalcogenide nanocrystals because of their compatibility with biological substances and the well-established Si electronic device technology. Since the discovery of room-temperature visible emission from porous Si in 1990,<sup>18</sup> there have been a tremendous number of papers on the structural and photoluminescence (PL) properties of Si nanostructures in solid systems. The focused efforts on PL properties revealed that the radiative recombination of quantum-confined excitons in Si nanostructures enabled them to exhibit PL in the visible to near-IR range.<sup>19–22</sup>

Despite the numerous reports on Si nanocrystals in solid matrices, the development of “colloidal” Si nanocrystals had been challenging because the solution synthesis of Si nanocrystals is in principle difficult due to the covalent bond nature. It is only recently that the quality of colloidal Si nanocrystals has been improved in terms of

crystallinity, size distribution, high stability in solution and high luminescence quantum yield.

The group of J. Veinot in University of Alberta reported size-controlled synthesis of Si nanocrystals embedded in  $\text{SiO}_2$  by thermal decomposition of hydrogen silsesquioxane (Figure 1-3 (a)).<sup>23</sup> By hydrofluoric acid etching, hydride Si nanocrystals are liberated in solution and passivated by organic molecules to obtain the colloidal dispersion (Figure 1-3 (b)). The nanocrystal size can be controlled by the temperature of thermal treatment before etching. G. Ozin and co-workers developed the size-separated colloidal Si nanocrystals by density gradient precipitation technique,<sup>24</sup> which show efficient (QY ~40%) emission spanning red to near-IR range (Figure 1-3 (c)). Kortshagen and co-workers also reported colloidal Si nanocrystals with a high quantum yields synthesized by non-thermal plasma.<sup>25</sup>

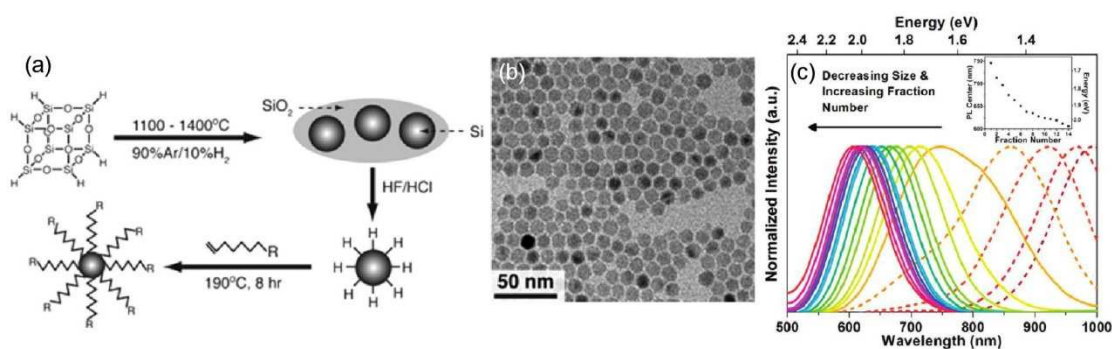


Figure 1-3 (a) Synthesis of Si nanocrystals from HSQ.<sup>23</sup> (b) TEM image of ligand-stabilized Si nanocrystals prepared in (a).<sup>23</sup> (c) Photoluminescence spectra of size-separated colloidal Si nanocrystals.<sup>24</sup>



In the past decade, the quality of colloidal Si nanocrystals is rapidly catching up with that of II-VI and IV-VI compound semiconductors. For further development of the functionality in a variety of application, in the following sections, the way to enhance and control the functionality of Si nanocrystals, which is the main goal of this thesis, will be introduced.

## 1-4 n- or p-type Impurity Doping in Si Nanocrystals

The electrical property of semiconductor is precisely controlled in a very wide range by shallow impurity doping and this is the basis of modern Si-based semiconductor technology.<sup>26</sup> In bulk Si, the n- (phosphorus (P), arsenic (As)) or p-type (boron (B)) doping results in the generation of charge carriers, which enables us to control the electrical transport properties very precisely. This scenario can be also applied to Si nanocrystals and the technology to control the charge carriers in nanocrystals is indispensable for the application in electronic devices. Since the number of Si atoms per sub 10 nm size nanocrystal is in the range of 100–10000, an impurity atom corresponds to a very high doping level ( $>10^{18}$  /cm<sup>3</sup>). The effect of B or P doping in Si nanocrystals has been studied by PL,<sup>27–29</sup> electron paramagnetic resonance (EPR),<sup>30–32</sup> and Raman spectroscopy.<sup>33–35</sup> It was found that B or P doping quenches the PL by the Auger process between photoexcited carries and those provided by doping.<sup>27–29</sup> Pi *et al.*<sup>29</sup> assigned preferential doping sites of P or B in *in situ* doped plasma-synthesized Si nanocrystals from the analysis of PL data. The doping site of P was also studied by atom probe tomography.<sup>36</sup> In our group,<sup>30</sup> we studied the hyper-fine structure of EPR spectra of P-doped Si nanocrystals in glass matrices and demonstrated the evidence of the quantum confinement of donors in nanocrystals. Pereira and co-workers<sup>31,37</sup> studied P-doped Si nanocrystals powder by EPR spectroscopy and demonstrated that doping efficiency of Si nanocrystals decreases significantly when the diameter is smaller than 10 nm. Recently, the electrical transport properties and free-carrier absorption by B and P doping are systematically studied by the group of Kortshagen

and Nozaki.<sup>38-40</sup> They successfully demonstrated the presence of charge carriers in Si nanocrystals.<sup>38-40</sup>

## 1-5 B and P Codoped and Compensated Si Nanocrystals

The research in our group in the past decade has provided new fascinating features of doping in Si nanocrystals.<sup>41-44</sup> One of the most important findings was that PL properties of Si nanocrystals can be modified drastically by simultaneously doping B and P. Figure 1-4 (a) shows the PL spectra of B and P codoped Si nanocrystals embedded in silicate films.<sup>41</sup> The PL peak shifts to lower energy as P concentration increases and is located below bulk Si bandgap in codoped Si nanocrystals. The low-energy PL can be assigned to the radiative transitions between donor and acceptor states introduced by B and P codoping.<sup>42</sup> In addition, the PL intensity of codoped Si nanocrystals is larger than that of B-doped Si nanocrystals. Figure 1-4 (b) shows the absorption coefficient of doped Si nanocrystals in the near infrared range, which demonstrates the decrease of free-carrier absorption at longer wavelength by codoping. This is a signature of the compensation of excess carriers by codoping and explains increased PL intensity in codoped Si nanocrystals compared to that of B or P singly doped ones.

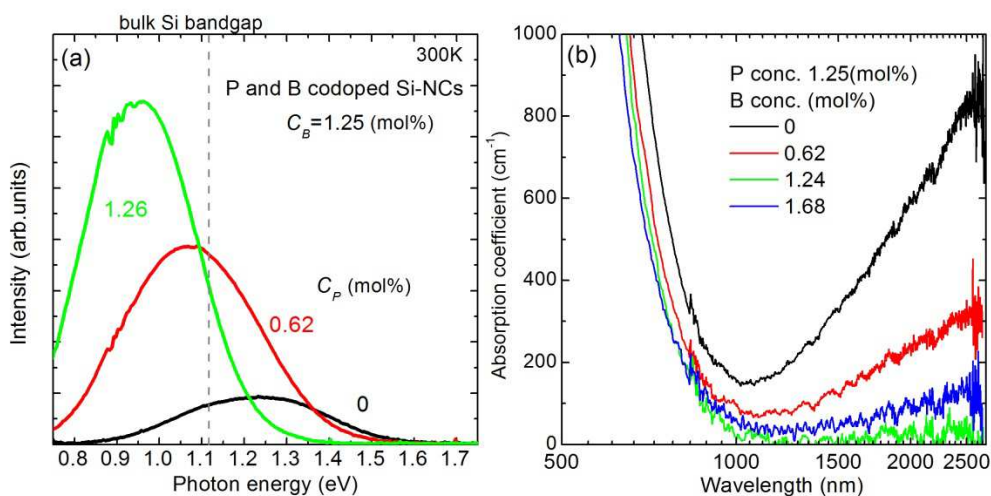


Figure 1-4. (a) PL spectra and (b) Absorption coefficient of B and P codoped Si nanocrystals in silicate film with different nominal concentrations of B and P.

Ossicini and co-workers studied the codoped nanocrystals by first principle calculations.<sup>45,46</sup> Figure 1-5 displays the formation energies, which demonstrate that the codoping drastically decreases the formation energy compared to that of nanocrystals doped with either B or P.<sup>45</sup> This means that the compensated nanocrystals are preferably formed, which is consistent with the discussion above. They also demonstrated that the formation of donor and acceptor states by codoping shrinks the gap energy between the highest occupied molecular orbitals (HOMO) to the lowest unoccupied molecular orbitals (LUMO), resulting in the lower-energy shift of the luminescence.<sup>45</sup>

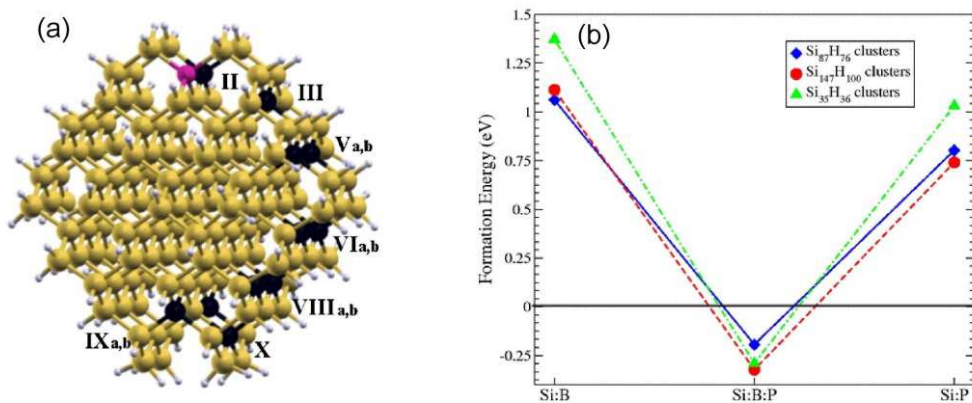


Figure 1-5. (a) Model of B and P codoped Si nanocrystal ( $\text{Si}_{145}$  (yellow balls) B (magenta) P (black)  $\text{H}_{100}$  (gray)). (b) Formation energy for single-doped and codoped Si nanocrystals. In the codoped nanocrystals, the impurities are placed as second neighbors in the first subsurface shell (P is located at II in (a)).<sup>45</sup>

Another important feature and unexpected effect of codoping is that it modifies the chemical properties of Si nanocrystals drastically. Codoped Si nanocrystals can form a stable colloidal dispersion in alcohol without any the surface functionalization processes.<sup>44</sup> These unusual properties provided by B and P codoping offer a new opportunity to further explore the functionalities of Si nanocrystals, which leverage the nanoscale Si-based optoelectronic applications. In fact, B and P codoped colloidal Si nanocrystals are the main cast of this work.

## 1-6 Coupling with Surface Plasmon Resonance of Metal

### Nanostructures

Luminescent Si nanocrystals are promising candidates as light-sources in optoelectronic devices and nanoprobe in bioimaging. For such applications, a highly efficient PL is crucial. The PL efficiency is determined by the absorption cross-section and the quantum yield. Unfortunately, Si nanocrystals intrinsically have small absorption cross-section. Furthermore, the radiative decay rate is much smaller than those of direct band gap semiconductors, which often results in low quantum yield. A promising approach to overcome these problems is utilizing the enhanced local-field in the vicinity of metal nanostructures. It is well known that the excitation efficiency is strongly enhanced when an emitter is located nearby metal nanostructures exhibiting localized surface plasmon resonance (LSPR) *i. e.*, plasmonic nanostructures.<sup>47</sup> In addition, the plasmonic nanostructures acting as nano-antennas results in an increase of the photonic density of states (PDOS) which leads to the enhancement of the radiative decay rate of antenna-coupled emitters. This coupling effect boosts the quantum efficiency by overcoming the fast relaxation into non-radiative decay channels.<sup>48</sup>

Plasmonic nanostructures including nanospheres, nanorods, nanodisks and their arrays have been tailored to control the PL properties of semiconductor nanocrystals.<sup>47,49</sup> A significant luminescence enhancement has been previously demonstrated utilizing LSPR of metal nanostructures. The combination of plasmonic nanoparticles and nanoscale emitters into a single multifunctional colloidal platform has a large potential

for engineering novel active devices for biosensing and bioimaging.<sup>50-52</sup> Plasmon-enhanced emission of nanocrystals with Au nanoshell,<sup>50</sup> DNA-linked Au nanoparticles-nanocrystals hybrid structures,<sup>53</sup> and Au nanorods coupled to nanocrystals<sup>54,55</sup> in aqueous solutions have been demonstrated (see Figure 1-6).

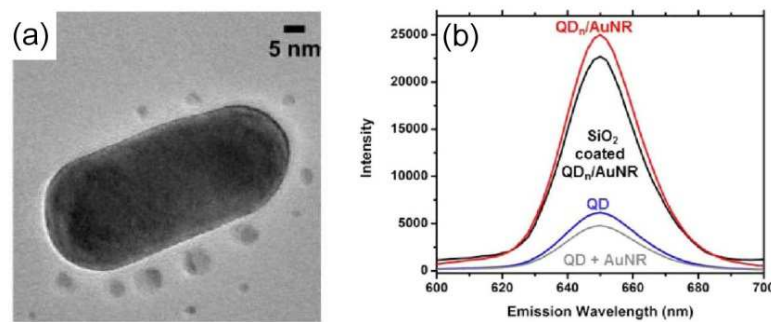


*Figure 1-6 (a) Gold nanorod-QD composites. (b) Emission enhancement in composites.<sup>55</sup>*

Plasmonic-coupled PL of Si nanocrystals embedded in solid matrices has been widely investigated in the past decade.<sup>56-60</sup> In 2005 Atwater and co-workers have demonstrated the quantum efficiency enhancement of Si nanocrystals by the coupling with nanoporous Au.<sup>56</sup> Figure 1-7 shows the sample structure and enhanced PL intensity of Si nanocrystals in SiO<sub>2</sub>. By controlling and optimizing the spacer thickness, they successfully demonstrated that utilizing localized surface plasmon resonance is a promising way to enhance the emission rate and quantum efficiency of Si nanocrystals.

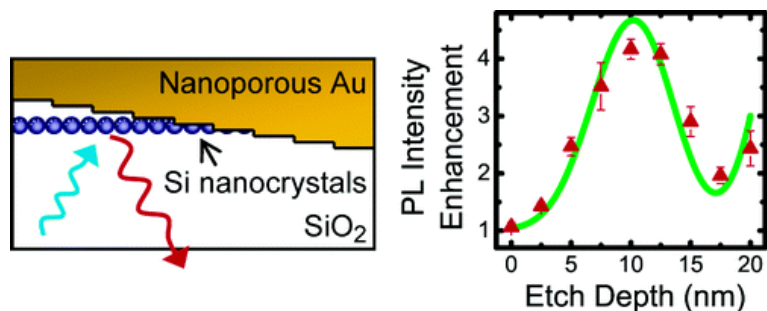


*Figure 1-7 Solid state system for plasmon-enhanced silicon nanocrystal emission. (Left) Sample structure of Si nanocrystals embedded in SiO<sub>2</sub> with nanoporous Au film. (Right) PL intensity enhancement measured at 780 nm as a function of etch depth.<sup>56</sup>*

In contrast to Si nanocrystals embedded in solid matrices, colloidal Si nanocrystals coupled to plasmons have been scarcely studied in spite of their importance in applications such as in-vivo bioimaging<sup>61</sup> and printable optoelectronics.<sup>25,62</sup> The development of such systems is still challenging due to the difficulty of synthesizing high quality Si nanocrystals with bright emission in biological transparent windows (700–1200 nm) and high colloidal stability in aqueous solution.<sup>63,64</sup>



## 1-7 Chapter Overview and Goals of This Thesis

The following chapters will focus on the development of different types of Si-based nanomaterials targeting for a variety of applications in optoelectronics and biology.

As introduced in section 1–5, we have found that the B and P codoped Si nanocrystals can be dispersed in alcohol without any surface functionalization, and exhibit luminescence in the near-IR range. Therefore, the codoped nanocrystals are highly promising for the applications in printable optoelectronics and biology. In Chapter 2, to clarify the mechanism of solution-dispersibility, we first study the structural properties of B and P codoped colloidal Si nanocrystals in detail. We show that the formation of surface shell consisting of heavily B and P codoped crystalline Si, which results in unique properties such as high-chemical stability and excellent colloidal stability without organic surface functionalization. Moreover, the overview of optical properties of codoped Si nanocrystals with different size is described. The codoped Si nanocrystals exhibit efficient photoluminescence spanning visible to near-IR ranges, depending on their average sizes. Chapter 3 is an extension of the work in Chapter 2. We show the synthetic route of codoped Si nanocrystals for mass-production without vacuum processes using molecular precursors.

Chapter 4 focuses on the potential of Si nanocrystals as fluorescent probes in bioimaging. The preparation of colloidal Si nanocrystals in water and their controlled PL properties are shown. The photo-stability and pH dependence of PL intensity and dynamics are systematically investigated.

In Chapter 5 and 6 for the enhanced light emission performance of Si nanocrystals, we synthesize Si nanocrystal-based plasmonic coupled composites and systematically investigate the PL properties such as PL decay dynamics, polarization and excitation spectra. The enhanced PL of Si nanocrystals by the coupling with plasmonic nanoparticles are demonstrated in different systems. This work has been performed partially in collaboration with the groups of Prof. Luca Dal Negro and Prof. Björn M. Reinhard at the Photonics Center in Boston University.

Another important feature of codoped Si nanocrystals is that they contain a large amount of B and P atoms per nanocrystal. This makes them very promising for applications such as Boron Neutron Capture Therapy (BNCT). In Chapter 7, by extending the preparation method of codoped Si nanocrystals introduced in Chapter 2, we demonstrate the size-controlled growth of cubic boron phosphide nanocrystals. Chapter 8 focuses on development of new materials promising for BNCT and thus we develop ternary alloy Si-B-P nanocrystals with a large content of B while maintaining solution-dispersibility and photoluminescence properties.

In Chapter 9, we summarize all the results and present a brief outlook for further study of Si-based functional nanomaterials.

## Chapter 2

# Structural and Optical Properties of All-Inorganic Colloidal Si Nanocrystals Codoped with Boron and Phosphorus

Adapted from *H. Sugimoto, et al., J. Phys. Chem. C, 116, 17969–17975 (2012)*

*H. Sugimoto, et al., J. Phys. Chem. C 117, 11850-11857 (2013)*

*H. Sugimoto, et al., J. Phys. Chem. C 117, 6807-6813 (2013)*

*M. Fujii, et al., J. Appl. Phys. 115,084301 (2014)*

### 2-1 Introduction

For the formation of conductive solution-processed nanocrystal films, all-inorganic colloidal nanocrystals have been developed in metal chalcogenides by exchanging organic-ligands with inorganic atomic ligands.<sup>15</sup> Unfortunately, ligand exchange technique is not successfully applied to Si nanocrystals because Si forms covalent bonds (Si-C) with organic ligands. Since Si is very environmentally friendly and is an extensively used semiconductor, the development of inorganic ligand-capped Si nanocrystals is a very important research topic.

In 2011, we have introduced a new type of all-inorganic colloidal Si nanocrystals, which are achieved by heavily boron (B) and phosphorus (P) codoping in Si nanocrystals.<sup>44</sup> However, the mechanism of dispersibility is still unclear. In this

section, we comprehensively study the structural and optical properties of B and P codoped Si nanocrystals.

## 2-2 Materials and Methods

The preparation procedure of colloidal dispersion of P and B codoped Si nanocrystals is summarized in Figure 2-1. Si-rich borophosphosilicate glass (BPSG) films with thickness of 10–20  $\mu\text{m}$  were first deposited on thin stainless steel plates (0.1 mm in thickness) by cosputtering Si,  $\text{SiO}_2$ ,  $\text{B}_2\text{O}_3$ , and  $\text{P}_2\text{O}_5$  in an rf-sputtering apparatus. The films peeled from the plates were annealed at different temperatures (850–1300°C) in a  $\text{N}_2$  gas atmosphere for 30 min to grow Si nanocrystals with different sizes in BPSG matrices. During the growth of Si nanocrystals, P and B atoms are incorporated into Si nanocrystals from BPSG matrices, or precipitate the interface between Si nanocrystals and glass matrices. It is well-known that this effect takes place at the interface of between borosilicate glass (BSG) and bulk Si when heavily doped BSG is removed by HF etching. Annealed films were then grounded in a mortar to obtain fine powders. Codoped Si nanocrystals were isolated from BPSG matrices by etching in HF solutions (46 wt %) for 1 hour. Isolated Si nanocrystals were separated from the HF solution by centrifugation (4000 rpm, 1 min) in an ultrafiltration concentrator (VS0232: Sartorius Stedim Biotech GmbH), and Si nanocrystal powder was obtained in the concentrator. The powder of Si nanocrystals was then redispersed by adding methanol and simply shaking the vial. A part of nanocrystals aggregates after a little while (<10% at an

optimized preparation condition), which can be removed by centrifugation (4000 rpm, 3 min).

Transmission-electron microscope (TEM) observations (JEM-2010, JEOL) were performed by dropping the solution on carbon-coated TEM meshes. Z-contrast high-angle annular dark-field (HAADF) images and electron energy loss spectroscopy (EELS) mappings are obtained using scanning TEM (Hitachi, HD2700). Raman spectra were measured using a confocal microscope (50 $\times$  objective lens, NA = 0.8) equipped with a single monochromator and a CCD. The excitation source was a 514.5 nm line of an Ar ion laser (1 mW). The excitation power was fixed to 1 mW for all samples. We confirmed that the laser excitation with 1 mW does not affect the structure of nanocrystals. X-ray photoelectron spectroscopy (XPS) measurements (PHI X-tool, ULVAC-PHI) were carried out using an Al K $\alpha$  X-ray source. The samples for Raman scattering and XPS measurements were prepared by drop-coating nanocrystal solution on gold-coated Si wafers. Photoluminescence spectra were obtained by using a single spectrometer equipped with a liquid-N<sub>2</sub> cooled InGaAs diode array (OMA-V-SE, Roper Scientific) and a Si:CCD (Roper Scientific). The excitation wavelength was 405 nm. The spectral response of the detection system was corrected with the reference spectrum of a standard halogen lamp. PL spectra were also measured using a spectrofluorometer (Fluorolog-3, HORIBA Jovin Yvon) equipped with a photomultiplier (500-850 nm) and an InGaAs photodiode (800-1300 nm) as detectors. The PL spectra obtained by two different detectors are merged after corrected the sensitivity. The correction factors were obtained by measuring the reference spectrum of a standard halogen lamp. The excitation source was a monochromatized Xe lamp (405 or 450 nm). The PL QY was

determined by a comparative method.<sup>65</sup> Rhodamine 6G in water with a QY of 95% was used as a reference solution. The QY of a sample ( $Q_s$ ) is calculated from PL spectra of reference and colloidal Si nanocrystal samples obtained in the same condition using,  $Q_s = Q_R (I_S \times A_R \times n_S^2) / (I_R \times A_S \times n_R^2)$ , where  $Q$  is the quantum yield,  $I$  is the integrated PL intensity,  $A$  is the absorbance, and  $n$  is the refractive index. The subscript S and R refer to the sample and the reference solutions, respectively. In order to minimize an error due to nonuniform irradiation of solution, the sample solutions are diluted to keep the absorbance below 0.1. The error of QY values estimated from the measurements of series of diluted samples at several different excitation wavelengths was around  $\pm 12\%$ . PL decay dynamics were measured by using a near IR photomultiplier (R5509-72, Hamamatsu Photonics) and a multi-channel scalar (SR430, Stanford Research). The excitation source was modulated 405 nm light. All the measurements were carried out at room temperature.

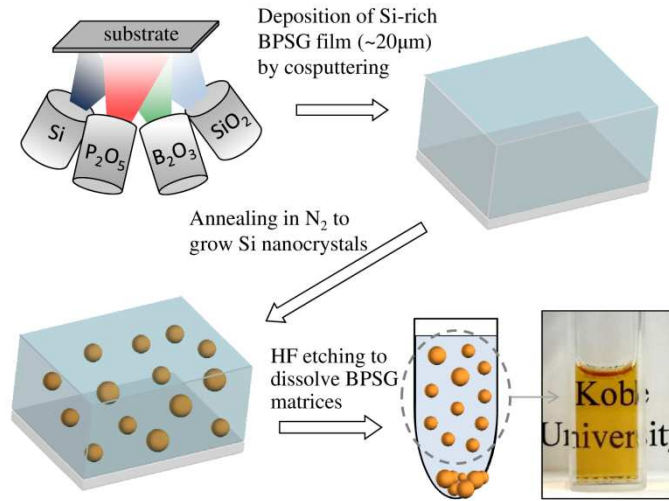


Figure 2-1. Preparation procedure of colloidal dispersion of P and B codoped colloidal Si nanocrystals

### 2-3 Codoped Si nanocrystals in silicate matrices

We first characterize the PL properties of annealed samples before HF etching, *i.e.*, Si nanocrystals or nanoclusters in BPSG, annealed at different temperatures (850–1250°C). Figure 2-2 (a) shows normalized PL spectra of codoped samples annealed at different temperatures. The spectra depend strongly on annealing temperature. The PL peak energies and intensities are plotted in Figure 2-2 (b) as a function of annealing temperatures. We can see the shift of the PL peak in a very wide range by changing annealing temperature. The most remarkable feature in Figure 2-2 is that the PL peak energy is located below the bulk Si band gap (1.12 eV) when annealing temperature is higher than 1100°C. Such a low energy PL cannot be observed in

undoped Si nanocrystals at room temperature and the observation of the below bulk-band gap PL is one of the evidences that the PL arises from the transitions between donor and acceptor states. In Figure 2-2, we find that the PL intensity also strongly depends on annealing temperature. Especially, the PL intensity drastically decreases at high annealing temperature. We will discuss the mechanism later.

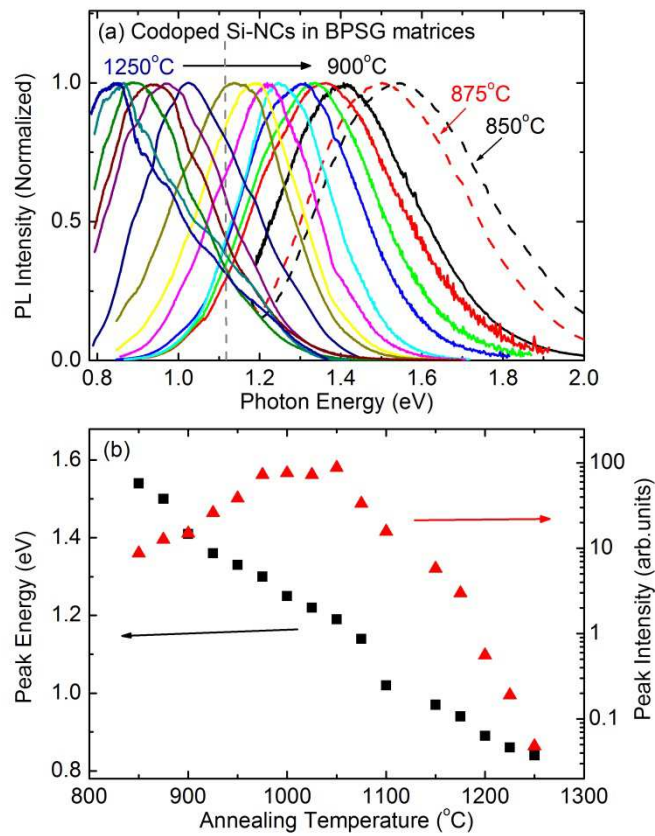


Figure 2-2. (a) PL spectra of codoped Si nanocrystals embedded in silicate matrices annealed at different temperatures. (b) PL peak energy and intensity as a function of annealing temperatures.



## 2-4 Codoped Si nanocrystals in solution

### A. Structural properties

We first discuss the relation between B and P codoping and solution-dispersibility. Figure 2-3 shows the photographs of colloidal Si nanocrystals prepared from Si-rich BPSG films with different P and B concentrations. The abscissa and ordinate of Figure 2-3 represent B and P concentrations, respectively, in as-deposited Si-rich BPSG films. The P concentration is determined by energy dispersive x-ray spectroscopy (EDS) and the B concentration is obtained from the intensity ratio of Si–O–Si and B–O vibration modes in IR absorption spectra.<sup>66</sup> The photographs of the dispersions after removing precipitates by centrifugation are shown. The color of the solution depends strongly on sample preparation parameters. Note that the amount of Si nanocrystal-doped BPSG films dissolved in HF is the same for all samples. Therefore, dense color implies that a large fraction of Si nanocrystals contributing the visible light absorption are dispersed in solution. On the other hand, light color means that majority of Si nanocrystals are precipitated and removed by centrifugation. Below the photographs in Figure 2-3, the amounts of Si nanocrystals in the solutions obtained by inductively coupled plasma atomic emission spectrometry (ICP-AES) measurements are shown. In undoped Si nanocrystals (sample H), the solution is colorless and Si is not detected in ICP-AES. Therefore, undoped Si nanocrystals are not dispersed in polar liquids. This is consistent with previous reports. Similarly, in P (sample G) and B (sample I) singly-doped samples, Si is not detected in ICP-AES and the solutions are colorless. In contrast to these

samples, P and B codoped samples (samples A-F) are brownish. The color becomes dense and the amount of Si in solution increases with increasing P and B concentrations. In the darkest solution (sample D), Si concentration is 453  $\mu\text{g/ml}$ . Figure 2-3 demonstrates that codoping of P and B is essential to achieve high solution dispersibility.

In Figure 2-3, P and B concentrations in colloidal Si nanocrystals obtained by ICP-AES measurements are also shown below the photographs. We can see that the P and B concentrations, especially the B concentrations, are very high. They are much higher than those in Si-rich BPSG films before etching (see abscissa and ordinate in Figure 2-3). The difference in the P and B concentrations between Si nanocrystals in solution and Si-rich BPSG films before etching indicates that P and B atoms are accumulated in or on the surface of Si nanocrystals during the growth of Si nanocrystals by annealing. The P and B concentrations in colloidal Si nanocrystals are also much higher than the solid solubility limits of P and B in bulk Si crystal.

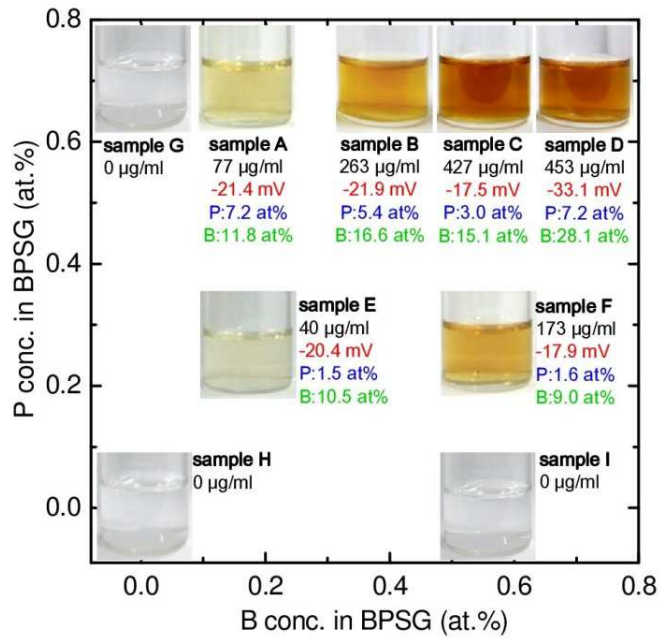
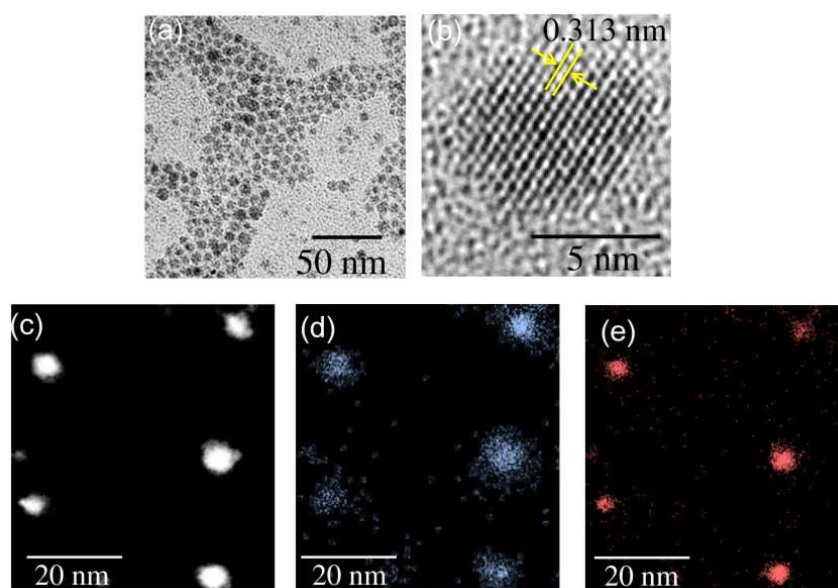


Figure 2-3. Photographs of the solutions after removing precipitates by centrifugation. The abscissa and ordinate are B and P concentrations, respectively, in as-deposited Si-rich BPSG films. The numbers below the pictures are the amounts of Si in the solutions, P and B concentrations in Si nanocrystals and the  $\zeta$ -potentials.

B and P codoped Si nanocrystals are characterized by electron microscopy. Figure 2-4 (a) shows the TEM image of codoped Si nanocrystals. Nanocrystals with approximately 5 nm in diameter are well-isolated and high-resolution TEM image in figure 2-4 (b) shows lattice fringes of monocrystalline Si. Figure 2-4 (c) shows a HAADF image, which shows 5 white spots corresponding to Si nanocrystals. Figure 2-4 (d) and (e) shows EELS mapping images of B and P, respectively, taken at exactly the same place. We find the 5 spots in the EELS mappings perfectly coincide with that in the HAADF image, demonstrating that B and P are heavily codoped (more than the detection limit of

EELS) in individual nanocrystals. The quantitatively determined average B and P concentration by ICP-AES is much higher than solid solubility limits of B and P in bulk Si crystal.<sup>67</sup> Therefore, it is reasonable that the majority of doped B and P atoms are not doped in the nanocrystal core, but located around the surface.



*Figure 2-4(a) TEM and (b) high-resolution TEM images of Si nanocrystals. (c) High-angle annular dark field image of Si nanocrystals. (d) and (e) Electron energy loss spectroscopy mappings of B and P, respectively.*

Figure 2-5 (a)–(d) show the TEM images of codoped Si nanocrystals grown at different temperatures (1050 to 1300°C). We find that the nanocrystals grow larger as the growth temperature increases. Figure 2-6 show the electron diffraction patterns obtained from several hundreds of nanocrystals grown at different temperatures. We also show the bars

corresponding to the data of diamond Si crystals (JCPDS No. 27-1402). The average diameters plotted in Figure 2-5 (e) demonstrate the controllability of the nanocrystal size just by varying annealing temperature. This can be explained simply by the fact that the diffusion coefficient of excess Si atoms in BPSG is larger in higher when annealed at a higher temperature. This simple growth mechanism allows us to estimate the diameter of nanocrystals prepared at temperature lower than 1000°C, which cannot be observed by TEM. At such temperature range, the nanocrystals are too small to directly determine from TEM images and also the lower contrast due to the low-crystallinity. We first obtain diffusion coefficients of Si in BPSG at different temperatures from the experimentally obtained sizes under the assumption that the radius of as-deposited Si clusters in BPSG is 0.5 nm.<sup>68</sup> By fitting the growth temperature dependence of the diffusion coefficients, the activation energy can be estimated to be 218 kJ/mol. Using obtained activation energy, the relation between the size and the temperature can be calculated.<sup>69</sup> The result is shown as a dashed red curve in Figure 2-5 (e). The calculated result reproduces experimentally obtained data well, and thus we can extrapolate the temperature dependence of the nanocrystal size. The average diameter can be tuned from around 1 nm to 14 nm.

The average numbers of P and B atoms per a nanocrystal are plotted in Figure 2-5 (f) as a function of diameters. The black curve represents the concentration of 1.0 at% ( $5 \times 10^{20} \text{ cm}^{-3}$ ). We find that the dopant concentration is very high. Especially, the B concentration is much higher than the solid solubility of B in bulk Si crystal.

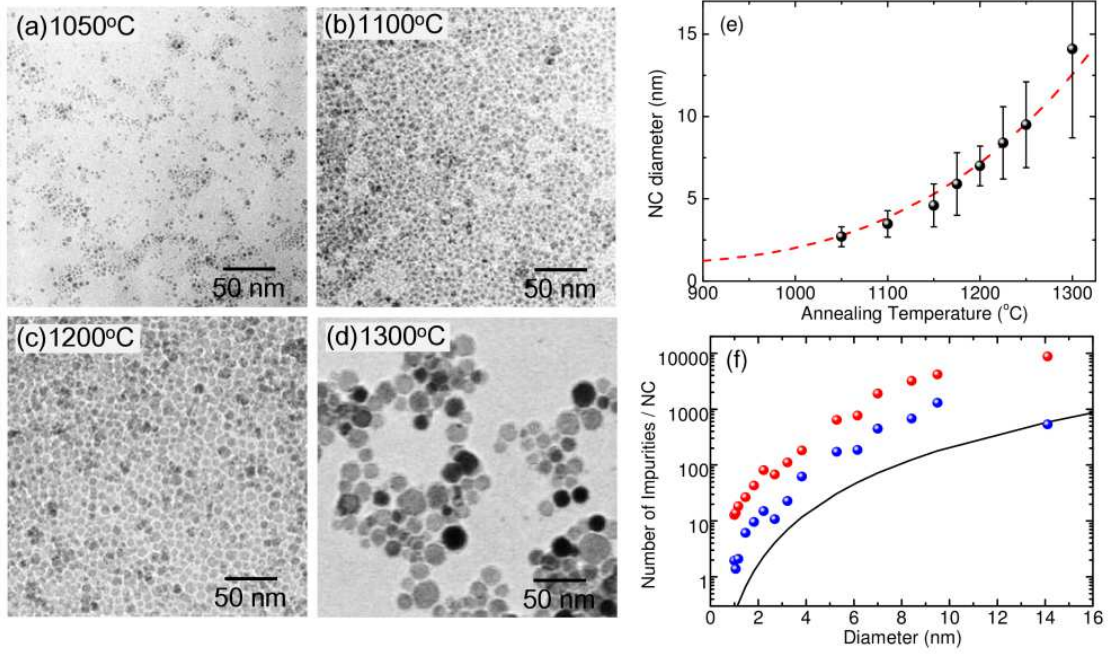
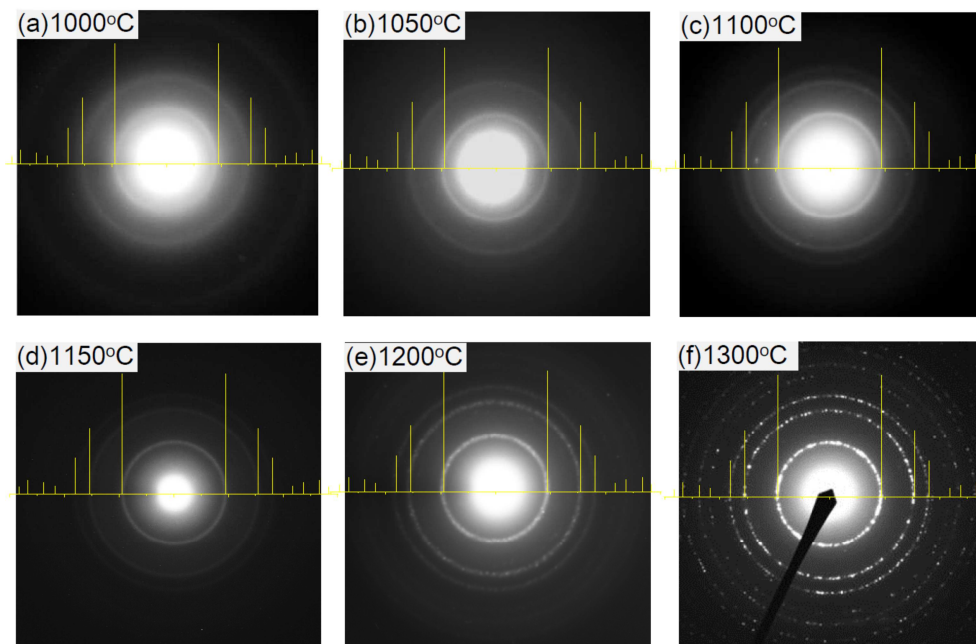


Figure 2-5 (a)-(d) TEM images of Si nanocrystals grown at different temperatures shown in the images. (e) Average diameters (black) as a function of annealing temperatures. Dashed red line shows the results of theoretical prediction. (f) Number of B (Red) and P (Blue) per nanocrystal as a function of average diameters. Black line corresponds to the concentration of 1.0 at.% ( $5 \times 10^{20} / \text{cm}^3$ ).



*Figure 2-6 Electron diffraction patterns of codoped Si nanocrystals grown at different temperatures.*

The results so far strongly suggest that B and P are doped at extremely high concentration and thus segregated to the surface of nanocrystals. To study the surface structures, we performed XPS measurements for free-standing codoped Si nanocrystals. Figure 2-7 shows XPS spectra of codoped Si nanocrystals with different sizes (1 day storage in methanol after HF etching). In the Si 2p signal, we find peaks assigned to Si nanocrystal cores ( $\text{Si}^0$ ) at 99.8 eV and surface native oxides ( $\text{Si}^{1+} \sim \text{Si}^{4+}$ ). The binding energy of the oxides smaller than that of stoichiometric  $\text{SiO}_2$  ( $\text{Si}^{4+}$ , 103.8 eV) suggests that the oxide layer is less than a monolayer. The size dependence of intensity ratio of the oxide signal can be explained by the increase of the ratio of surface Si atoms within the escape depth of photoelectrons (2 nm).<sup>70</sup> Figure 2-7 (b) shows the B

1s signals. Neutral B and B<sub>2</sub>O<sub>3</sub> exhibit XPS peaks at 187-188 and 193 eV, respectively. In codoped nanocrystals, the main peak around 188 eV is predominant, which indicates that the majority of doped B is non-oxidized. Similar results are obtained for the P 2p signals in Figure 2-7 (c). The main peak around 130 eV is assigned to non-oxidized P and the broad tail arises from sub-oxides.

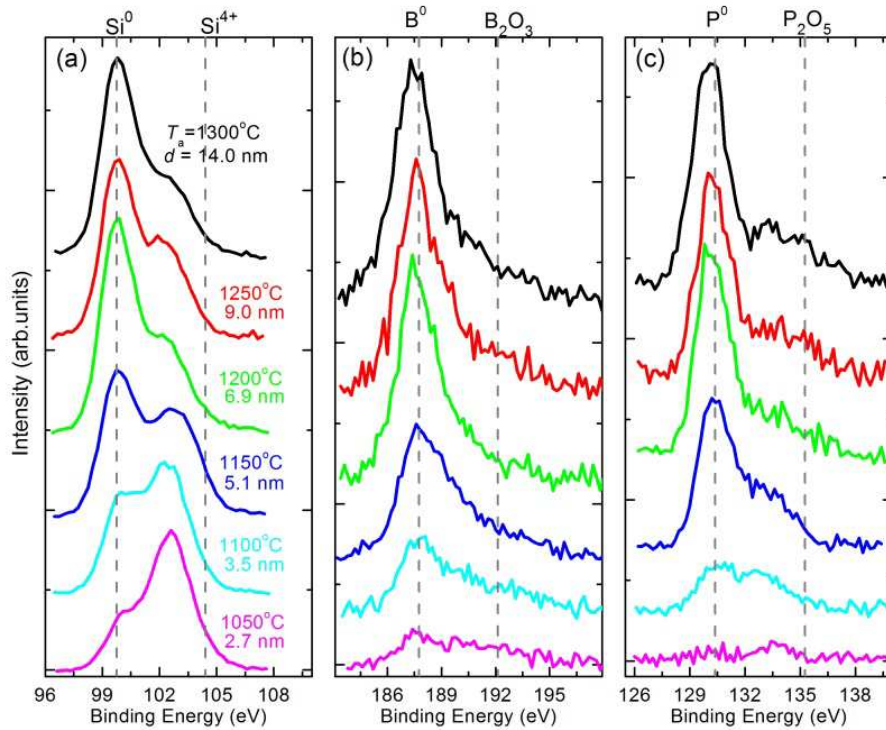
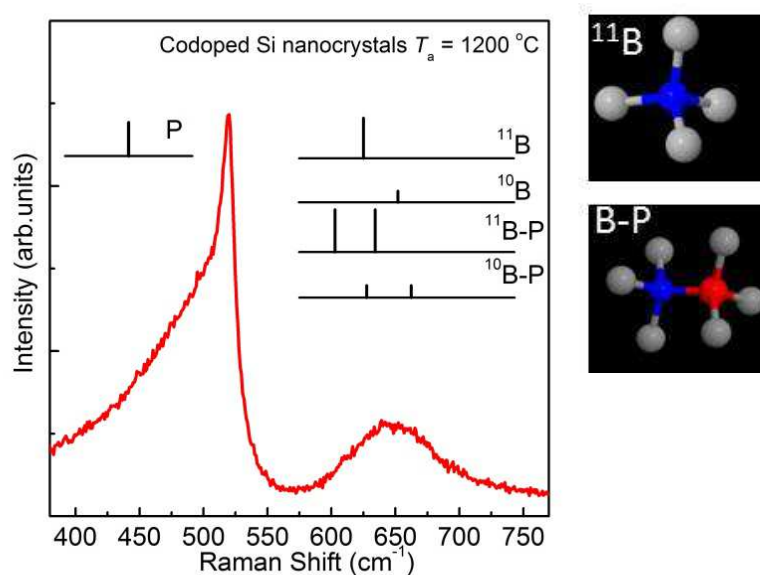


Figure 2-7 XPS spectra of codoped Si nanocrystals with different diameters. (a) Si 2p, (b) B 1s, (c) P 2p.

Figure 2-8 (a) shows the Raman spectrum of B and P codoped Si nanocrystals grown at 1200°C. The typical optical phonon mode of Si crystal is observed at 520 cm<sup>-1</sup>. In free-standing undoped Si nanocrystals, a significant low-energy shift of the peak is



observed when the nanocrystal size is smaller than 10 nm.<sup>71</sup> The size dependence is often explained by the phonon confinement effect. In oxide-embedded nanocrystals, the effect is compensated by the compression due to solid matrices surrounding the nanocrystals. Interestingly, in codoped Si nanocrystals, the peak is located exactly at 520 cm<sup>-1</sup> despite their small diameter of 6 nm. This result indicates that the crystal and surface structure of codoped Si nanocrystals are quite different from that of undoped nanocrystals. Besides, we find a broad band around at 650 cm<sup>-1</sup>. Considering the extremely high B concentration (15–20 at%), the broad band can be assigned to local vibrational modes of substitutional B,<sup>72</sup> B-P pairs,<sup>73,74</sup> B clusters, B-interstitial clusters<sup>75,76</sup> in Si crystal. The integrated intensity of the broad band (600–700 cm<sup>-1</sup>) is approximately 20% of that of the main peak (400–550 cm<sup>-1</sup>), which roughly corresponds to the B concentration measured by ICP-AES. The very broad tail at the low-energy side of the main peak can be assigned to amorphous Si and/or substitutional P and P-related clusters.<sup>77</sup>



*Figure 2-8. Raman spectrum of codoped Si nanocrystals grown at 1200°C with schematic illustrations of B, P doped structures.*

From the structural analysis, we present the structural model of codoped Si nanocrystal in Figure 2-9. Lattice fringes in TEM images associated with electron diffraction patterns, optical phonon mode of Si crystal in Raman spectrum, and Si 2p core signals in XPS suggest that the core of codoped nanocrystal is undoubtedly a crystalline Si, probably “lightly” doped with B and P. Here, “lightly” doping means the dopant concentration is lower than the solid solubility limits in bulk Si crystals. This is also supported by the theoretical calculation by the group of Prof. Ossicini.<sup>45</sup> They demonstrate the small formation energy of few dopants (B and P) in Si nanocrystals, which indicates that small number of B and P can be doped inside nanocrystals. The calculation in Ref.<sup>78</sup> also predicted that the dopants are preferentially located around the surface of Si nanocrystals. The preferential dopant locations were calculated in

codoped Si nanowires. The results demonstrated that B and P are doped at the interface of Si/SiO<sub>2</sub>, *i. e.*, the surface of Si-core.<sup>79,80</sup> XPS and Raman study demonstrate that the surface of nanocrystals is strongly modified by heavily codoping B and P. Here, “heavily doping” means doping with a concentration exceeding the solubility limit. In bulk Si crystal, it is known that saturated B-rich layers (BRL) are formed at the interface between B<sub>2</sub>O<sub>3</sub> and Si, when B is heavily doped in solid state diffusion processes.<sup>81</sup> Also in codoped Si nanocrystals, the heavily doped B are most likely to form the layer similar to BRL. The BRL exhibits hydrophilic nature, which explains the dispersibility of codoped Si nanocrystals in aqueous solution. It is worth noting that B atoms are doped in the crystalline Si as proven by the local modes in Raman spectrum. The difference between B-doped bulk Si crystal and codoped nanocrystals is the presence of P. Without P doping, the nanocrystals aggregate easily in solution. A possible explanation is that P plays a role to stabilize larger amounts of B atoms at the surface of Si nanocrystals by charge compensation and structural relaxation.

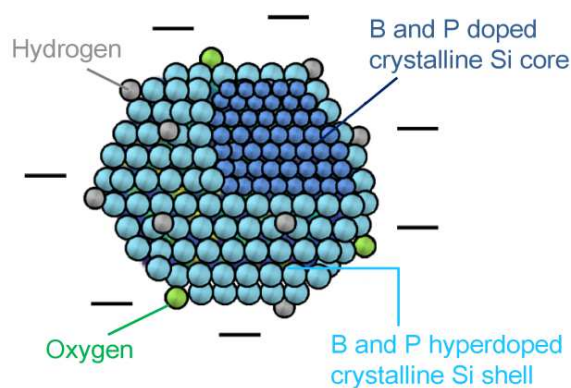


*Figure 2-9. Structural model of codoped Si nanocrystal*

## B. Photoluminescence properties

Figure 2-10 (a) shows normalized PL spectra of codoped colloidal Si nanocrystals with different sizes. The broad spectra (FWHM  $\sim 400$  meV) are obtained and the peak energy strongly depends on the size of nanocrystals. The PL peak energies are plotted in Figure 2-10 (b) as a function of size. We find the PL peak exhibits blue-shift monotonically as the size increases. Remarkably, the PL peak energy is below the bulk Si band gap (1.12 eV) when size is larger than 5 nm. For the comparison, we also plot the relation of undoped Si nanocrystals from literatures.<sup>19,24,82</sup> Although the trend is similar, such a low energy PL cannot be observed in undoped Si nanocrystals at room temperature. The observation of the below bulk-band gap PL is one of the evidence that the PL arises from the transitions between donor and acceptor states shown in Figure 2-10. The size dependence of PL energy is similar to that of undoped nanocrystals, while the energy is always lower by  $\sim 300$  meV. From the model in Figure 2-10 (c), the energy difference probably corresponds to the sum of binding energy of donor and acceptor doped in Si nanocrystals. Compared to bulk Si, the binding energy is much larger in the present nanocrystals. This can be explained by both the formation impurity band due to the high doping level forming the impurity band<sup>83,84</sup> and increased binding energy in nanocrystalline Si.<sup>46,85,86</sup> In heavily n- or p-type doped bulk Si, the dopant-related PL energy is 100-200 meV lower than bandgap PL was reported.<sup>83,84</sup>

In some specific sizes of Si nanocrystals, the energy differences between the highest occupied molecular orbitals (HOMO) and the lowest unoccupied molecular orbitals (LUMO) are calculated by first principles calculations when a pair of B and P is

doped.<sup>45</sup> For example, the HOMO-LUMO gap of B and P codoped Si nanocrystal (1.8 nm in diameter) is calculated to be in the range between 1.59 and 2.03 eV depending on the B and P distance and their sites. In the present work, the PL peak energy of codoped Si nanocrystals 1.8 nm in diameter is around 1.7 eV, in good agreement with the theoretical prediction. Furthermore, the paper demonstrated the difference of HOMO-LUMO gaps between codoped and undoped nanocrystals is approximately 300 meV, almost corresponding to our experimental results.

Figure 2-10 (e) shows the PL lifetimes of codoped and undoped Si nanocrystals prepared by same procedures (cosputtering and annealing)<sup>19</sup> as a function of the diameter. The lifetimes obtained at the PL maxima are plotted for both samples. The trend is totally different between codoped and undoped nanocrystals. In undoped nanocrystals, the lifetime depends strongly on the size, while almost independent of the size in codoped nanocrystals larger than 3 nm. The lifetime insensitive to the nanocrystal size can be explained by the following model. In codoped nanocrystals, the first principle calculations showed that phot-excited carriers are localized at the impurity states.<sup>45</sup> The localization might relax the momentum conservation rule during the optical transition and enhances the radiative recombination rate compared to that of undoped nanocrystals. As a result, the physical size nanocrystals, which determines the degree of the relaxation of the momentum conservation rule and the radiative recombination rate in undoped nanocrystals, is not a determining factor of PL lifetime. In codoped Si nanocrystals, carriers are localized not only by potential barriers at the surface but also by potentials induced by ionized B and P. When the size is relatively large, the latter is more striking for PL properties including the lifetime. On the other

hand, when the size is below a certain value, the physical size of nanocrystals becomes dominant.

Figure 2-10 shows the PL quantum yields as a function of the size. For nanocrystals larger than 3 nm, the PL quantum yield decreases while the PL lifetime is almost constant as shown in Figure 2-10. This implies that with increasing the size, the ratio of dark Si nanocrystals increases. Iori *et al.*<sup>87</sup> demonstrated that, in the small Si nanocrystals (~1.5 nm), the formation energy of Si nanocrystals in which exactly the same number of P and B atoms are doped is much smaller than those in which unequal number of P and B atoms are doped. This suggests that perfectly compensated Si nanocrystals are preferentially grown by annealing Si-rich BPSG. On the other hand, when the size increases and the number of dopants per a nanocrystal increases (see figure 2-5), the difference of the formation energy between perfectly and imperfectly compensated nanocrystals is considered to be small. As a result, the ratio of uncompensated nanocrystals increases. Excess carriers in Si nanocrystals leads to efficient Auger recombination with the lifetime time of 0.1–100 ns,<sup>88</sup> which is more than 3 orders of magnitude shorter than the radiative lifetime of Si nanocrystals. Therefore, uncompensated Si nanocrystals thus become almost completely dark. The increase of the ratio of dark nanocrystals results in the quantum yield decrease without the lifetime reduction. The quantum yield of codoped nanocrystals is quite good if we compare the value with those of other materials emitting in the NIR range. For example, the QY of codoped Si nanocrystals with 6.2 nm in diameter emitting around 1150 nm is 0.14%. This value is larger than that of a NIR luminescent dye (IR-26, quantum yield ~ 0.05%), emitting in the same energy range (1130 nm).<sup>89</sup> When the diameter is smaller

than 3 nm, both the lifetime and quantum yield decrease, which indicates the formation of non-radiative recombination processes due to disorders in or on the surface of small Si nanocrystals.

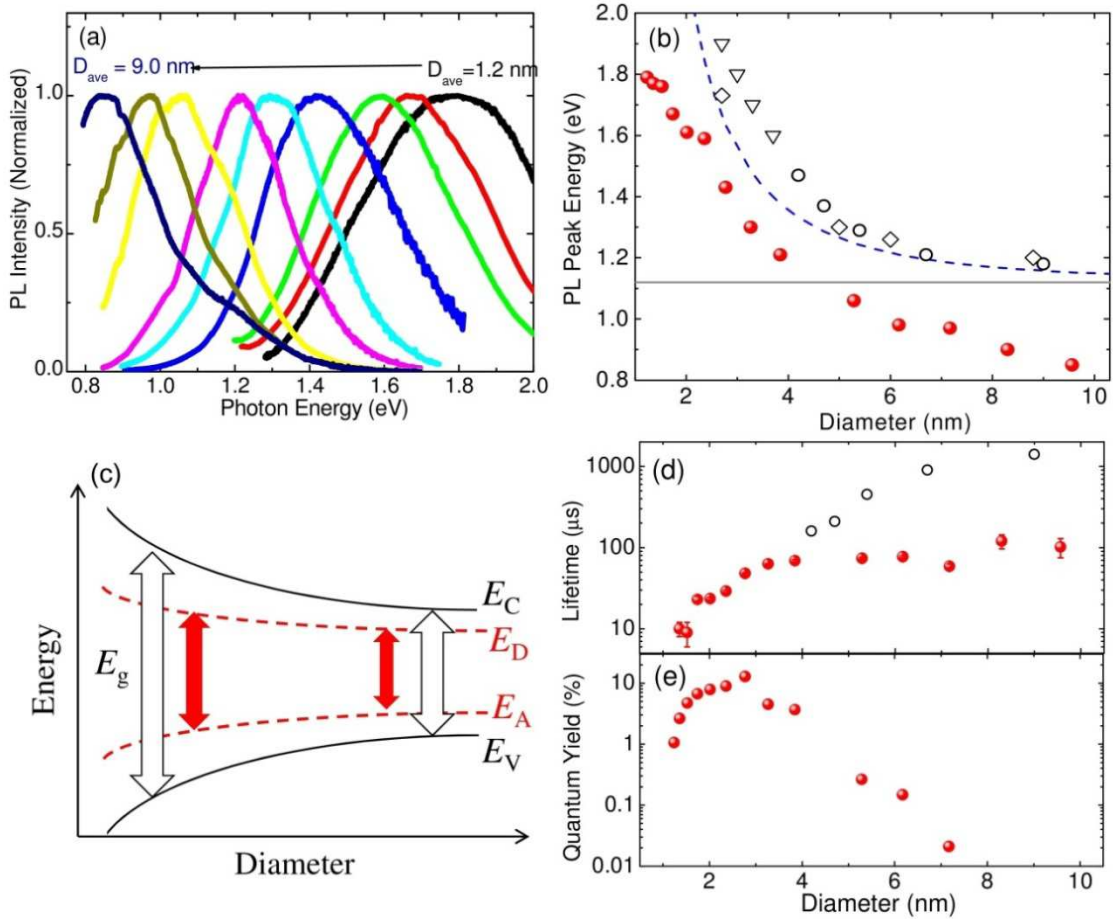


Figure 2-10. (a) PL spectra of codoped Si nanocrystals with different average diameters. (b) PL peak energy as a function of diameters. The open symbols are from Ref <sup>19</sup>( $\circ$ ), <sup>23</sup>( $\diamond$ ) and <sup>82</sup>( $\nabla$ ). (c) Schematic of size-tunable energy level structure of shallow donor and acceptor codoped Si nanocrystals. (d) PL lifetimes and (e) quantum yields of codoped (red) and undoped (open circle) Si nanocrystals<sup>19</sup> as a function of nanocrystal diameters.

## 2-5 Conclusion

A new type of all-inorganic colloidal Si nanocrystals is successfully produced by heavily codoping of B and P. The structural and optical properties are studied in detail, which demonstrate that B and P are very heavily doped ( $>$  bulk solubility limits) simultaneously and they form heavily B and P doped shells. The shells induce negative potential on the surface of Si nanocrystals and make them dispersible in water and alcohols without organic surface ligands. By the presence of B and P protecting layer on nanocrystal surface, the nanocrystals are chemically very stable and the luminescence properties are insensitive to the environment. The nanocrystals exhibit size-tunable luminescence in a very wide energy range. Remarkably, larger Si nanocrystals ( $D_{\text{ave}} > 5$  nm) show luminescence at the energy below the band gap of bulk Si crystal at room temperature. The low-energy luminescence suggests that the PL arises from the radiative transitions between donor and acceptor states in Si nanocrystals with increased binding energy of impurities due to the confinement effects. Because of these superb properties, B and P codoped Si nanocrystals are potentially have applications in optoelectronic devices and in biology.



## Chapter 3

# Synthetic Route of B and P codoped Colloidal Si Nanocrystals from Hydrogen Silsesquioxane

Adapted from *H. Sugimoto, et al., Nanoscale, 6, 12354–12359 (2014)*

### 3-1 Introduction

In Chapter 2, we have demonstrated the development of colloidal dispersion of Si nanocrystals in polar solvents, which is achieved by the formation of high B and P concentration shells on the surface. A drawback of the preparation codoped nanocrystals is the small production rate. Since the formation process of codoped colloidal Si nanocrystals includes a sputtering process, production of large amount of colloidal solutions meeting the requirement of industrial applications is very hard and expensive.

In this section, we present a new simple route for mass-production of Si nanocrystals with high B and P concentration shells by extending the process in Refs. <sup>90</sup> and <sup>91</sup>. The process is summarized in Figure 3-1. Codoping of B and P is achieved by simple addition of dopant acids ( $\text{H}_3\text{BO}_3$  and  $\text{H}_3\text{PO}_4$ ) in hydrogen silsesquioxane (HSQ) solution. Dried mixture of HSQ,  $\text{H}_3\text{BO}_3$  and  $\text{H}_3\text{PO}_4$  are annealed at temperatures from 900 to 1200°C in  $\text{N}_2$  gas, which results in the growth of Si nanocrystals in BPSG

matrices. Si nanocrystals are then liberated from the matrices by HF etching. Finally, free-standing Si nanocrystals are dispersed in methanol.

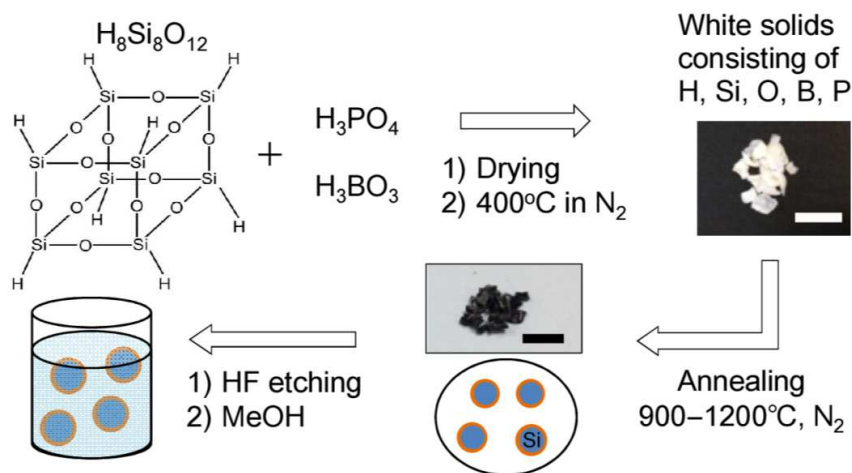


*Figure 3-1 Preparation procedure of all-inorganic B and P codoped colloidal Si nanocrystals. Scale bars in photographs are 1 cm.*

## 3-2 Materials and Methods

### *Synthesis of colloidal Si nanocrystals:*

Phosphoric acid solution (100  $\mu\text{L}$ ) (85 wt% in ethanol, Wako) and boric acid powder (150 mg) (Wako) were dissolved in 5 mL of ethanol. 400  $\mu\text{L}$  of the solution was added to 1 mL of HSQ (Fox-16, Dow Corning Corporation, 16 wt.% HSQ in methyl isobutyl ketone) solution. The mixture solution was stirred for 30 minutes and dried overnight. The resulting white glassy solid was annealed in  $\text{N}_2$  gas atmosphere first at  $400^\circ\text{C}$  for 30

min, and then at higher temperatures (900, 1000, 1100 and 1200°C) for 30 min. During the second stage of annealing, the glassy solid transforms into a black lump, which is composed of BPSG containing B and P codoped Si nanocrystals. The size of nanocrystals can be controlled by annealing temperature. Doping concentration can be varied by changing the amount of phosphoric and boric acids in HSQ solution. In order to isolate Si nanocrystals from BPSG matrices, the black lump was ground in a mortar and dissolved in HF solution (46 wt%). Si nanocrystals isolated in HF solution were then transferred to methanol. A large fraction of Si nanocrystals dispersed in methanol without any additional processes and the others precipitated. Precipitates were removed by centrifugation (4500 rpm, 10 min) and the supernatant solutions were stored in a vial. All the processes were performed in an ordinary laboratory environment. The yield of colloidal Si nanocrystals depends on several parameters such as doping concentration and growth temperature. When HSQ, H<sub>3</sub>PO<sub>4</sub> and H<sub>3</sub>BO<sub>3</sub> are 144 mg, 85 mg and 150 mg and the annealing temperature is 1100°C, a yield is as follows. By annealing the mixture solution, about 244 mg of BPSG powder containing Si nanocrystals is obtained. The estimated amount of excess Si in the BPSG powder is 16.3 mg. After removing BPSG matrices by HF etching, about 7.3 mg of Si nanocrystals can be retrieved in methanol.

#### *Characterization:*

TEM observations (JEM-2100F, JEOL) were performed for carbon-coated TEM meshes on which colloidal Si nanocrystals are drop-cast. XPS measurements (PHI X-tool, ULVAC-PHI) were carried out using Al K $\alpha$  X-ray source. Raman spectra were

measured using a confocal microscope (50 $\times$  objective lens, NA=0.8) equipped with a single monochromator and a CCD. The excitation source was a 514.5 nm line of an Ar ion laser. The excitation power was 1.1 mW. The samples for XPS, Raman and IR absorption measurements were prepared by drop-casting colloids on gold-coated Si wafers. The details of measurements of PL spectra and PL-QYs were shown in Chapter 2.

### 3-3 Results and Discussion

Figures 3-2 (a) shows a picture of the solution of Si nanocrystals grown at 1200 $^{\circ}$ C. The solution is very clear and the characters behind the 1cm cubicle can clearly be seen. The solution is stable and no precipitates are observed for more than 6 months. Optical transmittance spectra of solutions containing nanocrystals grown at 900 to 1200 $^{\circ}$ C are shown in Figure 3-2 (b). The transmittance below the band gap energy of bulk Si crystal is nearly 100%, indicating that light scattering by nanocrystal agglomerates is negligibly small. It should be stressed here that Si nanocrystals can be dispersed in methanol only when  $\text{H}_3\text{BO}_3$  and  $\text{H}_3\text{PO}_4$  are simultaneously added in HSQ solution. In the visible range, the absorption onset shifts to the shorter wavelength when the growth temperature is lower. This is due to smaller sizes and resultant stronger quantum confinement effects for nanocrystals grown at lower temperatures.

Figure 3-2 (c) shows a typical high-resolution TEM image of a Si nanocrystal grown at 1200 $^{\circ}$ C. Lattice fringes corresponding to  $\{111\}$  plane of Si crystal (0.31nm) are clearly

seen. TEM observations over wide areas reveal that no three-dimensional agglomerates of nanocrystals are formed. This evidences that Si nanocrystals are dispersed in methanol perfectly as isolated nanocrystals. The average diameters and the standard deviations obtained by TEM observations are summarized in Table 3-1. For nanocrystals grown at 900°C, the size was too small to be estimated by TEM observations.

Figure 3-2 (d) shows IR absorption spectrum of Si nanocrystals grown at 1200°C. The peaks around 2100 and 870  $\text{cm}^{-1}$  are due to Si-H<sub>x</sub> vibrations.<sup>92</sup> The weak peaks around 1080 and 480  $\text{cm}^{-1}$  are assigned to Si-O-Si stretching and rocking vibration modes, respectively. The small peak around 1000  $\text{cm}^{-1}$  is probably due to O<sub>x</sub>-Si-H<sub>y</sub> vibrations.<sup>93,94</sup> The surface of Si nanocrystals are thus hydrogen-terminated and slightly oxidized. No signals assigned to organic molecules such as C-H (~2900  $\text{cm}^{-1}$ ) and Si-C (680  $\text{cm}^{-1}$ ) vibrations<sup>95</sup> are observed. This confirms that the high dispersibility of codoped Si nanocrystals in methanol is not due to organic capping, but to other mechanisms.

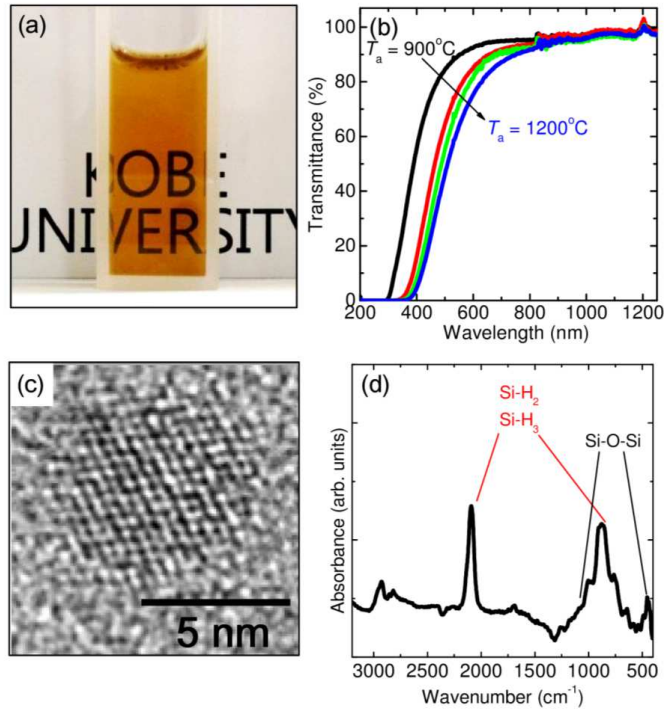


Figure 3-2. (a) Photograph of solution in which codoped Si nanocrystals grown at 1200°C are dispersed. (b) Optical transmittance spectra of colloidal dispersion of nanocrystals grown at 900 to 1200°C. (c) High-resolution TEM image of a Si nanocrystal grown at 1200°C. Lattice fringes correspond to (111) plane of Si crystal. (d) IR absorption spectrum of codoped Si nanocrystals grown at 1200°C.

Table 3-1. List of samples. The annealing temperature ( $T_a$ ), average diameter ( $d_{ave}$ ) and the standard deviation ( $\sigma$ )

Name	$T_a$ (°C)	$d_{ave}$ (nm)	$\sigma$ (nm)	B (at.%)	P (at.%)
sample A	900	-	-	4.5	2.4
sample B	1000	3.7	1.3	6.0	4.8
sample C	1100	4.8	1.7	8.1	4.6
sample D	1200	5.3	1.7	9.0	4.1

To analyze the structure of the surface of codoped Si nanocrystals, we measured XPS spectra of Si, B and P. In Si 2p spectra in Figure 3-3 (a), a peak appears at 99.8 eV with a tail to the high energy side. The peak is assigned to  $\text{Si}^0$  and is considered to arise from crystalline Si cores.<sup>96</sup> The high-energy tail is from surface native oxide. The tail is larger when the growth temperature is lower. At the lowest temperature (900°C), a sub-peak emerges at 103.8 eV ( $\text{Si}^{4+}$ ).<sup>96</sup> The increase of the oxides signal at lower growth temperatures can be explained by the increased surface-to-volume ratio. It should be stressed here that, considering the escape depth of photoelectrons, the native oxide is much thinner than 2 nm.<sup>97</sup> This is consistent with the TEM image and the IR absorption spectrum.

In B 1s spectra in Figure 3-3 (b), the peak energy is around 188 eV. It is known that neutral B atoms and  $\text{B}_2\text{O}_3$  exhibit XPS peaks at 187–188 and 193 eV, respectively. Therefore, majority of doped B atoms exist as the non-oxidized states. The situation is similar in P 2p spectra (Figure 3-3 (c)) when the growth temperature is higher than 1000°C. The energy of the peak (130 eV) coincides with  $\text{P}^0$ , and thus majority of doped P atoms exist also as the non-oxidized states. When the growth temperature is 900°C, the peak at 135 eV is larger than that of  $\text{P}^0$  at 130 eV. The 135 eV peak is assigned to  $\text{P}_2\text{O}_5$ , indicating that nanocrystals grown at lower temperatures are more vulnerable for oxidation.

In Table 3-1, B and P concentrations quantified from the integrated peak intensities of XPS spectra are shown. Note that the concentration shown in Table 3-1 is not the

average concentration of a whole volume of a nanocrystal, because of the small escape depth of photoelectrons ( $\sim 2$  nm). In small nanocrystals, the concentration may be close to the average concentration, while in large nanocrystals, the concentration of the surface layer is more emphasized and is different from the average concentration. In Table 3-1, the concentration is much higher than the solid solubility limits of B and P in bulk Si crystal.<sup>67</sup> Considering the fact that Si nanocrystals are single crystal with high crystallinity as confirmed by TEM observations, doping of B and P in Si nanocrystal cores by exceeding the solubility limits is very unlikely. Therefore, the XPS results indicate that B and P are mainly doped on or near the surface of Si nanocrystals, and heavily B and P doped shells are formed.

Figure 3-3 (d) shows a Raman spectrum of a sample grown at  $1200^{\circ}\text{C}$ . In addition to a Raman peak of crystalline Si at  $520\text{ cm}^{-1}$ , a broad band is observed around  $650\text{ cm}^{-1}$ . The band can be assigned to B-related local vibrational modes, such as substitutional  $\text{B}^{10}$  and  $\text{B}^{11}$  and substitutional B-P pairs.<sup>72,98,99</sup> Furthermore, B clusters such as  $\text{B}_2$  and B-interstitial clusters in crystalline Si lattices exhibit Raman peaks in the  $650\text{--}700\text{ cm}^{-1}$  range.<sup>100</sup> The observation of the relatively strong  $650\text{ cm}^{-1}$  band suggests that the heavily B and P doped shells are crystalline shells.



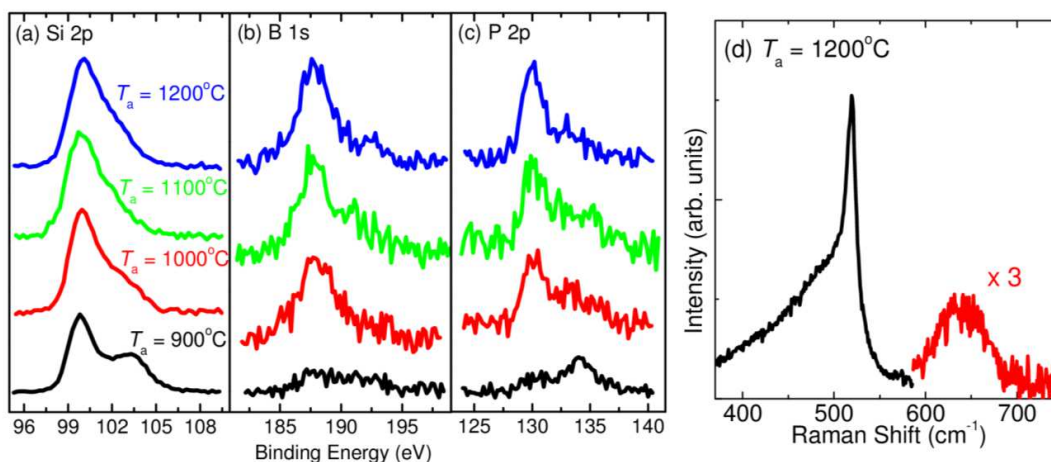


Figure 3-3. XPS spectra of samples grown at 900 to 1200°C (a) Si 2p (b) P 2p (c) B 1s. (d) Raman spectrum of codoped Si nanocrystals grown at 1200°C.

The TEM, FT-IR, XPS and Raman results suggest the structural model. The nanocrystal core is B and P doped crystalline Si. The shell is also crystalline Si, but B and P are doped much more heavily, exceeding the solid solubility limit in bulk Si crystal. The outer surface is terminated by hydrogen and oxygen. Recently, Guerra et al. studied the arrangements of B and P in codoped Si nanocrystals by *ab initio* calculations.<sup>78</sup> They found that pairs of B and P are preferentially located near the surface of nanocrystals. This is consistent with our model that heavily B and P doped crystalline shells are formed. Furthermore, they studied the relative arrangement of B and P. The most energetically favored structure is that B is located on the outer surface and P in the inner of B.<sup>78</sup>

In bulk Si crystal, it is known that saturated B-rich layers (BRL) are formed at the interface between B<sub>2</sub>O<sub>3</sub> and Si, when B is heavily-doped by solid state diffusion

processes.<sup>101</sup> The BRL is hydrophilic and has high resistance to HF etching.<sup>102</sup> The heavily B and P doped shells in the present Si nanocrystals are considered to be a kind of BRL, which makes Si nanocrystals hydrophilic and dispersible in polar solvents. The difference between B-doped bulk Si crystal and present Si nanocrystals is the necessity of P codoping for the formation of BRL. A possible explanation is that P plays a role to stabilize larger amounts of B atoms at the surface of Si nanocrystals by charge compensation. In fact, theoretical work demonstrates that B and P codoping is energetically much more favorable, and codoped Si nanocrystals have lower formation energy than B or P singly doped ones.<sup>45</sup>

Figure 3-4 (a) shows PL spectra of codoped colloidal Si nanocrystals. The PL peak shifts from 1030 to 740 nm with decreasing the growth temperature. This is due to stronger confinement of carriers with decreasing the size. In our previous work on codoped colloidal Si nanocrystals prepared by sputtering, we studied the size dependence of the PL properties in detail.<sup>43,103,104</sup> The PL energy of codoped Si nanocrystals is controlled in a very wide range (0.85 - 1.8 eV) by varying the size from 1 nm to 14 nm. In the whole size range, the PL energy is 300–400 meV lower than that of undoped Si nanocrystals. The consistent low-energy shift of the PL by codoping suggests that the PL arises from the optical transitions between donor and acceptor states.<sup>43,103,104</sup> Since the structure of the present Si nanocrystals is similar to those of the previous work, the PL is also considered to arise from the donor to acceptor transitions. In fact, in Figure 3-4 (a), the low energy tail of the PL spectra of nanocrystals grown at high temperatures extends below the bulk Si band gap. This is evidence that donor and

acceptor states contribute to the PL. The QYs of the PL are shown in the figure. The largest value is 10.7% for nanocrystals grown at 1100°C.

In Figure 3-4 (b), PL mean lifetimes defined by  $\tau = \int_{t_0}^{\infty} \left[ \frac{I(t)}{I_0} \right] dt$ , where  $I(t)$  is the PL intensity as a function of time  $t$  and  $I_0$  is the initial intensity at time  $t_0$ , are plotted as a function of the detection wavelength.<sup>105</sup> The decay curves (not shown) are not a single-exponential function. For Si nanocrystals grown at 1100 and 1200°C, the lifetimes are several hundreds of  $\mu s$ , and are almost independent of the growth temperature, i.e., the lifetime depends only on the detection wavelength. However, the QY of nanocrystals grown at 1200°C is much smaller than that grown at 1100°C. This discrepancy suggests that the QY is mainly determined by the number of dark nanocrystals that do not contribute to the PL. Similar scenario can be applied for nanocrystals grown at 900 and 1000°C. On the other hand, the large difference of the lifetime between the two groups, i.e., nanocrystals grown at 900 and 1000°C and those at 1100 and 1200°C, is not clear. It may be possible that crystallinity is degraded when the growth temperature is below 1000°C and the degradation shortens the lifetime.

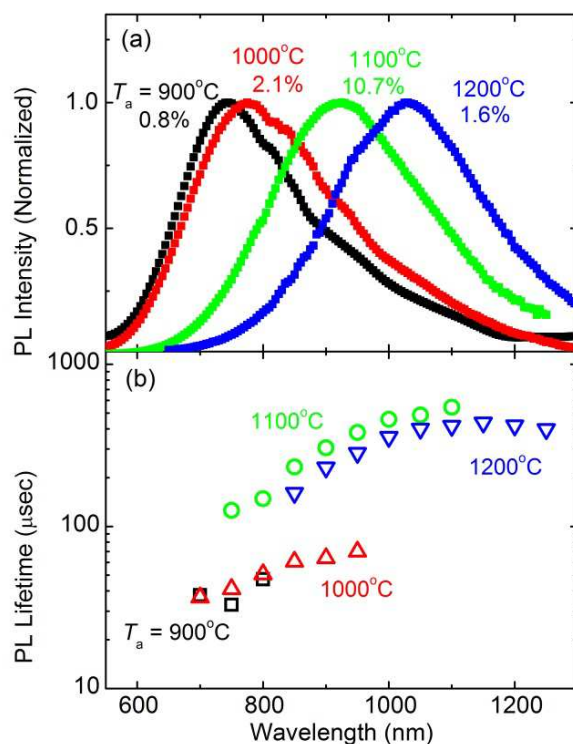


*Figure 3-4.(a) Normalized PL spectra of colloidal dispersion of codoped Si nanocrystals grown at 900 to 1200°C. PL quantum yields are shown in the figure. (b) PL lifetimes as a function of detection wavelengths.*

Figure 3-5 (a) shows a SEM image of a nanocrystal film prepared by spin-coating (1000 rpm, 2 min) concentrated colloid of nanocrystals grown at 1200°C (~5 mg/ml). A uniform film about 500 nm in thickness is prepared by one spin-coating process. Because of perfect dispersion of isolated nanocrystals in solution, the film is very smooth and flat over a large area. The PL spectrum of the nanocrystal film is shown in Figure 3-5 (b). For comparison, PL spectrum of the colloid is also shown. The spectra are almost identical, indicating that codoped Si-nanocrystals are very stable even after air exposure.

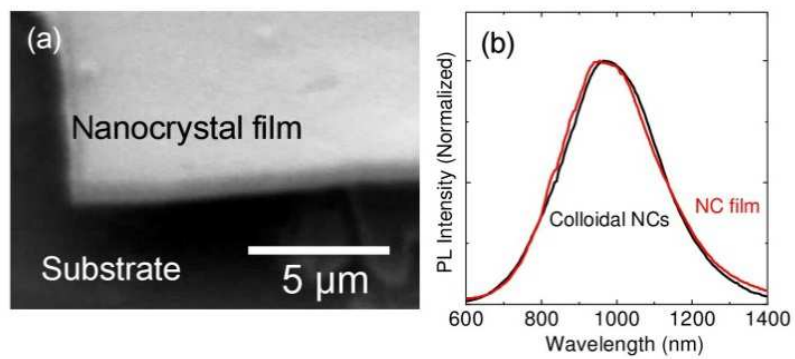


*Figure 3-5.(a) SEM image of a nanocrystal film prepared by spin-coating colloidal dispersion of nanocrystals grown at 1200°C. (b) Comparison of PL spectra of colloidal dispersion and the spin-cast nanocrystal film.*

### 3-4 Conclusions

We developed a novel vacuum-free route for mass-production of all-inorganic colloidal Si nanocrystals. The nanocrystals have heavily B and P doped crystalline shells and the shells make Si nanocrystals hydrophilic and dispersible in polar solvents. The colloids show efficient size-tunable PL in the near IR to visible region. Because of perfect dispersion of isolated Si nanocrystals in solution, smooth and flat nanocrystal films are easily prepared by spin-coating the solution.

## Chapter 4

# Water-Dispersible Si Nanocrystals: Photoluminescence Properties and Stability

Adapted from *H. Sugimoto, et al., Nanoscale, 1, 122–126 (2014).*

### 4-1 Introduction

Colloidal nanocrystals have been considered to be a promising alternative to organic dyes for biological fluorescence imaging,<sup>106</sup> because of the superior properties such as size-tunable luminescence, chemical stability in aqueous media as well as high photostability. As mentioned in Chapter 1, the II–VI and IV–VI compound semiconductor nanocrystals consist of toxic elements, which limit their extensive applications as contrast agents for *in vivo* and *in vitro* biological labeling. In contrast, Si nanocrystals possess higher compatibility with biological substances. For *in vivo* biomedical applications, Si nanocrystals should be hydrophilic and be dispersed in water in a wide pH range. Furthermore, the PL wavelength is preferably within the biological window (700–1200 nm). Unfortunately, colloidally-stable Si nanocrystals synthesized so far is hydrophobic and dispersed in nonpolar solvents, which is unsuitable for biological applications. Only a limited number of researches have been made on water-dispersible Si nanocrystals. Ruckenstein et al.<sup>107</sup> synthesized poly(acrylic acid) grafted

water-dispersible Si nanocrystals with a high PL quantum yield (QY) of 24%. However, the PL was in the visible range (~600 nm). Water-dispersible Si nanocrystals emitting in the similar range (650 nm) reported by Zhong et al. were capped with protein (IgG) and emitted with high pH- and photostability.<sup>108</sup> Lin et al. realized water-dispersible Si nanocrystals by the formation of thick oxide shells, although the PL wavelength was very short (450 nm).<sup>109</sup> Erogbogbo et al.<sup>110</sup> employed a different approach to obtain the dispersibility in water, which is polymer-coated or micelle-encapsulated Si nanocrystal assemblies (50-150 nm). They showed stable PL around 650 nm. However, the large size of the Si nanocrystal assemblies limits the application in specific fields. The development of Si nanocrystals dispersible in water in a wide pH range and emitting in the NIR range is still a challenging task.

In this section, we study the stability and optical properties of B and P codoped Si nanocrystals dispersed in water, which is very important for the applications we discussed above.

## 4-2 Materials and Methods

Colloidal B and P codoped Si nanocrystals were prepared the same method as that shown in Chapter 2. To obtain aqueous dispersion of nanocrystals, we first disperse them in methanol for stabilization. Using the same way that we remove HF, we exchange the solvent from methanol to water. This process is indispensable to obtain water-dispersible



codoped Si nanocrystals with a high-yield. The details of measurements of PL spectra and PL-QYs were shown in Chapter 2.

### 4-3 Results and Discussion

The list of the samples studied in this work is summarized in Table 4-1. For all the samples (samples A–D) preparation parameters are fixed except for the annealing temperature (see Experimental section). Figure 4-1 (a)–(c) shows photographs of aqueous solutions and transmission electron microscope (TEM) images of codoped Si nanocrystals (samples B–D). We can see yellowish optically clear solutions. Figure 4-1 (d) shows the optical transmittance spectra of sample D measured 2, 3 and 5 weeks after the preparation. The insets are the photographs after 2 and 5 weeks. The transmittance in the NIR range is almost 100%, indicating that light scattering caused by agglomerates is negligibly small. The solution is very clear and the color density does not change significantly even after 5 weeks. In the TEM images, the dark spots correspond to Si nanocrystals with the diamond structure as confirmed by electron diffraction patterns. In a high resolution TEM image (inset of Figure 4-1 (c)), lattice fringes corresponding to the {111} planes of Si crystal can clearly be seen, implying that the codoped Si nanocrystal is defect-free single crystal. We can confirm from TEM images that Si nanocrystals are isolated and do not form agglomerates. The average diameters ( $d_{ave}$ ) of Si nanocrystals in samples B, C and D estimated from the TEM images are 2.8, 3.9 and 5.2 nm, respectively, and the standard deviations of the size distribution ( $\sigma$ ) are 0.7, 0.8 and 0.8 nm, respectively. In sample A, Si nanocrystals were

not clearly observed by TEM and the electron diffraction pattern was halo, suggesting that the diamond structure is strongly distorted.

*Table 4-1. List of samples. Annealing temperature ( $T_a$ ), average diameter ( $d_{ave}$ ) and standard deviation ( $\sigma$ ).*

Sample name	$T_a$ (°C)	$d_{ave}$ (nm)	$\sigma$ (nm)
Sample A	1000	-	
Sample B	1050	2.8	0.7
Sample C	1100	3.9	0.8
Sample D	1150	5.2	1.0

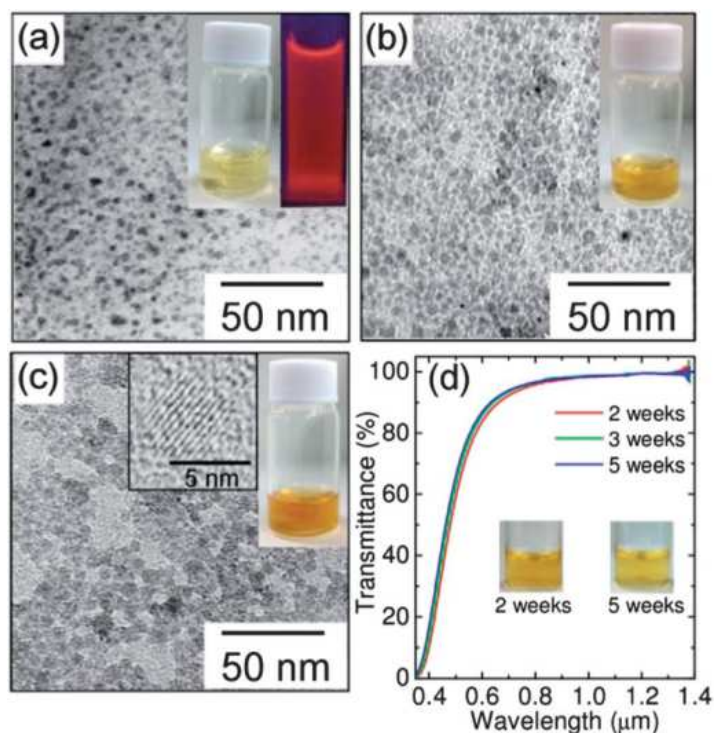


*Figure 4-1. TEM images and photographs of Si nanocrystals dispersed in water. (a) Sample B (photo on the right: under UV (352 nm) irradiation), (b) sample C, and (c) sample D. (d) Optical transmittance spectra of sample D stored in water for different terms. The storage terms are shown in the figure. Inset: photographs of the sample after storage for 2 and 5 weeks.*

As shown in Figure 4-2 (a), the solution exhibits bright red luminescence under UV irradiation (352 nm, FL4BLB, TOSHIBA). Figure 4-2 (a) shows the PL spectra of codoped colloidal Si nanocrystals in water (samples A–D). Size dependent shift of the PL from red to NIR regions can clearly be seen. The observed size dependence of the PL wavelength is quantitatively in good agreement with that of codoped colloidal Si nanocrystals in methanol, despite the large difference in the dielectric constants ( $\epsilon_{r\_water}$

$= 78.5$  and  $\epsilon_{\text{r\_methanol}} = 33$ ).<sup>111</sup> PL of codoped Si nanocrystals is thus insensitive to the solvent polarity. In Figure 4-2 (a), the PL quantum yields (QYs) are also shown. The highest PL-QY of 10.2% is obtained for sample B (PL peak:  $\sim 760$  nm). This is to our best knowledge, the highest PL-QY reported for Si nanocrystals dispersed in water and luminescing in the biological window.

Figure 4-2 (b) shows the PL mean lifetimes defined by  $\tau = \int_{t_0}^{\infty} \left[ \frac{I(t)}{I_0} \right] dt$ , where  $I(t)$  is the PL intensity as a function of time  $t$  and  $I_0$  is the initial intensity at time  $t_0$  of samples A-D as a function of detection wavelength (see the right side of Figure 4-2 ). The wavelength dependence of the lifetimes is on the same trend for all samples, although the data are scattered. The lifetimes are from several tenths of  $\mu\text{s}$  in the red region to over 100  $\mu\text{s}$  in the NIR region. The lifetimes are comparable to those of Si nanocrystals in nonpolar solvents exhibiting PL in the same wavelength range.<sup>24</sup>

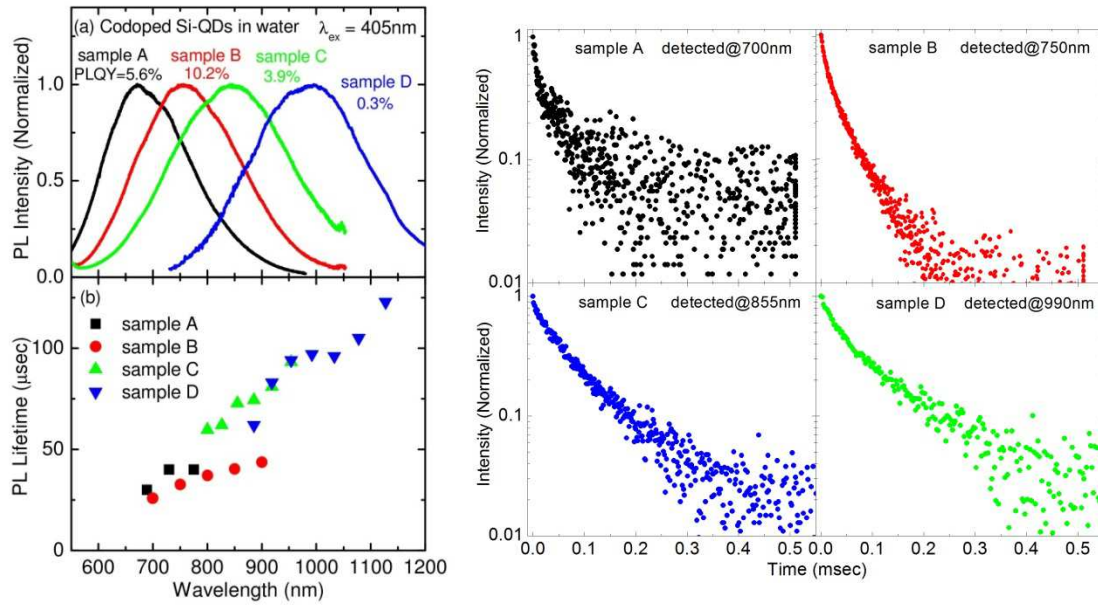


Figure 4-2 (a) PL spectra of samples A–D. PL quantum yields are shown in the figure. (b) PL lifetimes of samples A–D as a function of detection wavelength. Right panels: Representative decay curves of all samples.

Figure 4-3 (a) and (b) shows the evolution of the PL intensities of samples B and C, respectively, in water under continuous irradiation of 450 nm ( $150 \mu\text{W}/\text{cm}^2$ ) and 365 nm ( $180 \mu\text{W}/\text{cm}^2$ ) light for 2 h. When excited at 365 nm, the PL intensities decrease by about 10% within 100 s for both the samples. After the initial quenching, the PL intensity of sample B slowly decreases to 78% of the initial value in 2 h, while that of sample C is almost constant. When the excitation wavelength is 450 nm, the degradation is much smaller for both the samples. Especially, sample C does not show any degradation of the PL. It should be stressed here that CdSe and CdTe nanocrystals in water, often regarded as photostable materials, degrade more rapidly by continuous irradiation (more than 50% decrease in 100 min).<sup>112,113</sup> Therefore, we can conclude that

codoped Si nanocrystals, especially large nanocrystals, possess remarkably high photostability. Hereafter, we focus mainly on sample B to further study the PL stability in different environment because it is relatively more vulnerable than samples with larger nanocrystals and has the highest PL-QY.

To investigate the mechanism of the PL degradation, we introduce a short break in the middle of the continuous excitation. Figure 4-3 (c) shows the PL intensity of sample B under continuous excitation at 450 nm for 1 h with a 3 min break in the middle. The PL intensity fully recovers after the 3 min break, indicating that the PL quenching is not due to structural changes such as photo-oxidation commonly observed for colloidal nanocrystals with organic ligands. A plausible explanation of the temporal decrease under continuous light irradiation is due to charging (ionization) of Si nanocrystals caused by capturing of either electrons or holes to traps on the surface. It is noted here that, although initial fast quenching is fully recovered, gradual quenching observed in Figure 4-3 (a) at 365 nm is not recovered after the break. The gradual quenching may be due to defect formation by photo-oxidation.

Figure 4-3 (d) shows the PL-QY of sample B as a function of storage time in dark. The PL-QY starts to decrease after 20 days and reaches 90% of the initial value after 27 days. However, even after 40 days, the QY of codoped Si nanocrystals is 6.5% (64% of the initial value). A possible mechanism of slight degradation is the formation of defects by oxidation in water. As shown in the inset, the PL spectral shape and the peak wavelength do not change even after 40 days. Compared to previously reported Si nanocrystals in water, the degree of degradation of codoped Si nanocrystals is very

small. For example, the PL intensity of poly-acrylic acid grafted Si nanocrystals decreases up to 80% of the initial value within 5 days in dark.<sup>107</sup>

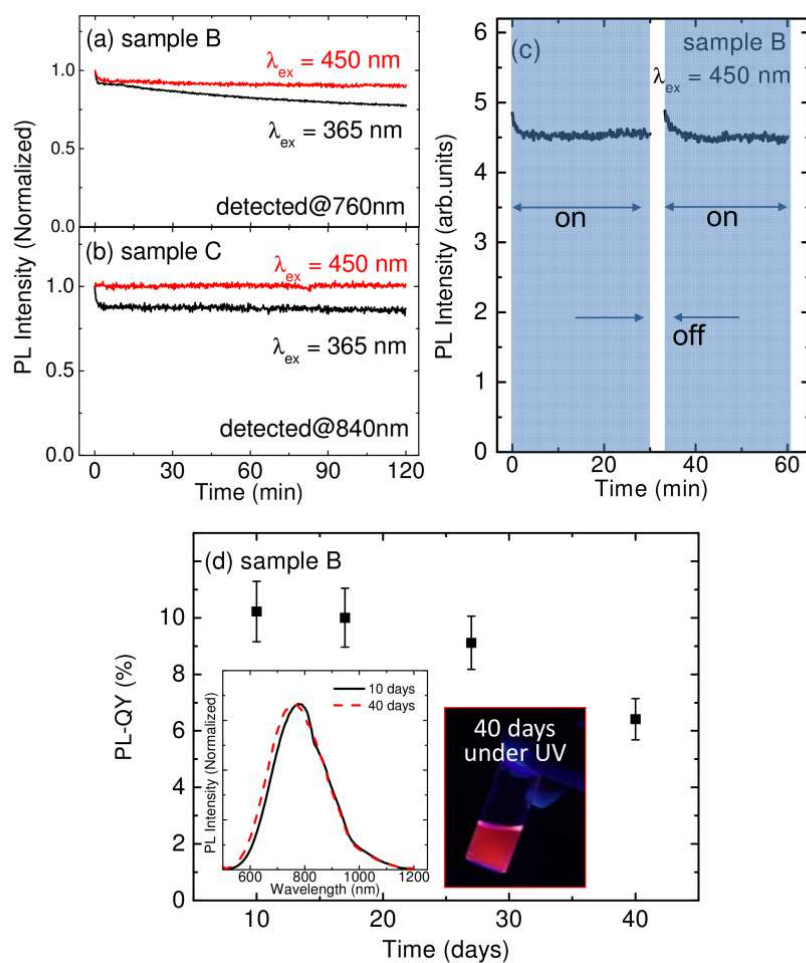


Figure 4-3 Temporal evolution of the PL intensity of (a) sample B and (b) sample C under continuous excitation at 365 and 450 nm. (c) Temporal evolution of the PL intensity of sample B under continuous excitation at 450 nm with a 3 min break. (d) PL-QY of sample B as a function of storage term in the dark in water. The inset is normalized PL spectra after storage for 10 and 40 days. The photograph is the sample after 40 days under UV excitation.



The pH stability of codoped colloidal Si nanocrystals in water is examined. Figure 4-4 (a) shows the optical absorbance at 360 nm and 1000 nm (sample B). The absorbance value at 360 nm, which is roughly proportional to the amount of Si nanocrystals in water, is almost constant in the wide pH range. The absorbance value at 1000 nm, which represents the scattering loss, is almost 0 in the pH range. These results indicate that no agglomerates and precipitates are formed and almost the same amount of Si nanocrystals is dispersed in the pH range of 2–10. Figure 4-4 (b) shows zeta-potentials of codoped Si nanocrystals in water (sample D) as a function of pH. In this pH range, zeta-potentials are negative. As the pH value increases, the zeta-potential decreases from -23 mV to -45 mV. This is a typical behavior of nanocrystals with negatively charged surface. At lower pH, the negative potential arising from the surface of nanocrystals is cancelled by  $H^+$  ions in an aqueous solution. This results in the small absolute value of zeta-potential. On the other hand, at higher pH,  $OH^-$  ions become the potential-determining ions. In such a pH range, the absolute value of zeta-potential becomes large. In codoped colloidal Si nanocrystals, the absolute value of the zeta-potential is 23 mV even at pH = 2. This value is usually considered to be high enough for colloidal stability. This is consistent with the pH-independent optical absorbance in Figure 4-4 (a).

Figure 4-4 (c) and (d) show PL intensity and PL lifetime detected at 760 nm, respectively, as a function of pH. The PL intensity is stable at low pH (< 4) and then decreases by 20-30% in the pH range of 5-8. On the other hand, PL lifetimes are almost constant in the pH range of 2–8. This suggests that the number of Si nanocrystals contributing to the PL decreases in the pH range of 5–8, although the reason is not clear.

In the pH range larger than 8, the intensity decrease is accompanied by the shortening of the lifetime. Non-radiative centers are thus considered to be introduced in or on the surface of Si nanocrystals in the pH range. A possible origin is defects on the surface generated by etching the surface with alkalized solution.

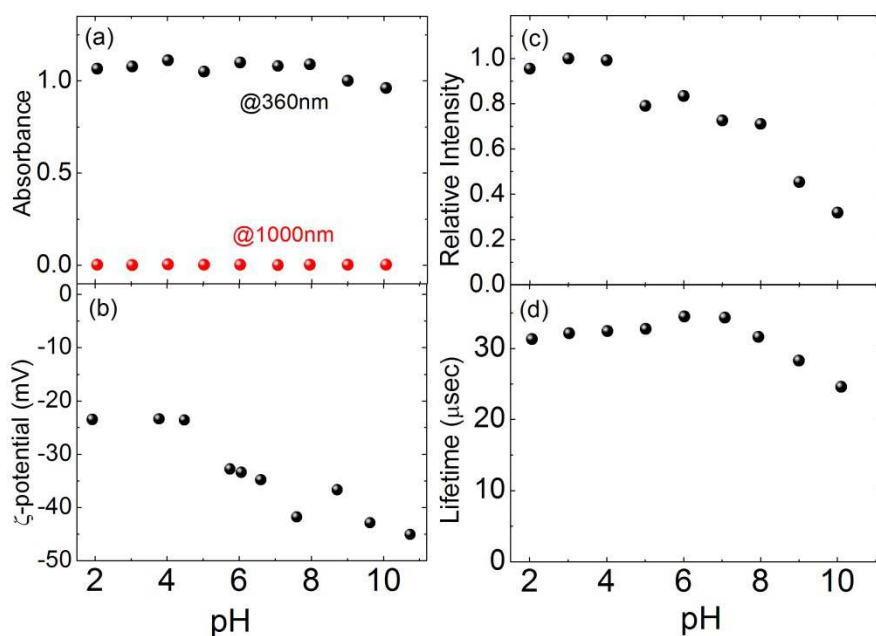


Figure 4-4 pH dependence of (a) absorbance at 360 and 1000 nm, (b)  $\zeta$ -potential, (c) normalized PL intensity and (d) PL lifetime detected at 760 nm

## 4-4 Conclusion

We have succeeded in producing Si nanocrystals having excellent stability in an aqueous solution without organic-ligand passivation by simultaneously doping P and B. The codoped Si nanocrystals in water exhibit bright size-tunable PL in a biological window (700-1000 nm) with the lifetime of 20–120  $\mu$ sec. The maximum PL-QY reaches 10.2 % at 760 nm. The codoped colloidal Si nanocrystals show high photo- and pH stability in water. The present results suggest that codoped colloidal Si nanocrystals are a very suitable material for the contrast agents in biological imaging.

## Chapter 5

# Plasmonic-Coupled Nanocomposites Based on Gold Nanorods Decorated with Si Nanocrystals

### 5-1 Introduction

The combination of plasmonic nanoparticles and light-emitting semiconductor nanocrystals into a single multifunctional colloidal platform provides a novel opportunity for the biocompatible nanoscale labels for sensing and, *in vivo* and *in vitro* imaging. Unlike toxic II–VI and IV–VI semiconductors, Si nanocrystals are highly biocompatible. However, colloidal Si nanocrystals coupled to plasmons have been scarcely studied due to that the synthesis of high quality Si nanocrystals with bright emission in biological windows and water-dispersibility is still challenging.

In Chapter 3, we developed water-dispersible Si nanocrystals with size-tunable in biological transparent windows by inorganic surface functionalization. Inorganically functionalized Si nanocrystals are well-dispersed in water and exhibit bright emission in a wide range of pH as well as excellent photostability.

In this chapter, we combine plasmonic nanoparticles and codoped Si nanocrystals. We present a facile synthesis of plasmonic-coupled nanocomposites based on Au nanorods

decorated with Si nanocrystals in an aqueous solution. By systematically investigating their structural and PL properties, we show significant enhancement of spontaneous emission rate with suppressed non-radiative quenching. In addition, through a comparison of the polarization dependence of PL and scattering intensities of single nanocomposites, we successfully demonstrate that the emission from Si nanocrystals coupled to Au nanorods is highly polarized along the major axis of nanorods. From a systematic PL analysis performed in partnership with rigorous theoretical calculations, we demonstrate a quantum efficiency enhancement of Si nanocrystals up to a factor of 3.

## 5-2 Materials and Methods

Colloidal Si nanocrystals of two different sizes were prepared by the method described in Chapter 2. The average diameters of Si nanocrystals grown at 1075 and 1150 °C were  $3.3\pm0.9$  and  $4.6\pm1.3$  nm, respectively (see Figure 5-1). Positively-charged polymer-coated Au nanorods (A12-40-750-POS) were purchased from Nanopartz Inc. (Loveland, CO) and used as received. A representative TEM image is shown presented in Figure 5-1 (c). The average length and width of the nanorods were  $131\pm8$  and  $57\pm5$  nm, respectively. A uniform polymer layer can be seen in the inset. The average thickness of the polymer layer is approximately 8 nm, which plays a crucial role for plasmonic-coupling between nanocrystals and nanorods.

Codoped Si nanocrystals are negatively charged (-25 mV in water at pH 7) and Au nanorods are positively charged (+35 mV in water at pH 7). Therefore, by mixing 25  $\mu$ L of Si nanocrystal solution ( $1 \times 10^{16}$  nanocrystals/mL) with 1.5 mL of concentrated Au nanorod solution ( $1.7 \times 10^{10}$  nanorods/mL) for 2 days, nanocrystals attach to the surface of the nanorods by electrostatic interaction. The mixed colloidal solution was subjected to centrifugation to remove unattached nanocrystals, and nanocrystal-decorated Au nanorods were redispersed in DI water.

TEM observations (Tecnai Osiris, FEI) were performed for carbon-coated TEM meshes on which the solution containing Si nanocrystals-decorated Au nanorods was drop-cast. Absorption spectra of nanocrystals and nanorods were acquired with a spectrophotometer (CARY 5000, Varian). Dark-field scattering and PL images of composites were obtained using an inverted microscope (IX71, Olympus) equipped with a high-resolution electron multiplying charge coupled device (EMCCD) (iXonEM, Andor). For dark-field measurements, the samples were illuminated through an air dark-field condenser. To obtain PL images, a 100 W mercury lamp (U-LH100HG, Olympus) with 10 nm bandpass filter centered at 430 nm was used as an excitation source. The excitation light was filtered using proper longpass filter and only emission from composites was detected by CCD. In this condition, Au nanorods without Si nanocrystals do not show any PL in the images. Polarization-dependence of scattering and PL images were taken with a polarization analyzer placed in front of the detector. The linear profile of each bright spot on the images was analyzed and the peak values were used for intensity comparison. Photoluminescence spectra and decay dynamics were measured using a monochromator (Oriel Cornerstone 260, Newport) and

photomultiplier tubes for visible (Oriel 77348, Newport) and NIR (R5509-73, Hamamatsu) regions. The excitation source was electrically-modulated light from laser diode of 405 nm (IQ1A-100, Power Technology Inc.). All the measurements were carried out at room temperature.

### 5-3 Results and Discussion

Figures 5-1 summarize the optical properties of Si nanocrystals with two different sizes and Au nanorods in water. The nanocrystals with 3.3 and 4.6 nm diameter exhibit the broad spectra peaked at 750 and 850 nm, respectively. In the following, we refer to the nanocrystals emitting at two different wavelengths as nanocrystals-750 and nanocrystals-850. We find that the longitudinal LSPR of Au nanorods at 750 nm well-overlaps with the PL spectra in particular of nanocrystals-750. The weak transverse mode is also observed at 525 nm. The absorption of Si nanocrystals appears around 650 nm that is enough far from the resonance of longitudinal modes of Au nanorods.

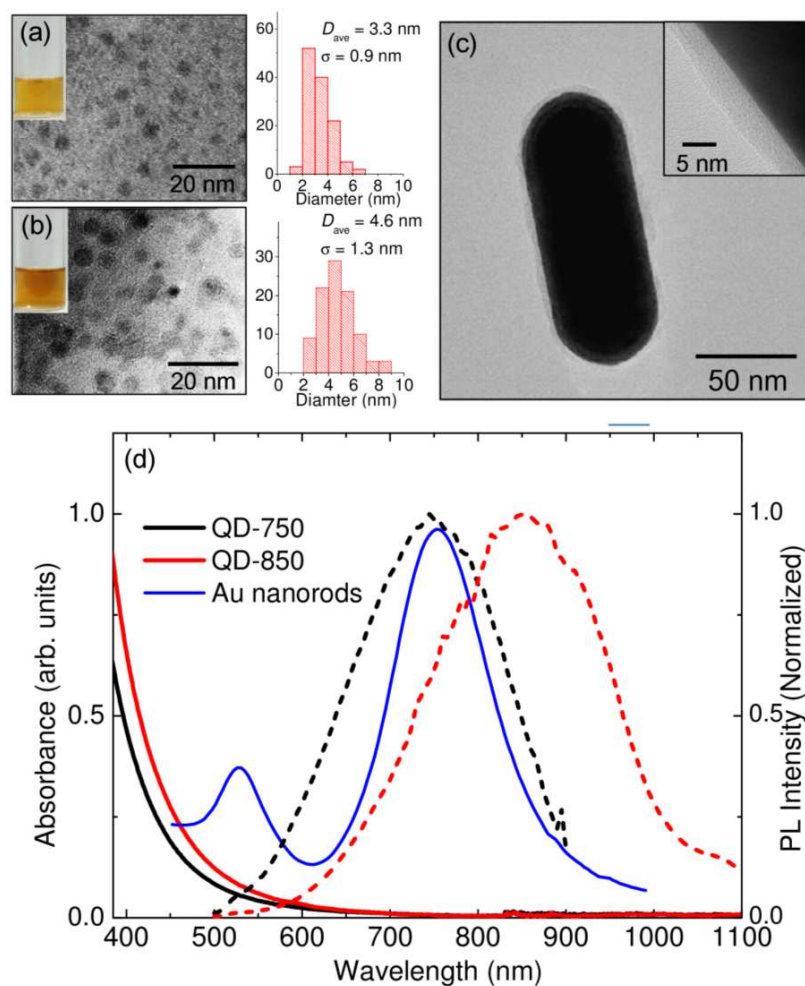


Figure 5-1. (a), (b) Photographs and TEM images of Si nanocrystals with different size. (c) TEM image of a positively-charged polymer coated Au nanorod. The inset shows a nanorod coated by polymer layer. (d) Absorption (solid) and normalized PL spectra (dashed) of Si nanocrystals-750 (black), Si nanocrystals-850 (red), and Au nanorods (blue).



In Figure 5-2, we compare the extinction spectra of Au nanorods in water before and after decoration with Si nanocrystals. The longitudinal mode exhibits a slight red-shift of 6 nm. This is consistent with previous results<sup>55</sup> and attributed to the modification of the local refractive index induced by the attachment of the nanocrystals. The quantification of the modification of local refractive index is difficult because of unknown effective refractive index of Si nanocrystal layers. Figure 5-3 shows a representative TEM image of a single Au nanorod decorated with Si nanocrystals that are attached on the surface of the nanorod by electrostatic attraction in solution. In both high-resolution TEM images in Figure 5-3, the lattice fringes corresponding to {111} planes of Si crystal can be clearly observed. These images demonstrate that single-crystalline Si nanocrystals are attached to the Au nanorods. The average separation between nanocrystals and nanorods estimated by inspecting several TEM images (shown in Figure 5-3) is 8.7 nm. Figures 5-4 (a) and (b) show the dark-field scattering and PL images collected from the same region of nanocrystals-850 coupled to Au nanorods. The bright spots in the images correspond to the spatial locations of the composites. Since the scattering and PL signals originate from the same locations, they demonstrate the formation of active (light-emitting) nanocomposites driven by the scattering of the nanorods. However, few spots in the scattering cannot easily be co-located in the PL images, due to the small PL signal that is originated by a reduced number of nanocrystals at such particular locations.

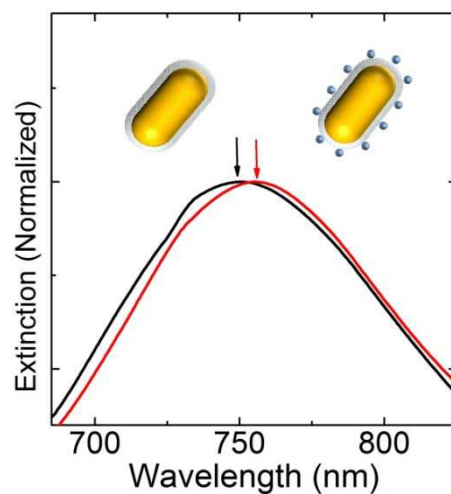


Figure 5-2. Longitudinal LSPR peak of Au nanorods before and after decoration with nanocrystals-850.

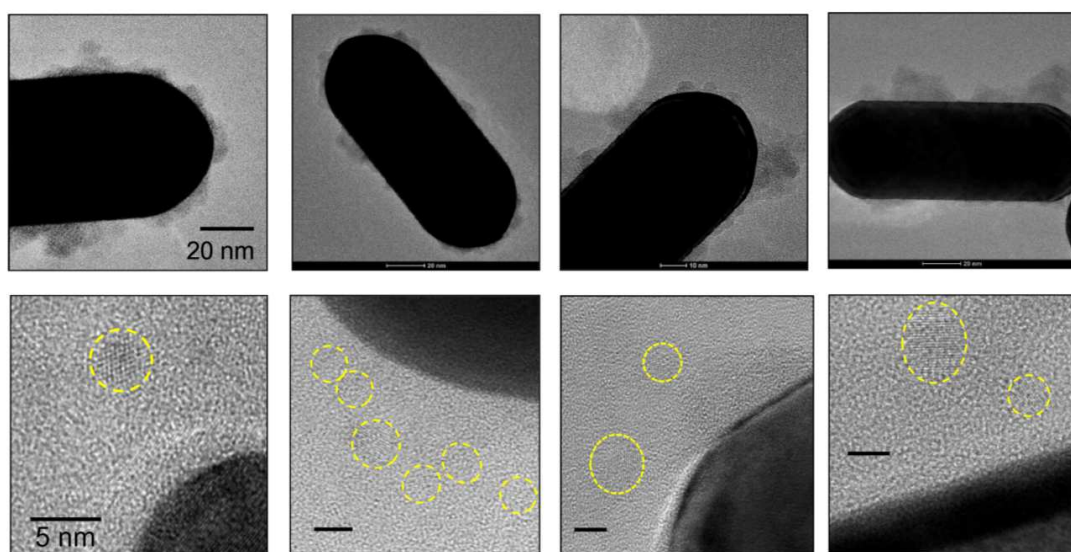
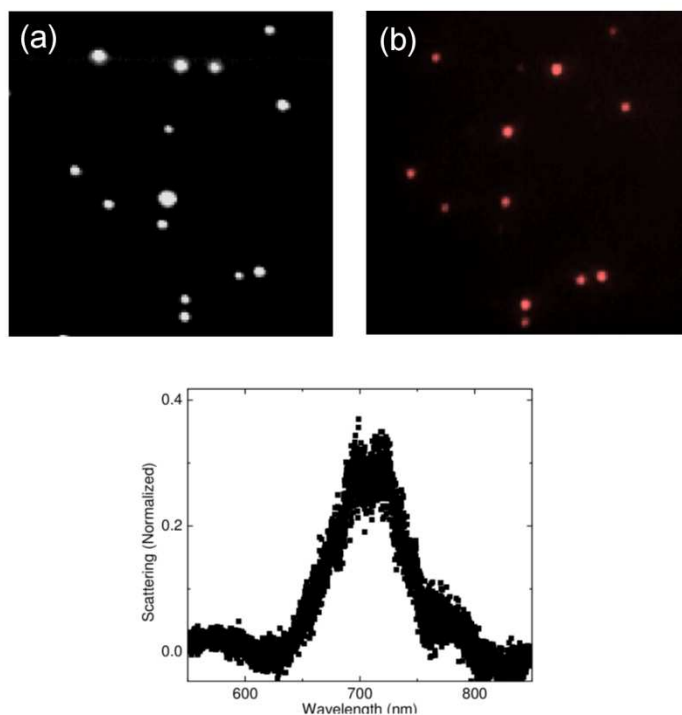


Figure 5-3. (Upper row) TEM images of Au nanorods decorated with Si nanocrystals. (bottom row) High-resolution TEM images of composites show single-crystalline Si nanocrystals attached to a nanorod surface with separation by polymer spacer.



*Figure 5-4. (a) Dark field scattering and (b) PL images of nanocomposites of Au nanorods and Si nanocrystals-850 collected at the same region. The bottom figure shows the representative scattering spectrum from a single Au nanorod.*

Figure 5-5 (a) and (b) display normalized PL spectra of Au nanorods decorated with Si-nanocrystals-750 and Si-nanocrystals-850. We also plot the PL spectra of reference (Si nanocrystals without nanorods in water) and extinction spectra of Au nanorods. To investigate the spontaneous emission rate of nanocrystals coupled to Au nanorods, we measured the PL decay curves in a wide wavelength range. Representative decay curves measured at 750 nm are shown in the inset of Figure 3a and b. We observe that even for the nanocrystals that are not coupled with nanorods, the PL decay curves are not single-exponential functions because of the inhomogeneity introduced by surface

defects and impurity doping.<sup>103</sup> In this work, a stretched exponential function,  $I = I_0 \exp [-(t/\tau)]^\beta$ , where  $\tau$  is the measurable decay constant and  $\beta$  is the stretching parameter of the decay, is used to estimate the lifetime of Si nanocrystals with and without Au nanorods, which can be expressed by the Laplace transform of the decay rate distribution. The fitted  $\beta$  values varied from 0.55 to 0.85 for nanocrystals coupled to nanorod, indicating a significant distribution of decay rates for each emission wavelength. According to the stretched exponential theory, an average lifetime can be defined as  $\tau_{\text{ave}} = \tau \beta^{-1} \Gamma(\beta^{-1})$ , where  $\Gamma$  is the Euler gamma function.<sup>114</sup> In Figure 5-5 (c) and (d), we plot the average lifetimes of nanocrystals with and without Au nanorods as a function of the detection wavelength. The lifetime of Si nanocrystals increases monotonically with increasing the detection wavelength, as reported in the literature.<sup>19,115,24</sup> When the nanocrystals are coupled to Au nanorods, the trend of lifetime is different from that of Si nanocrystals alone. The lifetime is shorter only in the range of 700–800 nm compared to reference. The overall decrease of lifetimes of nanocrystals-850 is observed in Figure 5-5 (d). To remove the intrinsic dependence of the nanocrystal lifetimes on wavelength, we approximate the decay rate with  $\Gamma_{\text{ave}} = \tau_{\text{ave}}^{-1}$  and calculate the enhancement factors by considering the ratio of decay rates of nanocrystals with and without Au nanorods. The decay rate enhancement values are shown in Figure 5-5 (e) and (f), which show a clear dependence on the emission wavelength due to the coupling with nanorods for both samples. The maximum enhancement reaches approximately 1.4 for nanocrystals-750 and 3.4 for nanocrystals-850. We notice that the measured enhancement values are larger where the PL spectra overlap with the longitudinal mode scattering spectrum of the LSPR of the

nanorods. In Figure 5-5 (e), at emission wavelength on either side of the peak, the decay rate enhancement factor approaches unity. This indicates that, irrespective of wavelength, the non-radiative energy transfer commonly observed for emitters positioned very close to metal (2-5 nm) surfaces<sup>116,117</sup> is suppressed by the presence of the polymer spacer layer. We performed the same measurements for nanocrystals-750-decorated Au nanorods using a thinner polymer layer (see Figure 5-6). In this case, the decay rate enhancement is approximately 3.5 for the overall PL spectrum. This proves that non-radiative decay channels are dominant for this sample. The decay rate enhancement of nanocrystals-850 in Figure 5-5 (f) also follows the extinction spectrum of the Au nanorods, but it is still greater than one (*i. e.*, 1.8) even at wavelengths detuned from the resonance of Au nanorods. One possible explanation for this behavior is the agglomeration of nanocrystals around the surface of nanorods, resulting in increased non-radiative recombinations.

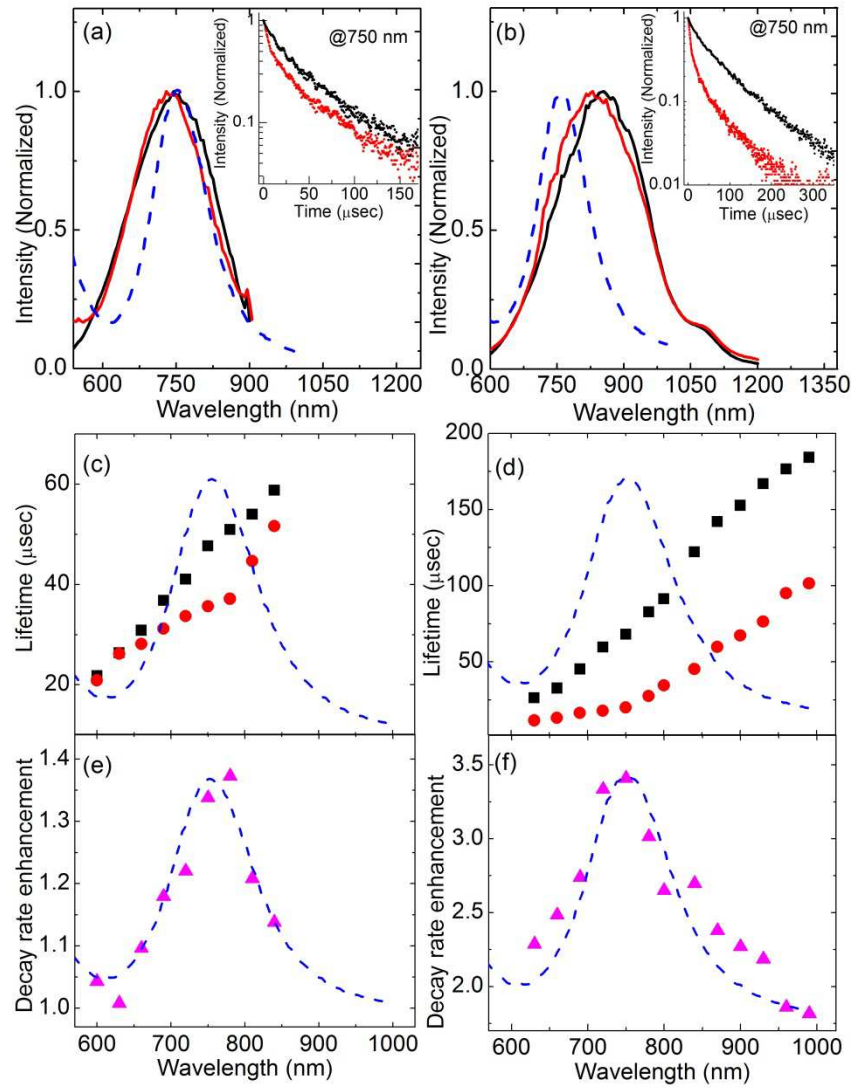
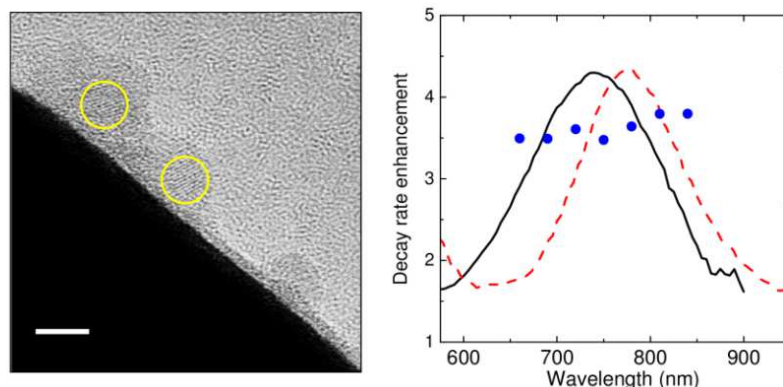


Figure 5-5. Normalized PL spectra of (a) nanocrystals-750 and (b) nanocrystals-850 coupled with Au nanorods (red line). Black and blue lines represent reference PL spectra of nanocrystals in water and extinction spectra of Au nanorods, respectively. Inset: Representative decay curves detected at 750 nm. (c), (d) Average PL lifetimes and (e), (f) decay rate enhancement of nanocrystals-750 (c, e) and nanocrystals-850 (d, f) as a function of emission wavelength. Black squares and red circles in (c) and (d) are results for reference and nanocrystals-decorated Au nanorods.



*Figure 5-6 (Left) TEM image and decay rate enhancement of nanocrystals-750 with CTAB-coated Au nanorods. The spacer thickness is  $\sim 2$  nm and much thinner than the samples shown in the main text. The scale bar is 5 nm. (Right) Decay rate enhancements (blue) of the sample. PL (black) and extinction (red) spectra are also shown in the figure.*

To further understand the coupling between nanocrystals and nanorods, we study the polarization properties of the PL of composites. The detail of data analysis is shown in Figure 5-7. Figures 5-8 (a)-(d) show the dark-field scattering ((a) and (b)) and PL images ((c) and (d)) of nanocrystals-Au nanorod composites collected from exactly the same locations at two polarization angles that are perpendicular to each other. For both scattering and PL, we find intensity differences of the spots in images with different analyzer angles. The polar plots of the scattering intensities of representative particles as a function of the analyzer angles are shown in Figure 5-8 (e). Since the strong dipolar LSPR of Au nanorods is inherently polarized along their major axis (longitudinal mode), the scattered light from the nanorod is also linearly polarized along the major axis.<sup>118</sup>

Figure 5-8 (f) shows the polar plots of PL intensities of the same nanocomposites. The PL from nanocrystals attached to nanorods is also highly polarized along the major axis of the nanorod. We observed similar features for several spots in the images (see Figure 5-9). The linearly polarized emission from randomly oriented emitters coupled to metal nanostructures was reported for Au nanorods coated with dye-doped silica shells<sup>119</sup> and Si nanocrystals coupled to elongated silver nanoparticles.<sup>58</sup> We notice that the polarization of the emission from a single semiconductor nanocrystal, which in general depends on its shape, is almost isotropic for a spherical nanocrystal.<sup>120,121</sup> TEM images in Figure 5-1 (a) and (b) clearly show the spherical shapes of our Si nanocrystals. However, even in the presence of non-spherical nanocrystals, the emission from an “ensemble” of nanocrystals excited by unpolarized light is expected to be unpolarized due to the random orientation of the nanocrystals.<sup>122</sup>

In Figure 5-8 (g), we confirm this picture by comparing the polarized emission of Si nanocrystals coupled and uncoupled to Au nanorods. The polarized emission from nanocomposites reflects the fact that the PL enhancement of Si nanocrystals due to the plasmon coupling with longitudinal modes of Au nanorods is significantly larger compared to the excitation of the transverse modes. This results in a far field emission that is polarized identically to the scattering of the longitudinal modes of Au nanorods. We will further confirm this interpretation in the next section based on our rigorous electromagnetic modeling results.



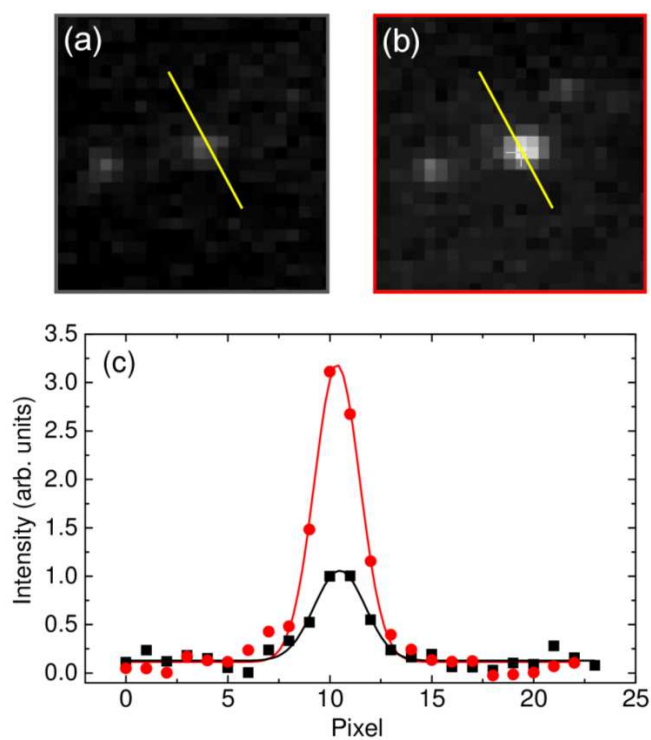


Figure 5-7. (a), (b) Photoluminescence images taken by different polarizations.(c) Linear profiles of spots in the images.

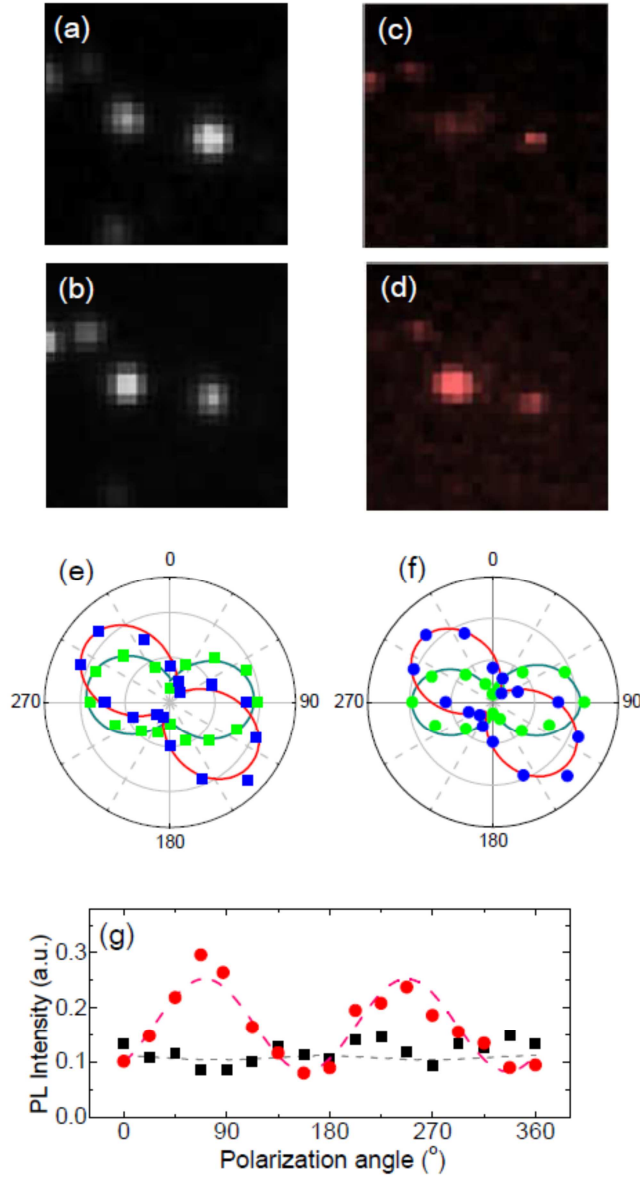
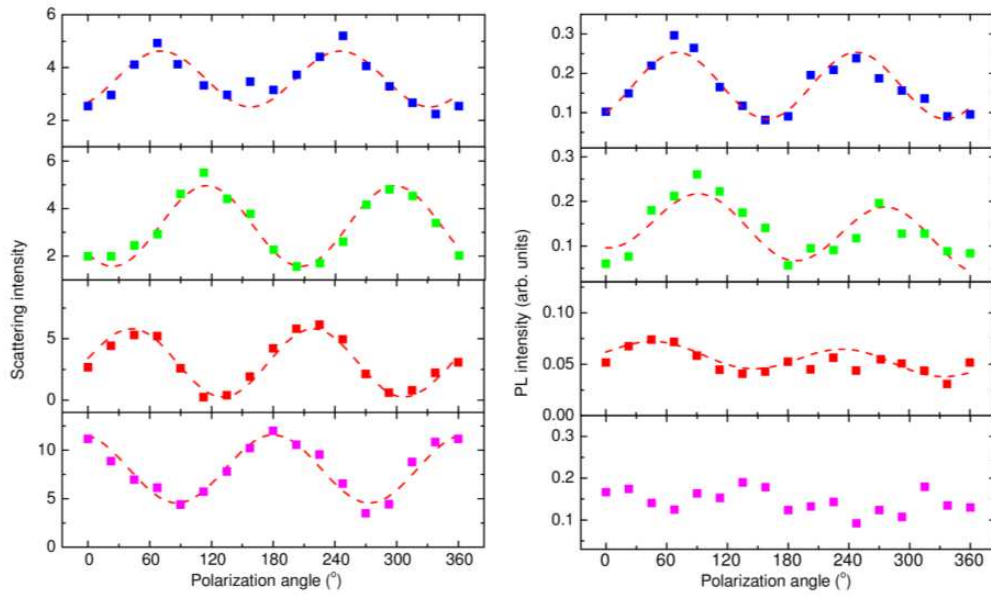


Figure 5-8 (a), (b) Dark-field scattering and (c), (d) PL images of nanocrystals-Au nanorod composites at exactly the same region with different angles of analyzer. The analyzer angles are perpendicular to each other. Polar plots of (e) scattering and (f) PL intensity of representative nanocomposites. Blue and green plots are obtained from identical nanocomposites, respectively. (g) PL intensities of nanocomposites (red) and ensemble Si nanocrystals without Au nanorod (black) as a function of polarization angles.



*Figure 5-9 Scattering and PL intensities as a function of analyzer angles. The plots with same colors are taken from the same particles in microscope images. Dashed line shows the fitting curves by using a cosine squared function. The particle shown in the bottom (magenta) does not show clear polarization dependence in PL. This might be due to the distribution of polymer thickness and the position of nanocrystals on the nanorod surface.*

The enhancement of spontaneous emission rate in Figure 5-5 is explained by the enhancement of LDOS due to the LSPR of Au nanorods. To discuss the contribution of the radiative and non-radiative rates as well as the quantum efficiency of Si nanocrystals-decorated Au nanorods, we performed theoretical calculations using the MNPBEM code,<sup>123</sup> which is based on the rigorous boundary element method. The decay rates in the vicinity of Au nanorod with diameter of 60 nm and length of 126 nm have been simulated by placing point dipoles at fixed distances from the nanorod surface with tabulated dispersion data.<sup>124</sup> The results are normalized by the emission

rate of a dipole in water, and thus we use the term radiative and non-radiative rate enhancements to describe the modification of decay rate due to the presence of Au nanorod. In Figure 5-10 (a), we demonstrate a good agreement between the extinction spectra for Au nanorods obtained from experiment and the simulation. Figure 5-10 (b) shows both radiative and non-radiative rate enhancements of single dipole placed at 10 nm from the top and side of Au nanorod as a function of wavelength. The results are averaged over all dipole orientations. The largest enhancement of radiative rate is observed when the dipole is placed at the top of nanorods. On the opposite, when the dipole is positioned along the side of nanorods, its radiative rate is small and comparable to non-radiative rate at 750 nm. It is also worth noting that the radiative and non-radiative rate enhancement values, which determine the overall quantum efficiency of the plasmonic-coupled system,<sup>125,126</sup> strongly depend on the orientation of dipoles. To discuss the quantum efficiency of the dipoles with different orientation, we compare the ratio of radiative to total decay rate enhancement, called the antenna efficiency.<sup>125,126</sup> In Figure 5-10 (c), we plot the results of oriented parallel (solid) and perpendicular (dashed) to the major axis of nanorods. For dipoles placed at the side of nanorod (black curves), the efficiency is comparable for both orientations. On the other hand, we find a dramatic change in the efficiency when a dipole at the top is oriented parallel to the major axis of the nanorod. This explains our experimental results of emission polarization in Figure 5-8 (f). In the case of nanocrystals attached at the top of the nanorod, the PL intensity becomes much larger when the analyzer is positioned parallel to the major axis of nanorods. The polarization selective PL enhancement may improve the sensitivity and performance of bioimaging.

In our samples, nanocrystals are randomly located on the surface of Au nanorod. Therefore, we also took into account the relative effect of dipole positions around the nanorod, and obtained the positionally-averaged decay rates shown in Figure 5-10 (c). We notice that around the emission peak of nanocrystals-750, the radiative rate enhancement is about 2 times larger than the non-radiative rate enhancement. Therefore, in nanocomposite of nanocrystal-Au nanorods, a significant quantum efficiency enhancement of nanocrystals can be obtained. The non-radiative decay becomes dominant at wavelengths shorter than 650 nm, which corresponds to the excitation region of the transverse scattering mode of the nanorods.

In order to quantitatively determine the quantum efficiency enhancement, we will now combine the experimental and theoretical results. We focus on the nanocrystals-750 sample because the PL spectrum of nanocrystals-750 fully overlaps with the LSPR of Au nanorods. The intrinsic quantum efficiency ( $Q_0$ ) of Si nanocrystals is expressed as  $Q_0 = \gamma_r^0 / (\gamma_r^0 + \gamma_{nr}^0)$ , where  $\gamma_r^0$  and  $\gamma_{nr}^0$  are the intrinsic radiative and non-radiative decay rates of nanocrystals in aqueous solution. The quantum efficiency of nanocrystals coupled to Au nanorods ( $Q_m$ ) is defined by:

$$Q_m = \frac{\Gamma_r}{\Gamma_r + \Gamma_{abs} + \gamma_{nr}^0} \quad (1)$$

Here,  $\Gamma_r$  is the modified radiative rate, and  $\Gamma_r / \gamma_r^0$  corresponds to the Purcell factor<sup>127–129</sup> with respect to the emission of a dipole in water and  $\Gamma_{abs}$  is the plasmon-induced non-radiative rate due to the absorption by the metallic nanorods. In eq 1, we assume that only the radiative rate is modified by the coupling with Au nanorods because the intrinsic non-radiative rate ( $\gamma_{nr}^0$ ) arising from material

imperfections of Si nanocrystals is not affected by the local electromagnetic environment.<sup>130,131</sup> In fact, the decay rate enhancement of nanocrystals-750 shown in Figure 5-5 (e) is almost unity at wavelengths that are detuned from the resonance of Au nanorods. This confirms that the measured decay rate enhancement is due to  $\Gamma_r/\gamma_r^0$  (Purcell enhancement) and  $\Gamma_{\text{abs}}/\gamma_r^0$  (absorption by Au nanorods) rather than modification of internal non-radiative rate of Si nanocrystals by coupling with nanorods. By combining the experimentally obtained total decay rate enhancement ( $W_{\text{total}}$ ) shown in Figure 5-5 (e) with the  $\Gamma_r/\gamma_r^0$  and  $\Gamma_{\text{abs}}/\gamma_r^0$  values obtained from the simulations in Figure 5-10 (c), we can calculate  $Q_0$ ,  $Q_m$  and the enhancement of the quantum efficiency of Si nanocrystals. We can determine the QE enhancement of Si nanocrystals induced by Au nanorods, which is given by:

$$\frac{Q_m}{Q_0} = \frac{\Gamma_r}{\Gamma_r + \Gamma_{\text{abs}} + \gamma_{nr}^0} \times \frac{\gamma_r^0 + \gamma_{nr}^0}{\gamma_r^0} \quad (2)$$

From the definition of total decay rate enhancement, which is

$$W_{\text{total}} = \frac{\Gamma_r + \Gamma_{\text{abs}} + \gamma_{nr}^0}{\gamma_r^0 + \gamma_{nr}^0}, \quad (3)$$

the QE enhancement of Eq (2) can be simply expressed as:

$$\frac{Q_m}{Q_0} = \frac{\Gamma_r/\gamma_r^0}{W_{\text{total}}} \quad (4)$$

In Table 5-1, we summarize the results of emission at 750 nm which is the nanocrystal emission peak. By coupling with Au nanorods, we found that the quantum efficiency of

nanocrystal emission is enhanced by a factor of 2.8. We notice that this large enhancement is achieved only by engineering the radiative decay rate without the contribution from excitation enhancement (pumping enhancement). We also observe that the calculated  $Q_0$  is in excellent agreement with measured PL quantum yield ( $6.9 \pm 0.7\%$ ) of our Si nanocrystals in water,<sup>132</sup> which proves the validity of our analysis.

Finally, we discuss the perspective of the nanocrystal-Au nanorod composite. In this system, there are two determining factors for radiative rate enhancement, which are the nanocrystal location on the nanorod and their separation distance from the nanorod. In Figure 5-10 (e), we plot the quantum efficiency enhancement that can be obtained considering the emission of nanocrystals with  $Q_0 = 7.4\%$  (at 750 nm) as a function of their separation from the surface of a nanorod. The radiative and non-radiative rate enhancement as a function of emission wavelength is shown in Figure 5-11. The nanocrystal orientation and location around the surface of the nanorod have been averaged. We found that there exists an optimal separation distance is in the range of 7.5 nm to 12.5 nm, which is very similar to the conditions of our samples. Figure 5-10 (f) shows the quantum efficiency enhancement factors as a function of the intrinsic quantum efficiency of nanocrystals. We plot both dipole position-averaged values as well as the case of a single dipole located at the top of the nanorod. From the curves of position-averaged result, we demonstrate quantum efficiency enhancement in a wide range of values for the intrinsic quantum efficiency. This means that even in the case of emitters with significantly larger values of intrinsic quantum efficiency, the proposed plasmonic-coupled composites give rise to emission enhancement, especially when the emitters are located atop the nanorods. The selective binding of active molecules on top

of nanorods has been already reported.<sup>133–135</sup> Although this work has been limited to Si nanocrystals with low intrinsic quantum efficiency, the results of our numerical analysis demonstrate the applicability of the nanorod composite approach to other emitting materials that feature larger values of intrinsic quantum efficiency.

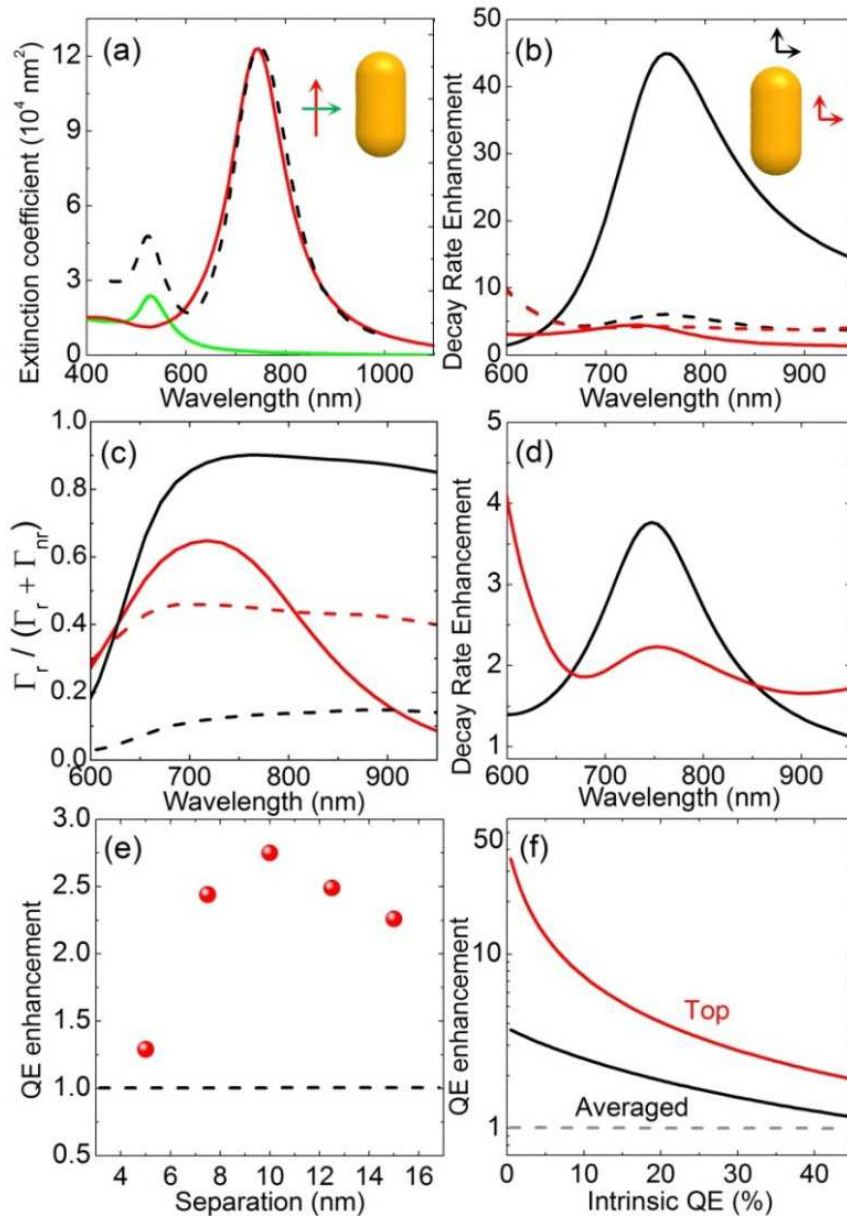




*Figure 5-10 (a) Calculated extinction coefficient (solid line) of Au nanorod excited by plane waves with two different polarization (red and green curves) and measured extinction spectrum (dashed line). (b) Calculated radiative (solid line) and non-radiative (dashed line) decay rate enhancements of dipole placed at 10 nm from the top (black) and side (red) of Au nanorod. The results are normalized by the radiative rate of dipole in water and orientationally averaged. (c) Ratio between radiative ( $\Gamma_r$ ) and total decay rate enhancement ( $\Gamma_r + \Gamma_{nr}$ ) of dipoles oriented parallel (solid) and perpendicular (dashed) to the long axis of nanorods. Black and red curves represent the results of dipoles placed 10 nm from the top and side of nanorods, respectively. (d) Both position- and orientation-averaged radiative (black) and non-radiative (red) decay rate enhancements. (e) Quantum efficiency enhancement as a function of separation between emitters and nanorods. (f) Quantum efficiency enhancements as a function of intrinsic quantum efficiency. Black and red curves represent position-averaged results and the case of a dipole placed at the top of the nanorod, respectively.*

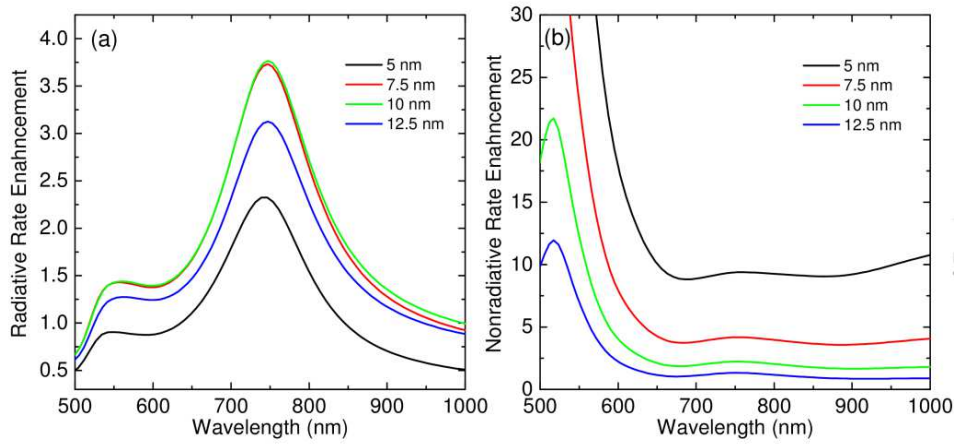


Figure 5-11 (a) Radiative and (b) non-radiative rate enhancement with different spacer thicknesses.

Table 5-1 Parameters of emission of Si nanocrystals at 750 nm. Measured total decay rate enhancement ( $W_{exp}$ ), radiative ( $\Gamma_r/\gamma_r^0$ ) and non-radiative ( $\Gamma_{abs}/\gamma_r^0$ ) decay rate enhancements from simulation, calculated intrinsic ( $Q_0$ ) and modified ( $Q_m$ ) quantum efficiencies, and calculated quantum efficiency enhancement.

$\lambda$ (nm)	$W_{exp}$	$\Gamma_r/\gamma_r^0$	$\Gamma_{abs}/\gamma_r^0$	$Q_0$ (%)	$Q_m$ (%)	$Q_m/Q_0$
750	1.35	3.77	2.23	7.4	20.7	2.8

## 5-4 Conclusion

We have developed a novel plasmon-coupled light emitting platform based on Au nanorods decorated by Si nanocrystals. Through time-resolved PL measurements performed over a wide range of wavelengths, we have shown enhanced decay rates that follow the LSPR scattering spectrum of nanorods and tunable coupling efficiency of Si nanocrystals with colloidal Au nanorods. The PL imaging and scattering maps of single nanocomposites demonstrate that the emission of Si nanocrystals is polarized and driven by the efficient excitation of the longitudinal mode of Au nanorods. From a systematic PL analysis performed in partnership with rigorous theoretical calculations, we demonstrate a quantum efficiency enhancement of Si nanocrystals up to approximately a factor of 3. To the best of our knowledge, this is the first experimental demonstration of plasmon-coupled nanocomposites based on Si nanocrystals in an aqueous solution. Si-based plasmon-coupled nanocomposites prepared by facile and cost-effective method are promising candidates for the development of biocompatible fluorescent nanoprobe of interest to biosensing and bioimaging technologies.

## Chapter 6

# Enhanced Photoluminescence of Si Nanocrystals Doped Cellulose Nanofibers

### 6-1 Introduction

Polymer nanofibers prepared by electrospinning are cheap, flexible and biocompatible platforms for manipulating light at the nanoscale in nanophotonic and biophotonic applications.<sup>136,137</sup> The elegance of electrospinning technique relies on its simplicity and solution-based process in the absence of additional harsh chemicals and precisely controlled environment (pressure, temperature, *etc.*) that are traditionally required for most nanofabrication techniques. Light-emitting active nanofibers doped with semiconductor nanocrystals<sup>138,139</sup> or organic dyes<sup>140</sup> have particularly attracted much attention due to their wide range of applications including waveguides,<sup>141–143</sup> light-sources,<sup>144–146</sup> optical sensors.<sup>138,147,148</sup>

It is well-known that plasmonic nanostructures such as Au and Ag nanoparticles and nanorods can modify the emission properties of emitters located in their close proximity.<sup>48,149</sup> By carefully designing the material and structure, enhanced emission of nanocrystals coupled to localized surface plasmon resonance (LSPR) of metal

nanoparticles has been demonstrated.<sup>47,49</sup> This is also applicable to nanocrystals-doped electrospun nanofibers.<sup>150</sup> However, in order to suppress the non-radiative quenching of emitters coupled to metal surfaces or nanoparticles,<sup>151,152</sup> complex fabrication techniques must be developed capable to accurately control the distance between metal nanoparticles and emitters, which is a very challenging task.

In this work, using the cost-effective electrospinning technique, we demonstrate plasmon-enhanced emission in biocompatible light-emitting silicon nanocrystals doped nanofibers. The combination of water-based hydroxypropyl cellulose (HPC) polymer precursor and nontoxic Si nanocrystals emitting in the biological window (650–1300nm) enables the fabrication of all-biocompatible active nanofiber systems. Furthermore, we engineer the light-emission properties of the nanofibers by codoping them with plasmonic nanoparticles. By performing photoluminescence (PL) spectroscopy of codoped nanofibers with and without metal nanoparticles, we successfully demonstrate plasmon-driven PL enhancement by a factor of 2.2 in the absence of non-radiative quenching due to the strong scattering of excitation light by Au nanoparticles in side nanofibers.

## 6-2 Experimental Results

Colloidal dispersions of Si nanocrystals are prepared by the method described in Chapter 2. Si-rich borophosphosilicate glasses (BPSG) were first deposited by co-sputtering Si, SiO<sub>2</sub>, B<sub>2</sub>O<sub>3</sub>, and P<sub>2</sub>O<sub>5</sub> in an RF-sputtering apparatus. The films were

peeled off from the plates and annealed at 1075 °C in a N<sub>2</sub> gas atmosphere for 30 min to grow Si nanocrystals in BPSG matrices. The Si-nanocrystals were isolated from matrices by dissolving in HF solution (46 wt%). Isolated Si nanocrystals were then transferred to water. In Figure 6-1 (a) we show a photograph of Si nanocrystal dispersion and a TEM (Tecnai Osiris, FEI) image. Si nanocrystals are well-dispersed in water and no agglomerates were observed in the image. The average diameter of Si nanocrystals estimated by TEM was 3.3±0.9 nm.

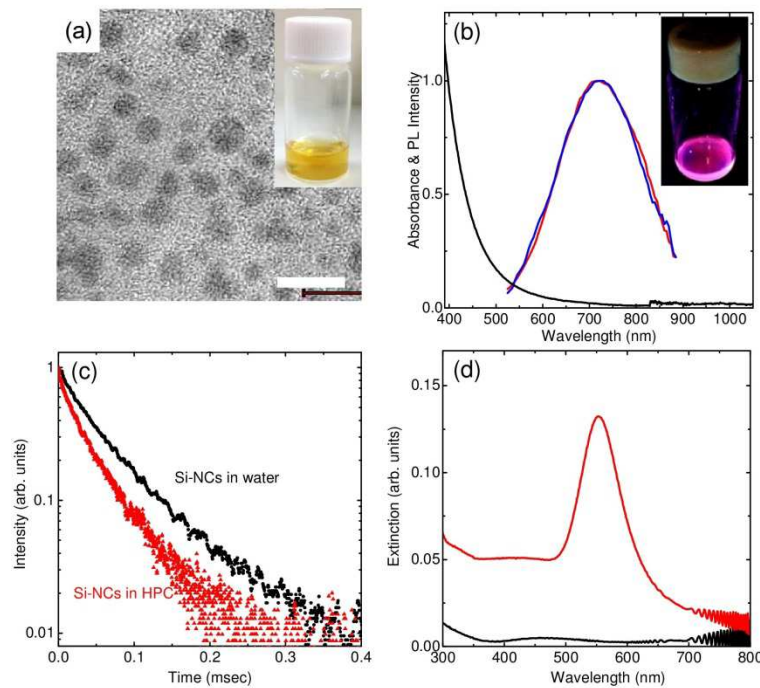


*Figure 6-1 (a) Photograph of colloidal dispersion and TEM image of Si nanocrystals (Scale bar: 10 nm). (b) Absorbance (black) and normalized PL spectra of Si nanocrystals in water (red) and planar HPC film (blue) The excitation wavelength is 488 nm. Inset: Photograph of HPC solution (45 wt%) containing Si nanocrystals under UV excitation (c) PL decay curves of Si nanocrystals dispersed in water and embedded in a HPC film. (d) Extinction spectra of single- (black) and codoped (red) HPC films.*

To prepare the precursor of electrospun nanofibers, we first dissolved HPC in DI water and then added Si nanocrystal solution to the polymer solution, followed by stirring for about 1 h to obtain a homogeneous mixture solution containing 45 wt% HPC and 0.8 mg/mL Si nanocrystals. Photoluminescence spectra were measured using a monochromator (Oriel Cornerstone 260, Newport) and photomultiplier tubes (Oriel 77348, Newport). The excitation source was 488 nm line of an Ar ion laser (Spectra Physics, 177–602). Figure 6-1 (b) shows absorbance and normalized PL spectra of Si nanocrystals in water (red) and in the HPC solution (blue). In the inset, we show a photograph of HPC solution containing Si nanocrystals under UV light excitation, exhibiting bright red luminescence. The Si nanocrystals in HPC solution exhibit a broad PL peaked at 710 nm, which is identical to that observed for Si nanocrystals in water. Figure 6-1 (c) shows the PL decay curves detected at 700 nm of Si nanocrystals dispersed in water and embedded in dried HPC film. The lifetimes of nanocrystals in water and HPC film are 56 and 31  $\mu$ sec, respectively. The difference between them is explained by a higher refractive index of HPC ( $\sim$ 1.56) than that of water (1.33). The emitters in the media with higher refractive index exhibit a larger emission decay rate.

Plasmonic nanoparticles and Si nanocrystals codoped polymer solution was prepared by directly adding concentrated Au nanoparticles (70 nm diameter) synthesized by a seeded growth method to the mixture solution. The concentration of the final mixture solution was 45 wt% HPC with 0.8 mg/mL Si nanocrystals and 1.2 mg/mL Au nanoparticles. In the following, we refer to the sample doped with both Si nanocrystals and Au nanoparticles as codoped sample, and to that doped with Si nanocrystals alone as single-doped sample. In Figure 6-1 (d) we plot the extinction spectra of single-

(black) and codoped (red) HPC films prepared by spin-coating mixture solutions. In the codoped HPC film, the extinction peak originating from LSPR of Au nanoparticles is clearly observed around 550 nm. The slight increase of extinction at a wavelength shorter than 400 nm observed in both spectra is due to the absorption of Si nanocrystals. We notice that in this wavelength range, the absorption (and scattering) of the HPC host film is negligibly small compared to that of Au nanoparticles.

In order to create active nanofibers by electrospinning, the HPC mixture solution was poured into 10 mL Syringe (diameter 18.94 mm) fitted with a 20 gauge stainless steel needle. The syringe was then transferred to an infusion syringed pump (Braintree scientific) with the needle connected to the positive terminal of a high power voltage source (Gamma high voltage). Controlled by the syringe pump, the precursor (45 wt% HPC solution) was pushed continuously to the needle tip with a flow rate of 0.4 mL/h. Driven by the high voltage (18 kV) established in the Taylor cone between the nozzle and metal plate collector, the precursor was ejected from the nozzle creating HPC nanofibers after solvent evaporation. The charged HPC nanofibers are neutralized at the collector (kept 20 cm from the nozzle) where they form random networks of nanofibers. Figure 6-2 (a) shows a representative scanning electron microscope (SEM) image of the electrospun HPC nanofibers codoped with Si nanocrystals and with Au nanoparticles. The average diameter of the nanofibers is 249 nm with the standard deviation of 31 nm. The nanofibers form a relatively uniform film with a thickness of 7.6  $\mu\text{m}$  measured by cross-section SEM analysis. We confirmed the same morphology (*i. e.*, thickness and diameter) of both single- and codoped nanofibers films. In Figure 6-2 (b), we show a TEM image of the codoped system, which demonstrates doping 70 nm Au



nanoparticles within the nanofiber. The TEM image demonstrates that the Au nanoparticles are incorporated into the nanofibers without forming aggregates at this doping concentration. The density of Au nanoparticles (*i. e.*, number of nanoparticles per unit volume) is estimated from TEM analysis to be  $\sim 10^{13} \text{ cm}^{-3}$  in good agreement with the concentration of the precursor solution. The high-resolution TEM image of the nanofiber in Figure 6-2 (c) shows an incorporated Si nanocrystal with lattice fringes corresponding to  $\{111\}$  planes of the Si crystal. Figure 6-2 (d) shows a PL image of Si nanocrystals codoped nanofibers obtained by an optical microscope with excitation at 430 nm. Since only the PL signal from Si nanocrystals (red to near-IR range) is collected by filtering the excitation light, the image clearly demonstrates that Si nanocrystals are homogeneously incorporated within the nanofibers network.

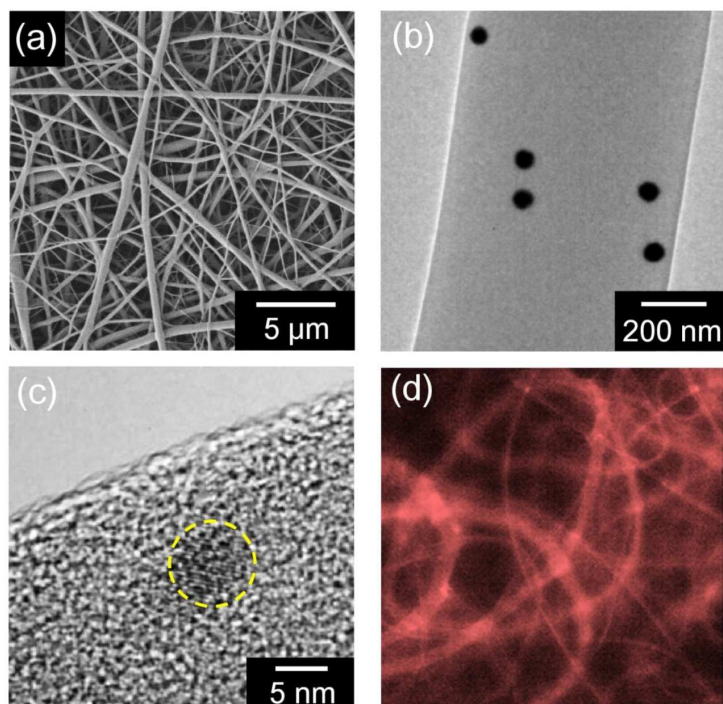


*Figure 6-2 (a) SEM image of electrospun HPC nanofibers doped with Si nanocrystals and Au nanoparticles. (b) TEM image of codoped nanofibers. (c) High-resolution TEM image showing a Si nanocrystal doped in a nanofiber. (d) Microscope PL image of codoped nanofibers (excited at 430 nm).*

To investigate the effect of codoping of Au nanoparticles on the light emission of Si nanocrystals, we performed PL excitation (PLE) spectroscopy for single- and codoped nanofiber samples using a tunable (340 nm–2200 nm) optical parametric oscillator (SpectraPhysics Inspire) pumped by a Ti:sapphire laser (MaiTai HP SpectraPhysics, 82MHz repetition rate) using an average power of 2.5 mW. The samples are directly irradiated by a focused excitation beam without waveguiding excitation.<sup>142</sup> In Figure

6-3 (a) and (b), we show the PL spectra of single- and codoped nanofibers excited at 490 and 545 nm, respectively. We measured the PL spectra at 5 different excitation spots, and calculated the average PL intensity and error bars. When excited at 490 nm, which is detuned from LSPR of Au nanoparticles, both the single- and codoped nanofibers samples show comparable PL intensity (within the error bars). Figure 6-3 (c) shows the measured PL decay traces of single- (black) and codoped (red) nanofiber detected at 720 nm using the excitation by the Ar laser beam (488 nm), which has been modulated with an acousto-optic modulator at a frequency of 1 kHz. The decay curves are well-fitted by a stretched exponential decay function,  $I = I_0 \exp(-t/\tau)^\beta$ , where  $\tau$  is the effective lifetime and  $\beta$  is the stretching parameter. The same  $\tau$  (32  $\mu$ sec) and  $\beta$  (0.74) are obtained for both samples, and almost identical to that of Si nanocrystals doped in a HPC film (*i. e.*,  $\tau$ =31  $\mu$ sec and  $\beta$ =0.77), which indicates that there is no significant change in the decay time of Si nanocrystals by electrospinning. Moreover, the comparison between single- and codoped nanofibers demonstrate that the spontaneous decay rate of Si nanocrystals is not affected by the codoping with Au nanoparticles, consistently with the large average distance between Si nanocrystals and Au nanoparticle (*i.e.*, precluding near-field interactions).

On the contrary, when we excite the systems at 545 nm, the PL intensity of the codoped nanofibers is enhanced by approximately a factor of 2 compared to the one of single-doped nanofibers. To better understand the origin of the measured PL enhancement, we study the PL enhancement spectrum (the PL intensity ratio of codoped to single-doped nanofibers). Figure 6-3 (d) shows the enhancement factors of the PL of Si nanocrystals and the scattering spectrum of Au nanoparticles- doped

nanofibers. We find that the PL enhancement factor strongly depends on the excitation wavelength and that its trend follows the scattering spectrum of Au nanoparticles in the nanofibers. The PL enhancement in a generic system of emitters (of identical density) can originate from several factors: the modifications of (a) excitation efficiency; (b) extraction efficiency of emitted light; (c) quantum efficiency (*i. e.*, emission rate) of the emitters. The separation between the extinction peak of Au nanoparticles (at 550 nm shown in Figure 6-1(d)) and the emission peak of Si nanocrystals (at 720 nm) allows us to exclude significant enhancement of the extraction efficiency at the emission wavelength. Moreover, due to the large average distance between Si nanocrystals and Au nanoparticles, we did not observe sizable modifications of the PL decay times of Si nanocrystals in both samples. Therefore, we can deduce that the measured PL enhancement originates from the plasmon-enhanced light scattering, which increases the effective excitation efficiency of Si nanocrystals due to the redistribution and trapping of light inside the Au nanoparticles doped nanofibers. The presence of strongly scattering Au nanoparticles in the nanofibers leads to an increase of the absorption rate of the pump inside the Si nanocrystals codoped samples. Our data demonstrate that the codoping of Au nanoparticles in active nanofibers significantly enhances the emission of Si nanocrystals in the absence of non-radiative quenching, which limits the performance of alternative active systems coupled to plasmonic nanoparticles in the near-field.<sup>151</sup>

In the inset of Figure 6-3 (d), we show the PL peak wavelength of single- and codoped nanofibers as a function of excitation wavelengths, demonstrating the red-shift with increasing excitation wavelength. This behavior is commonly observed in an ensemble

of Si nanocrystals.<sup>153,154</sup> Due to the size distribution of Si nanocrystals, only larger Si nanocrystals with smaller optical bandgap energies can be excited when the excitation wavelength is close to the PL wavelength.<sup>153,154</sup> In addition, we observe a small red-shift between single- and codoped samples across the overall excitation wavelength range. This can be explained by photon re-absorption in the presence of an inhomogeneous population of Si nanocrystals dispersed inside nanofibers (*i. e.*, the emission from small Si nanocrystals is re-absorbed by the larger Si nanocrystals). Since the scattering spectrum of Au nanoparticles overlaps with the shorter wavelength side of the PL spectrum, the emission from the smaller Si nanocrystals is strongly scattered by the Au nanoparticles and efficiently re-absorbed at lower energy by the larger Si nanocrystals in the nanofibers. This leads to the slight red-shift of the PL observed in the codoped samples.

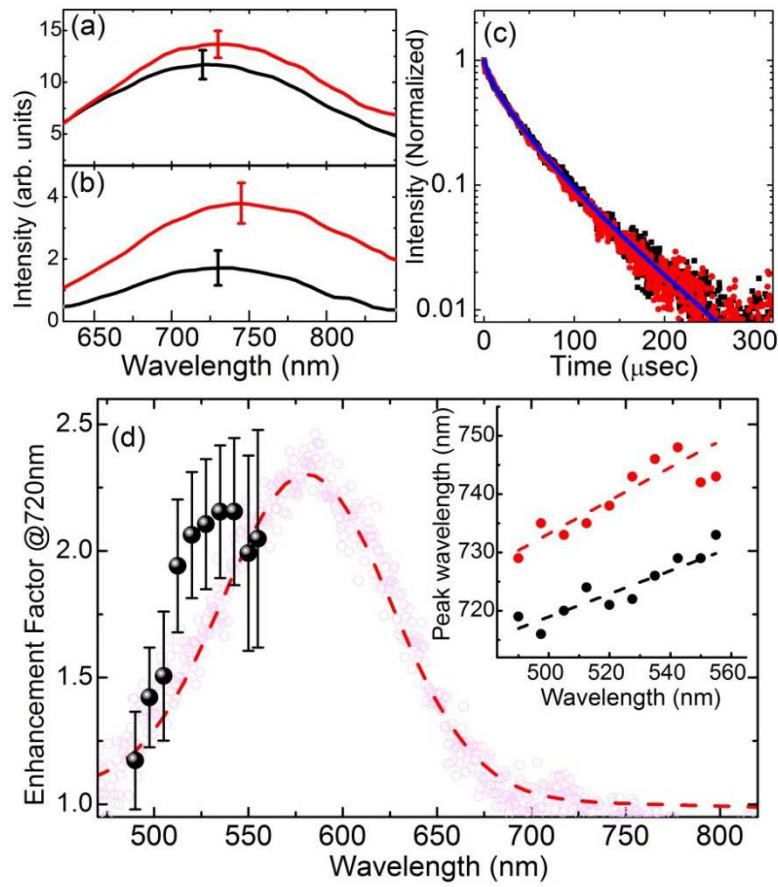


Figure 6-3. PL spectra of single- (black) and codoped (red) nanofibers excited at (a) 490 and (b) 545 nm. PL peak wavelength of single- (black) and codoped (red) nanofibers as a function of excitation wavelength. (c) PL decay curves of single- (black) and codoped (red) nanofibers detected at 720 nm with the fitting curve (blue). (d) PL enhancement factors (black) as a function of excitation wavelength. Red dashed curve shows the scattering spectrum of codoped nanofibers. Inset: PL peak wavelength of single- (black) and codoped (red) nanofibers excited at different wavelengths.

### 6-3 Conclusion

We developed active light-emitting HPC nanofibers doped with Si nanocrystals and Au nanoparticles. By performing time-resolved PL and PLE measurements, we demonstrate that codoped nanofibers give rise to enhanced PL by a factor of 2.2 in the absence of non-radiative quenching of the Si nanocrystal emission due to plasmon-enhanced scattering of pump radiation from Au nanoparticles to Si nanocrystals inside the nanofibers. Our findings provide not only a new concept for the plasmon-enhanced PL, but also a novel opportunity for biocompatible active platforms that leverage cost-effective and largely scalable processing with Si nanocrystals light emission for biophotonic applications.

## Chapter 7

# Size-Controlled Growth of Cubic Boron Phosphide Nanocrystals

Adapted from *H. Sugimoto, et al., RSC Advances, 5, 8427–8431 (2015).*

### 7-1 Introduction

As described in Figure 7-1, cubic boron phosphide (BP) is one of III-V compound semiconductors with the zinc-blende crystal structure. The indirect band gap is reported to be 2.0 eV. Analogously to other B-group V compound semiconductors such as boron nitride (BN) and boron arsenide (BAs), cubic BP has prominent mechanical, electronic, and thermoelectric properties.<sup>155–157</sup> Cubic BP has a covalent bonding due to its small ionicity,<sup>158</sup> resulting in high decomposition temperature (~1403 K) and chemical stability.<sup>156</sup> This makes it a promising candidate for high-temperature electronic devices. Since the discovery of cubic BP crystal in 1957,<sup>159</sup> cubic BP crystals have been grown by several methods including chemical vapor deposition (CVD),<sup>156,160,161</sup> close-spaced vapor transport (CVT),<sup>162</sup> flux growth,<sup>163,164</sup> and high-pressure flux method.<sup>165</sup> The band structure of cubic BP has been studied by photo- and electro-reflectance spectroscopy for films epitaxially grown on (100) Si



wafers.<sup>166</sup> The large thermoelectric figure of merit at high temperatures is shown for CVD grown BP films.<sup>167</sup>

In this Chapter, we develop a method to grow cubic BP nanocrystals smaller than 10 nm in diameter with a size-controllable manner. Semiconductor nanocrystals with the size in such range have been attracting significant attention for past several decades, because of the fascinating optical properties due to the quantum size effects. In particular, colloidal dispersion of semiconductor nanocrystals with several nanometers in diameter have been most extensively studied, because they can be a precursor for the formation of high-quality nanocrystal films for electronic devices by low-cost printable processes.<sup>1,168</sup> Growth of size-controlled BP nanocrystals provides the possibility to develop printable BP electronic devices. However, research on BP nanocrystals is very limited<sup>169–171</sup> mainly due to the lack of established growth processes. To our knowledge size-controlled growth of BP nanocrystals smaller than 10 nm has not been succeeded. In this paper, we report a new method to grow single-crystalline cubic BP nanocrystals with the diameter of 2 to 6 nm and relatively narrow size distributions. From the analyses by X-ray photoelectron and Raman spectroscopy, and transmission electron microscopy, the growth mechanism is discussed.

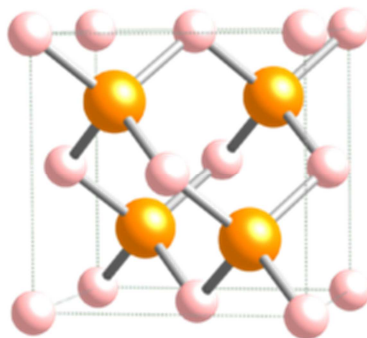


*Figure 7-1 Crystal structure of cubic phase boron phosphide. Boron atoms (pink balls) and phosphorus (yellow balls).  
([https://en.wikipedia.org/wiki/Boron\\_phosphide](https://en.wikipedia.org/wiki/Boron_phosphide))*

## 7-2 Materials and Methods

Scheme 1 shows the preparation procedure of cubic BP nanocrystals. Mixture films of Si, B, P and O were deposited on thin stainless steel plate by cosputtering Si chips ( $15 \times 13 \text{ mm}^2$ ) and boron phosphate ( $\text{BPO}_4$ ) tablets (10 mm in diameter) placed on a  $\text{SiO}_2$  target (10 cm in diameter). The number of Si chips was fixed to 4 pieces, while that of  $\text{BPO}_4$  tablets was changed from 4 to 12. The list of samples is shown in Table 7-1. The mixture films, *i.e.*, Si-rich borophosphosilicate glass (BPSG) films, were peeled from the stainless steel plates and annealed at  $1200^\circ\text{C}$  in a  $\text{N}_2$  gas atmosphere for 30 min. As will be shown later, BP nanocrystals are formed in silicate matrices during the annealing process. Annealed films were then ground in a mortar to obtain fine powder. The powder was dissolved in hydrofluoric acid solution (46 wt.%) to extract BP

nanocrystals from silicate matrices. Isolated nanocrystals were then transferred to methanol.

XPS measurements (PHI X-tool, ULVAC-PHI) were carried out using an Al K $\alpha$  X-ray source. Raman spectra were measured using a micro-Raman setup (LabRAM HR Evolution, HORIBA). The excitation source was a 325 nm line of a He-Cd laser with the excitation power of 0.5 mW. For the XPS and Raman measurements of free-standing BP nanocrystals, BP nanocrystal-dispersed in methanol was drop-casted on gold-coated Si wafers. The morphology and structure of BP nanocrystals were studied by TEM (JEM-2100F, JEOL). The diffuse reflectance spectra of free-standing BP nanocrystals were measured by a UV–VIS–NIR spectrophotometer (Solid Spec-3700, Shimadzu). Optical band gap was estimated from Tauc-plots of the spectra after the Kubelka–Munk transformation. Photoluminescence (PL) spectra were obtained by using a single spectrometer equipped with a liquid-N<sub>2</sub> cooled charge coupled device (CCD) (Roper Scientific). The excitation wavelength was a 325 nm line of a He-Cd laser. The spectral response of the detection system was corrected with the reference spectrum of a standard halogen lamp. Time transient of PL signals was obtained by a gated intensified CCD (ICCD) (PI-Max, Princeton Instrument) with the gate width of 5 nsec. The third harmonic of a Nd:YAG laser (355 nm, pulse width 5 ns, repetition frequency 20 Hz) was used as the excitation source.

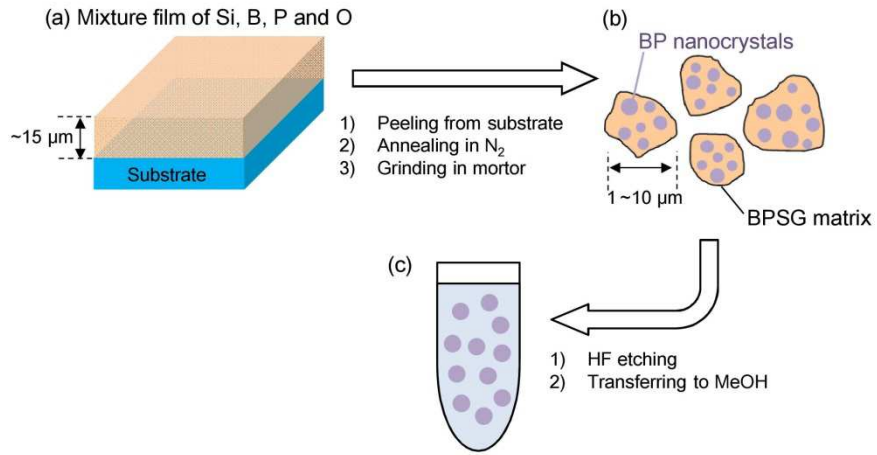


Figure 7-2 Schematic of the preparation of cubic BP nanocrystals.

**Table 7-1.** List of samples. The number of  $\text{BPO}_4$  tablets for the sputtering target, annealing temperature ( $T_a$ ), composition ratio of Si, B and P, average diameter ( $d_{\text{ave}}$ ) of BP nanocrystals.

Sample	Number of $\text{BPO}_4$ tablets	$T_a$ ( $^{\circ}\text{C}$ )	Si: B: P	$d_{\text{ave}}$ (nm)
BP4	4	1200	93.9: 3.5: 2.6	2.2
BP8	8	1200	87.3: 7.5: 5.2	4.3
BP12	12	1200	86.3: 7.9: 5.8	5.9

## 7-3 Results and Discussion

### A. BP nanocrystals in films.

Figure 7-3 (a)–(c) shows XPS spectra of BP12 before and after annealing. Before annealing, the Si 2p peak is at 103.4 eV. By annealing, it shifts to 103.8 eV. This binding energy corresponds to that of stoichiometric  $\text{SiO}_2$ .<sup>172</sup> Therefore, Si exists in as-deposited films as slightly oxygen-deficient silica and is fully oxidized by annealing, although annealing is performed in a  $\text{N}_2$  atmosphere. The B 1s spectrum in Figure 7-3 (b) has two peaks at 188 and 193 eV. These peaks can be assigned to non-oxidized B and fully-oxidized B ( $\text{B}_2\text{O}_3$ ), respectively. By annealing, the signal intensity of the non-oxidized B with respect to that of oxidized B increases. Similarly, in the P 2p spectra in Figure 7-3 (c), the signal from non-oxidized P at 130 eV with respect to that of fully-oxidized P ( $\text{P}_2\text{O}_5$ ) (133–135 eV) increases significantly by annealing. Very similar results are obtained for BP8. These XPS data indicate that Si is oxidized, while B and P are reduced by annealing Si-rich BPSG.

Figure 7-3(d) shows IR absorption spectra of films before and after annealing. The insets show the expansions around  $1400\text{ cm}^{-1}$  and  $900\text{ cm}^{-1}$ . The peaks at 480, 800 and  $1060\text{--}1080\text{ cm}^{-1}$  are due to Si–O–Si vibrations. By annealing, the Si–O–Si stretching mode at  $1060\text{ cm}^{-1}$  shifts to  $1080\text{ cm}^{-1}$  and the intensity increases. Furthermore, the intensity of B–O vibration mode at  $1400\text{ cm}^{-1}$  decreases and the P–O–P stretching mode at  $920\text{ cm}^{-1}$ <sup>173,174</sup> almost disappears. These results are consistent with the XPS data in Figure 7-3 (a)–(c), *i.e.*, Si is oxidized, while B and P are reduced by annealing.

Figure 7-3 (e) shows a Raman spectrum of BP12. The relatively sharp peak at 825  $\text{cm}^{-1}$  can be assigned to the LO phonon of cubic BP crystal ( $\sim 828 \text{ cm}^{-1}$  in ref. <sup>161,175</sup>). The broad band around 450  $\text{cm}^{-1}$  may arise from BPSG matrices. The peaks at 360 and 460  $\text{cm}^{-1}$  are tentatively assigned to B-P and P-P symmetric stretching modes.<sup>176</sup> The signal around 510  $\text{cm}^{-1}$  may be due to Si nanocrystals and nanoclusters remained unoxidized.<sup>177</sup>

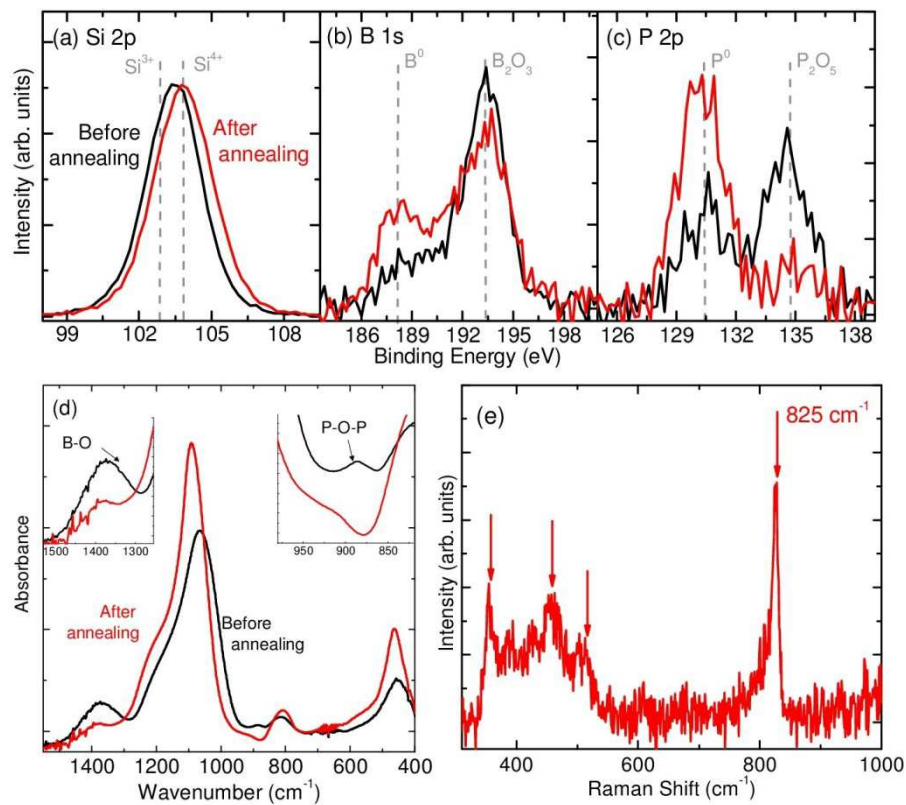


Figure 7-3 XPS spectra of film sample (BP12) before and after annealing. (a) Si 2p (b) B 1s (c) P 2p. (d) IR absorption spectra before and after annealing. (e) Raman spectrum after annealing.

Figure 7-4 shows the PL spectra of BP4, BP8 and BP12 after annealing. The broad PL bands can be decomposed into two Gaussian peaks centered at 1.4 (Peak 1) and 1.6 eV (Peak 2). The relative contribution of peak 2 increases with increasing B and P concentration, suggesting that peak 2 is related to BP. We will discuss the origin of peak 2 later. On the other hand, the opposite trend of peak 1 suggests that it arises from Si nanocrystals and nanoclusters remained unoxidized.<sup>178,179</sup>

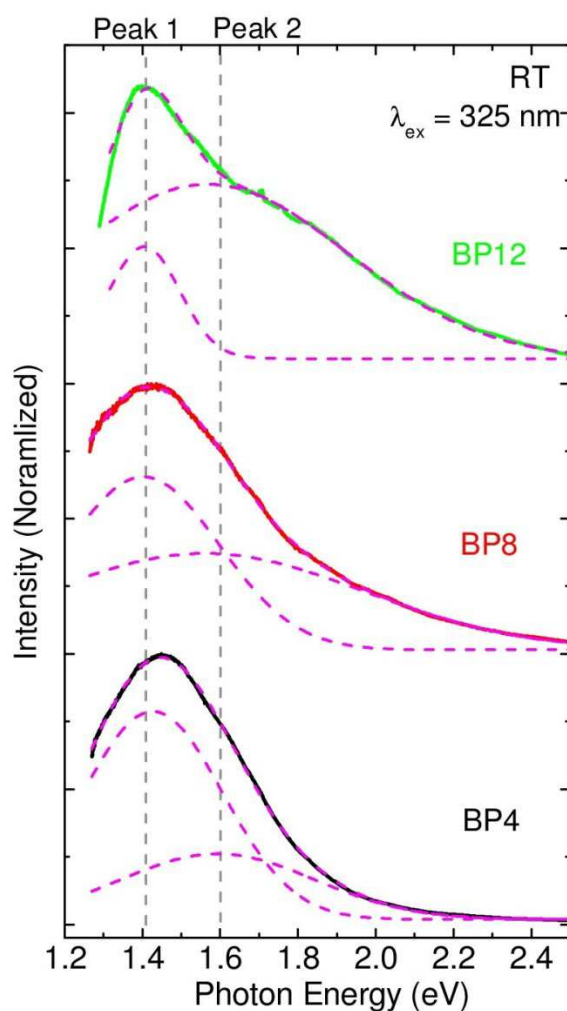


Figure 7-4 PL spectra of film samples with different B and P concentrations.

## B. Free-standing BP nanocrystals

Figure 7-5 (a)–(c) shows TEM images of particles after HF etching. The electron diffraction patterns are shown in the insets. The bars represent the data of cubic BP crystal (JCPDS No. 11-0119). The intensity profiles of the diffraction patterns are shown in Figure 7-5 (d). All peaks can be assigned to that of cubic BP, indicating that the nanoparticles in Figures 7-5 (a)–(c) are cubic BP crystal. The high-resolution TEM image in Figure 7-5 (e) demonstrates that the particle is single crystal. The lattice spacing estimated from the image is 0.26 nm (for the process of estimation, see Figure 7-6), corresponding to {111} planes of cubic BP crystal. We carefully observed more than 50 particles and found that all particles are single crystal of cubic BP. The size distributions obtained from TEM images are shown in Figure 7-5 (f). The average diameter in BP12 is 5.9 nm and that in BP8 is 4.3 nm. In BP4, the size is too small to be estimated by TEM observations. Hence, the size of nanocrystals in BP4 is estimated from the width of the electron diffraction peak by employing the Scherrer equation:

$$D = \frac{K\lambda}{\beta \cos \theta},$$

where,  $D$  is the diameter of nanocrystals,  $K$  is a constant determined by particle morphology,  $\beta$  is the full width at half-maximum (FWHM) of the diffraction peak, and  $\theta$  is the center position of the peak. Under the assumption that  $K$ ,  $\lambda$  and  $\theta$  are the same between BP4 and BP8, the ratio of the diameter ( $D_{\text{BP4}}/D_{\text{BP8}}$ ) is equal to that of the FWHM ( $\beta_{\text{BP4}}/\beta_{\text{BP8}}$ ) as,



$$\frac{D_{BP4}}{D_{BP8}} = \frac{\frac{K\lambda}{\beta_{BP4} \cos \theta}}{\frac{K\lambda}{\beta_{BP8} \cos \theta}} = \frac{\beta_{BP8}}{\beta_{BP4}}.$$

By using the diameter of BP8 obtained from TEM images (4.3 nm), the diameter of BP4 is estimated to be 2.2 nm.

In this paper, we fixed the annealing temperature at 1200°C. Growth of BP nanocrystals is possible at higher annealing temperatures, *e. g.*, 1250°C. However, we did not see notable difference of the size between 1200 and 1250°C in BP8. On the other hand, at 1100°C, we did not find BP nanocrystals after etching.

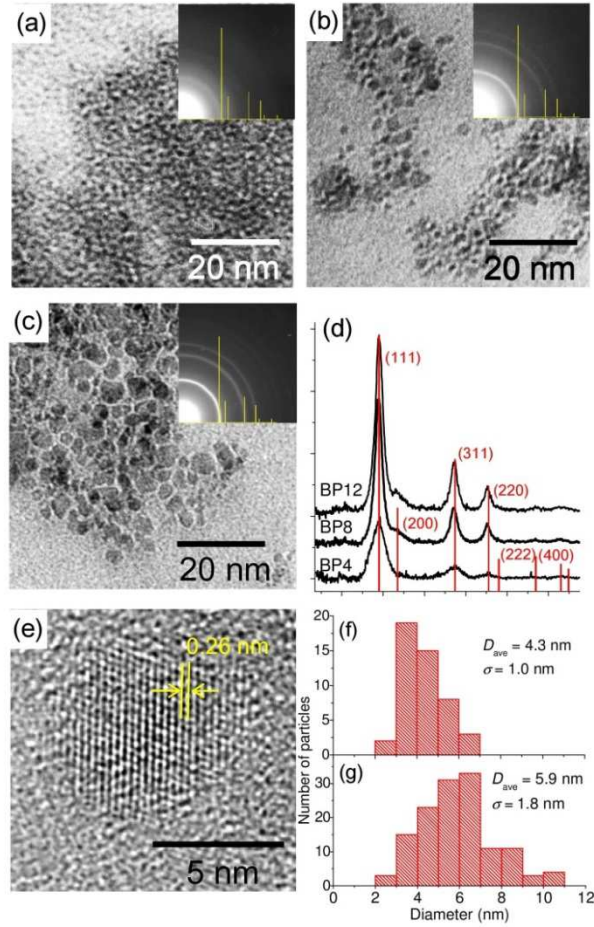


Figure 7-5. TEM images of (a) BP4, (b) BP8 and (c) BP12. (d) Intensity profiles of electron diffraction patterns. (e) High-resolution TEM image of a particle in BP8. Size distributions of (f) BP8 and (g) BP12.

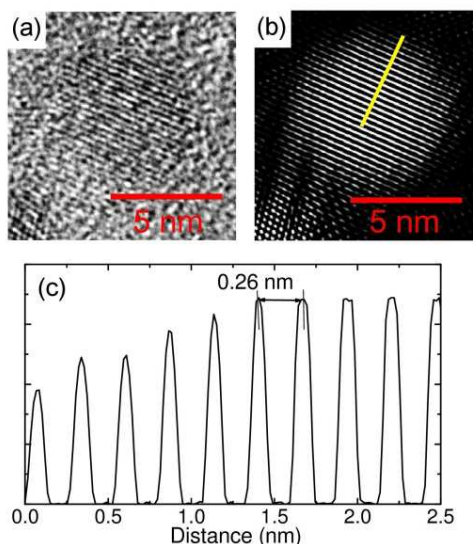


Figure 7-6 (a) High-resolution TEM image of a BP nanocrystal. (b) Inverse fast Fourier transform image after FFT and choosing spots corresponding (111) lattice fringes of BP crystals of (a). (c) Intensity profile of the yellow line of (b).

Figure 7-7 (a)–(c) shows the XPS spectra of cubic BP nanocrystals (BP12) after HF etching. The Si 2p signal almost disappears by etching. Furthermore, the signals from oxidized B and P are strongly suppressed and the spectra are dominated by those from non-oxidized B and P. This is consistent with the TEM results that only cubic BP nanocrystals are observed after etching. The B:P atomic ratio roughly estimated from integral intensities of XPS spectra is 53:47. In B 1s spectrum in Figure 7-7 (b), a shoulder due to sub-oxides can be seen. On the other hand, in P 2p spectrum in Figure

7-7 (c), the oxide signal is very weak. This suggests that the outmost surface of BP nanocrystals is mainly oxygen-terminated B. This may result in slightly B-rich composition. However, the result obtained by XPS is not accurate enough to discuss the composition and structure of BP nanocrystals in detail. More precise method should be employed for further discussion. Similar results are obtained in BP8.

Figure 7-7 (d) shows Raman spectra of BP8 and BP12 after HF etching. By etching, the spectra become very simple and only a LO phonon mode of cubic BP is clearly observed around  $825\text{ cm}^{-1}$ . The small bump around  $800\text{ cm}^{-1}$  is due to TO phonon of cubic BP. In the inset of Figure 7-7 (d), the Raman spectrum of BP12 is compared with that of bulk BP crystal.<sup>161</sup> The LO phonon peak of BP12 is broadened and shifts to the low-wavenumber side compared to that of BP crystal. These are considered to be due to phonon confinement effects, which are commonly observed in small semiconductor nanocrystals.<sup>180,181</sup> In fact, the signal of BP8 is broader than that of BP12 due to the smaller size.

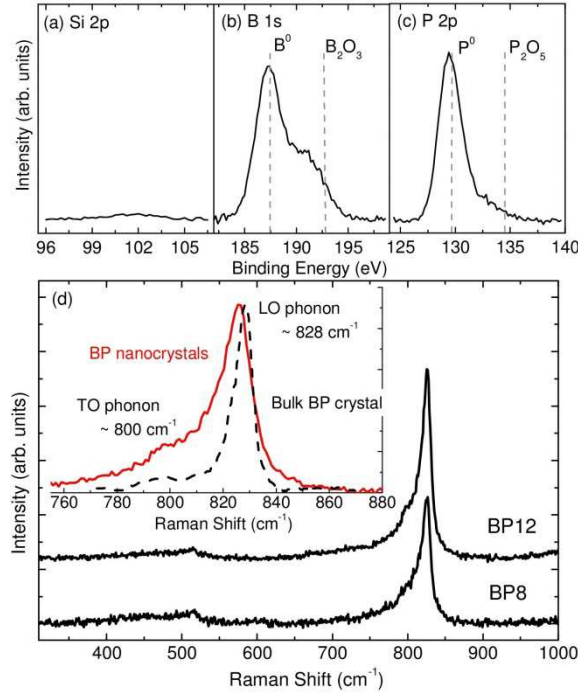


Figure 7-7 XPS spectra of BP nanocrystals (BP12). (a) Si 2p (b) B 1s (c) P 2p. (d) Raman spectra of BP8 and BP12. Inset: Comparison between Raman spectra of BP12 and bulk BP crystal.

Figure 7-8 (a) and (b) shows the Tauc plots,  $(\alpha h\nu)^n \propto (h\nu - E_{\text{opt}})$ , where  $\alpha$ ,  $h$  and  $\nu$  are an absorption coefficient, the Planck's constant and a photon frequency, respectively, of the absorption spectrum of BP12.  $n$  is set to 1/2 (Figure 7-8 (a)) and 2 (Figure 7-8 (b)) to obtain the indirect and direct band gaps, respectively. Although Tauc plot is not an accurate method to determine band gaps mainly due to the arbitrariness of fitting regions, especially when sub-band-gap tail states exist, it is convenient for the rough estimation. The estimated indirect and direct band gaps are 2.1 and 4.0 eV, respectively. Similarly, indirect and direct band gaps of 2.1 and 3.6 eV, respectively, are obtained for BP8. The indirect band gap is close to that reported in bulk BP crystal, *i.e.*, 2.0 eV.<sup>182</sup> On

the other hand, the direct band gaps are smaller than literature values, *i.e.*, 4.25–5.0 eV,<sup>166,183</sup> respectively. The difference might be related to the non-stoichiometric compositions and surface oxide layers.

Figure 7-8 (c) shows PL spectra of BP8 and BP12 after HF etching. Both samples exhibit broad PL around 1.6 eV. To our knowledge, this is the first observation of room temperature (RT) PL of BP nanocrystals. The peak is very broad covering the 1.3-2.0 eV range (FWHM ~650 meV) even at low temperature (6.7K). No significant difference can be seen between the spectra of BP8 and BP12. The PL peak energy coincides with that of peak 2 in Figure 7-8, suggesting that peak 2 arises from BP nanocrystals. The PL is relatively insensitive to the temperature and the intensity at RT is about 30 % of that at 6.7K.

The PL peak energy of 1.6 eV is about 500 meV lower than the optical band gap estimated in Figure 7-8 (a). This suggests that tail states probably originating from surface defects are responsible for the PL. The non-stoichiometric composition may also be related to the low energy PL. The size-insensitiveness of the spectral shape supports the model. In order to obtain the band edge luminescence, proper surface termination may be necessary. A PL decay curve of BP12 at RT is shown in Figure 7-8 (d). The PL lifetime estimated from the decay curve is 19.6 ns. No slower components are observed. This value is very short for the indirect band gap semiconductor, suggesting defect-mediated recombination of carriers.

Finally, we would like to mention the scalability of the synthesis process. In this paper, mixture films of Si, B, P and O are produced by sputtering. It is a relatively slow and

expensive process. However, sputtering is not an essential process for the growth of cubic BP nanocrystals. They can be produced irrespective of the preparation procedure of Si, B, P and O mixture materials, if the composition is within a proper range. For example, cubic BP nanocrystals can be produced by annealing mixture solutions of hydrogen silsesquioxane (HSQ),  $\text{H}_3\text{BO}_3$  and  $\text{H}_3\text{PO}_4$ , when  $\text{H}_3\text{BO}_3$  and  $\text{H}_3\text{PO}_4$  concentration is relatively high, *i.e.*, when the amounts of B and P are large enough to oxidize all excess Si. On the other hand, when their concentration is relatively small, excess Si remains even after reducing B and P. This results in the growth of B and P co-doped Si nanocrystals.<sup>184</sup> This method does not use any vacuum processes and thus can be easily scaled up for the mass production of cubic BP nanocrystals.

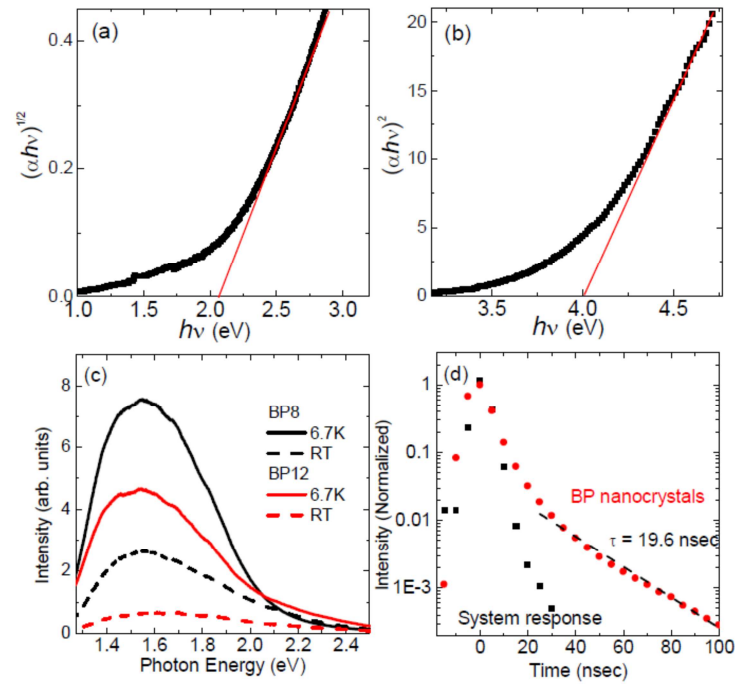


Figure 7-8. Tauc-plots of BP nanocrystals (BP12) for (a) indirect and (b) direct transitions. PL spectra of BP8 and BP12 at 6.7 K and RT. (d) PL decay curve of BP12 (red filled circle). Black squares are system response.

## 7-4 Conclusions

We have developed a new route for size-controlled growth of cubic BP nanocrystals. Thermal annealing of heavily B and P doped Si-rich silica films resulted in the formation BP nanocrystal in SiO<sub>2</sub> matrices due to the reduction of B and P by excess Si. Free-standing BP nanocrystals in solution were obtained by etching out the matrices. A comprehensive structural study revealed the formation of single crystalline BP nanocrystals with the diameter controlled from 2 to 6 nm. The optical band gap of BP nanocrystals was 2.1 eV and they showed a broad PL with the maximum around 1.6 eV at RT.

## Chapter 8

# Growth of Boron-Rich Nanocrystals from Oxygen-Deficient Borophosphosilicate Glasses for Boron Neutron Capture Therapy

Adapted from *H. Sugimoto, et al., RSC Advances, 5, 98248–98253 (2015).*

### 8-1 Introduction

Boron Neutron Capture Therapy (BNCT) is a radiotherapy treatment based on the ability of the stable isotope boron ( $^{10}\text{B}$ ) to capture neutron.<sup>185–188</sup> The neutron exposure of  $^{10}\text{B}$  generates  $^4\text{He}$  ( $\alpha$  particle) and  $^7\text{Li}$ , resulting in selective destruction of tumor cells without damaging adjacent cells because of their short pass length of approximately 10  $\mu\text{m}$  comparable to the diameter of cells.<sup>185–187</sup> Conditions of the materials for the BNCT are small size ( $<1\ \mu\text{m}$ ) for efficient incorporation into cells, high-solubility in water, as well as a large B content exceeding the required amount ( $\sim 10^9$  B atoms per cell). In previous work, boronophenylalanine (BPA) and sodium borocaptate (BSH) have been extensively used for BNCT in cancer treatment.<sup>189–191</sup> However, owing to their low-solubility and a small amount of B ( $\sim 5\ \text{wt.}\%$ ) per a molecule, focused research aiming at finding alternative materials is highly demanded.



Recently, there have been numerous efforts for the development of biocompatible inorganic nanoparticles with optimized functionalities for targeting biomedical applications such as drug delivery carriers<sup>192</sup> and fluorescent probes for sensing<sup>193</sup> and imaging.<sup>194</sup> Moreover, by the combination of different nanomaterials such as luminescent organic dyes or semiconductor nanocrystals, mesoporous silica nanoparticles for drug delivery and magnetic nanoparticles, the development of multifunctional nanoparticles have been reported.<sup>195,196</sup> This approach enables us to simultaneously perform imaging, diagnosis and therapy, which is also very promising for improved performance of BNCT. However, nanoparticles synthesized for the particular application in BNCT is still limited *e.g.*, borosilicate,<sup>197</sup> boron carbide<sup>198</sup> and boron phosphate,<sup>199</sup> and they do not satisfy all the required conditions.

In Chapter 2 and 7, we have developed heavily B and P codoped Si nanocrystals and boron phosphide (BP) nanocrystals by annealing quaternary amorphous films composed of B, O, Si, and P with different compositions prepared by sputtering (Figure 8-1).<sup>91,200</sup> A common feature of the starting material is that they are oxygen-deficient compared to BPSG ( $\text{SiO}_2\text{-}x\text{B}_2\text{O}_3\text{-}y\text{P}_2\text{O}_5$ ) due to addition of excess Si. When the atomic concentration ratio of B and P to excess Si is very small, typically less than 0.03, phase separation of the film by high temperature annealing results in the growth of B and P codoped Si nanocrystals in BPSG matrices.<sup>91,103</sup> By etching out BPSG matrices, free-standing B and P codoped Si nanocrystals are extracted in solution. The codoped Si nanocrystals are highly dispersible in polar solvents without organic ligands and exhibit efficient size-tunable luminescence in the biological transparent window (700–1300 nm) with excellent pH- and photostability.<sup>132</sup> These features make them promising in

biological imaging and diagnostic applications as well as in BNCT. On the other hand, at higher B and P concentrations, excess Si acts as a reducing agent and  $B_2O_3$  and  $P_2O_5$  are reduced to cubic phase BP nanocrystals (bottom part of Figure 8-1).<sup>200</sup> BP nanocrystals may be potentially suitable for BNCT because of the large B content per nanocrystal (~50 at.%). However, they are not dispersible in water and the luminescence, which originates from defect-related states, has limited wavelength tunability.

In Figure 8-1, in between the two extremes, there may be a chance to develop a new type of B-rich nanocrystals, which combine the advantages of B and P codoped Si nanocrystals and BP nanocrystals in BNCT applications. Therefore, in this work, we grow nanocrystals in the composition range in between the two extremes. We show that a new type of cubic nanocrystals with the lattice constant in between Si and BP crystal are grown in specific conditions. The average B concentration of the ternary B-Si-P cubic nanocrystals reaches 36 at.%. The nanocrystals are dispersible in water and the luminescence is located in the biological window.

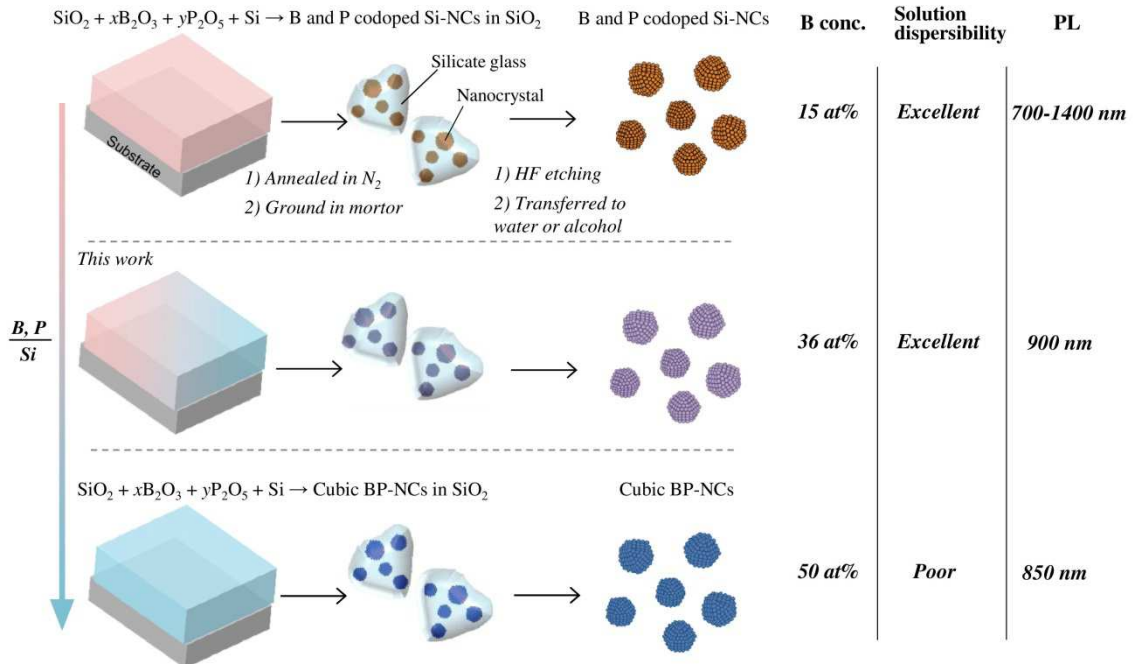


Figure 8-1. Preparation of different kinds of B-rich nanocrystals by phase separation of oxygen deficient (Si-rich) BPSG ( $\text{SiO}_2$ - $x\text{B}_2\text{O}_3$ - $y\text{P}_2\text{O}_5$ ) films.

## 8-2 Materials and Method

Preparation procedure of B-Si-P nanocrystals is qualitatively the same as those of B and P codoped Si nanocrystals<sup>91,103</sup> and cubic BP nanocrystals.<sup>200</sup> Amorphous films composed of B, O, Si and P were sputter-deposited on a thin stainless steel plate by cosputtering different sputtering targets (see Figure 8-2 and Table 8-1) in an RF-sputtering apparatus (SPF-210HS, Anelva) with the RF power of 200W. For the preparation of sample A, Si chips ( $15 \times 10 \text{ mm}^2$ ) and  $\text{B}_2\text{O}_3$  tablets (10 mm in diameter) were placed on a phosphosilicate glass (PSG) sputtering target (5 wt.%  $\text{P}_2\text{O}_5$  in  $\text{SiO}_2$ ,

10 cm in diameter). The composition of the target was exactly the same as that used in Refs. <sup>91</sup> and <sup>103</sup>, and in this preparation condition, B and P codoped Si nanocrystals are grown by annealing. For the preparation of samples B-E, Si chips, B<sub>2</sub>O<sub>3</sub> and BPO<sub>4</sub> tablets (10 mm in diameter) were placed on a SiO<sub>2</sub> target (10 cm in diameter).

The list of samples together with the compositions of the sputtering targets is shown in Table 8-1. To control the B and P concentrations in films, the numbers of B<sub>2</sub>O<sub>3</sub> and BPO<sub>4</sub> tablets were changed from 2 to 8, while that of Si chips was fixed to 4 (see Figure 8-2). Since B<sub>2</sub>O<sub>3</sub> and BPO<sub>4</sub> tablets are placed on a SiO<sub>2</sub> plate, the increase of the number of B<sub>2</sub>O<sub>3</sub> and BPO<sub>4</sub> tablets results in the decrease of the area of SiO<sub>2</sub>. Therefore, the B and P concentrations of deposited films are not proportional to the number of tablets. It should be stressed here that all the samples are oxygen-deficient compared to BPSG (SiO<sub>2-x</sub>B<sub>2</sub>O<sub>3-y</sub>P<sub>2</sub>O<sub>5</sub>). After sputtering, the films peeled from the stainless steel plates (80-100 mg) were annealed at 1100°C in a N<sub>2</sub> gas atmosphere for 30 min. By annealing, due to the oxygen deficiency, B, Si and P are precipitated and nanoparticles are formed in silicate matrices. Annealed films were then ground in a mortar to obtain fine powder. The powder of 20 mg was dissolved in hydrofluoric acid solution (46 wt.%) to extract B-Si-P nanocrystals from silicate matrices. Finally, isolated nanocrystals of approximately 1.5 mg were dispersed in methanol or water.

X-ray photoelectron spectroscopy (XPS) measurements (PHI X-tool, ULVAC-PHI) were carried out using an Al K $\alpha$  x-ray source. For the XPS and FTIR measurements of free-standing nanocrystals, colloidal dispersion of nanoparticles was drop-casted on gold-coated Si wafers. The morphology and structure of final products were studied by

TEM (JEM-2100F, JEOL). The details of measurements of PL spectra and PL-QYs were shown in Chapter 2.

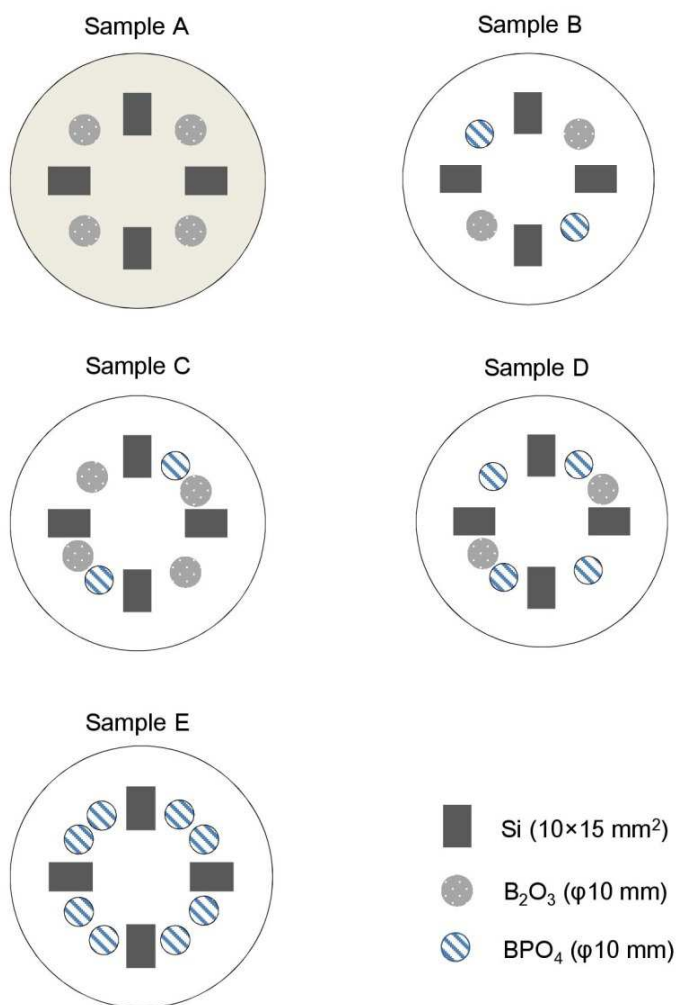


*Figure 8-2 Schematics of sputtering targets ( $\text{SiO}_2$ ) of sample A-E. In the case of sample A, the targets are placed on PSG target.*

*Table 8-1. Sample list with Si, B and P concentration ratios before and after HF etching.*

	sample A	sample B	sample C	sample D	sample E
Sputtering target (B <sub>2</sub> O <sub>3</sub> , BPO <sub>4</sub> )	(4, 0) on PSG	(2, 2) on SiO <sub>2</sub>	(4, 2) on SiO <sub>2</sub>	(2, 4) on SiO <sub>2</sub>	(0, 8) on SiO <sub>2</sub>
Si:B:P (precursor films)	97.9 : 2.3 : 0.8	97.2 : 1.9 : 0.9	91.7 : 3.8 : 4.5	87.8 : 8.0 : 4.2	87.3 : 7.5 : 5.2
Si:B:P (Free-standing particles)	84.1: 11.5 : 3.4	82.9 : 12.7 : 5.4	73.7 : 15.4 : 10.9	30.9 : 36.4 : 32.7	1.5 : 50.6 : 47.9

### 8-3 Results and Discussion

First, we study samples just after annealing *i. e.*, before extracting nanocrystals by HF etching. Figure 8-3(a)-(c) show XPS spectra of Si 2p, B 1s and P 2p core-levels, respectively. The Si 2p peak appears at 103–104 eV, in between the binding energies of Si<sup>3+</sup> and Si<sup>4+</sup>. The spectra are slightly asymmetric due to contributions of sub-oxides (Si<sup>1+</sup> to Si<sup>3+</sup>). The B 1s spectra in Figure 8-3(b) have two peaks at 188 and 193 eV. These are assigned to the neutral states of B (non-oxidized) and fully-oxidized B (B<sub>2</sub>O<sub>3</sub>), respectively. Similarly, in the P 2p spectra in Figure 8-3(c), both signals from non-oxidized and oxidized P at 130 and 134.5 eV, respectively, are observed. In Figure 8-3(b) and (c), we also find that the intensity ratio of non-oxidized and oxidized signals is different between samples. We estimate the Si: B: P atomic ratios from integral intensities of XPS spectra by taking into account the photo-ionization cross-sections of

each element. The results summarized in Table 8-1 demonstrate that the composition is controlled by changing the sputtering targets.

We then dissolve the silicate matrices by HF etching to liberate nanoparticles into solution. For samples A-D, we obtained clear yellowish dispersions in methanol and water. As will be shown later, nanoparticles are dispersed in the solutions without agglomeration. On the other hand, in sample E, a milky solution is obtained due to light scattering by agglomerates. Figure 8-3 (a)–(c) shows the XPS spectra of the nanoparticles (sample A–E) after HF etching. Atomic compositions of Si, B and P in samples A-E after HF etching estimated from XPS data are shown in Table 1. We can see that Si concentration decreases and B and P concentration increases from A to E. From our previous work,<sup>91,200</sup> sample A is B and P codoped Si nanocrystals and sample E is cubic BP nanocrystals. In Si 2p spectra in Figure 8-3 (a), we can see the signals in the range of 99.6 eV ( $\text{Si}^0$ ) to 103.4 eV ( $\text{Si}^{4+}$ ) including intermediate oxidation states. The spectra of samples A, B and C are qualitatively the same, *i. e.*, two signals from  $\text{Si}^0$  (99.5 eV) and  $\text{Si}^{4+}$  (103.4 eV) with a slightly different intensity ratio. These peaks arise from Si nanocrystal cores and thin native oxides on the surface (electron escape depth: 2–3 nm).<sup>97</sup> On the other hand, the binding energies of the peaks in sample D is different from those of samples B and C; the peaks are at 100.5 and 102.5 eV, corresponding to  $\text{Si}^{1+}$  and  $\text{Si}^{3+}$ , respectively. In the spectrum of sample E, only a very weak signal from Si is observed, because the formation of BP nanocrystals by the reduction of  $\text{B}_2\text{O}_3$  and  $\text{P}_2\text{O}_5$  is accompanied by the oxidation of Si during the annealing process and  $\text{SiO}_2$  is removed by HF etching. In B 1s spectra in Figure 8-3 (b), all samples exhibit a non-oxidized B signal at 187.5–189 eV, although the peak in sample D is slightly higher

than others. Similarly, in P 2p spectra, all samples show a signal around 130 eV, which corresponds to non-oxidized P. The binding energy of sample D is again slightly larger than others. Both B 1s and P 2p peaks have a tail toward higher energy due to their sub-oxides.

The results in Figure 8-3 suggest that samples B and C are within the same group of sample A, i.e., B and P codoped Si nanocrystals, although B and P concentration is larger. On the other hand, the structure of sample D is apparently different from that of sample A and E (BP nanocrystals). A possible explanation of the high energy shift of the Si 2p signal is the increased numbers of coordinated B and P to Si. In sample A, B and C, the average number of B and/or P atom bonded to a Si atom is considered to be less than one. On the other hand, almost comparable amounts of B, Si and P in sample D suggest that more than two B and/or P atoms can be coordinated to a Si atom. This results in the increase of the binding energy due to larger electron negativities of B (2.04) and P (2.2) than that of Si (1.9). In this situation, there should be substantial amounts of B-B and P-P bonds. The binding energy of B clusters is known to be larger than that of quadrivalent B in silicon.<sup>201</sup> Therefore, slight high energy shift of the B 1s peak can be explained by the increased number of B-B bonds in sample D. Similar explanation may be possible in P 2p, although we do not have XPS data of P clusters.



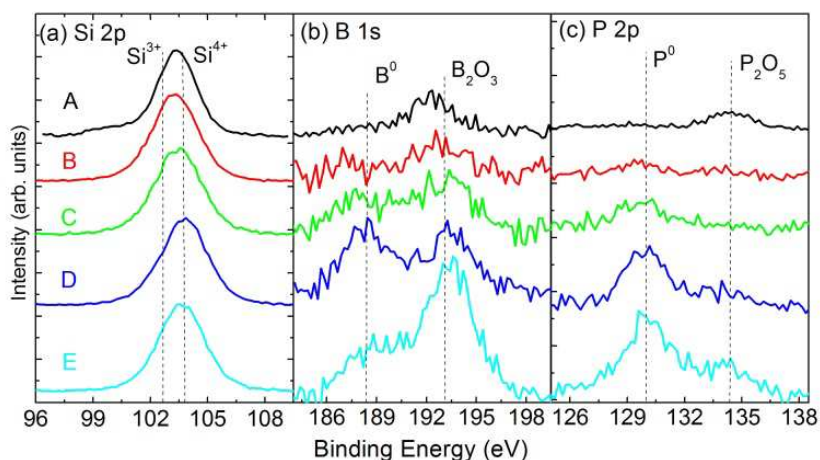
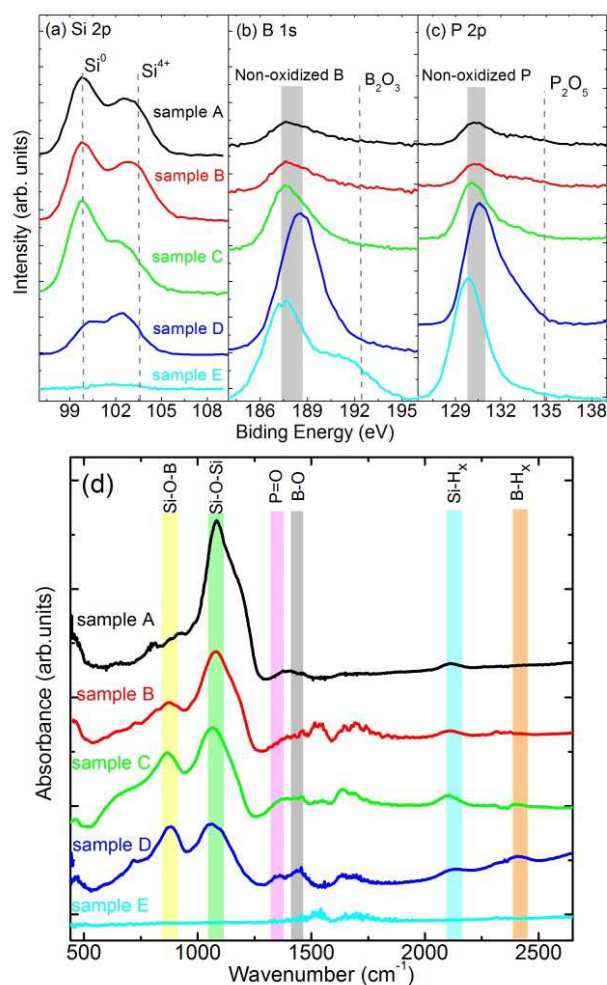


Figure 8-3. XPS spectra of samples A-E before HF etching. (a) Si 2p, (b) B 1s and (c) P 2p.

Figure 8-4 (d) shows IR absorption spectra of samples A-E. The amount of the samples is fixed and thus we can compare the intensity. In the spectrum of sample A, the peak around  $1060\text{--}1080\text{ cm}^{-1}$  is dominant, which is assigned to Si–O–Si stretching vibration modes. Note that all samples are stored for 2 days in methanol and then exposed in air during the measurements, and thus the surface of nanocrystals is slightly oxidized. The spectrum changes systematically from sample A to D. In sample B, an absorption appears at  $880\text{ cm}^{-1}$ , and it becomes stronger from B to D. Considering the high boron content, this peak can be assigned to a stretching mode of B–O–Si bridge often observed in  $\text{B}_2\text{O}_3/\text{SiO}_2$  glass systems.<sup>202,203</sup> In sample D, the signal intensity at  $880\text{ cm}^{-1}$  ( $\nu(\text{B–O–Si})$ ) is comparable to that at  $1080\text{ cm}^{-1}$  ( $\nu(\text{Si–O–Si})$ ). This suggests that the structure, especially the surface structure, of sample D is significantly different from that of sample A. The small peaks around  $1330\text{--}1450\text{ cm}^{-1}$  are assigned to B–O and P=O

stretching modes. The peaks at  $2100\text{ cm}^{-1}$  is due to  $\text{Si-H}_x$  vibrations.<sup>92</sup> The presence of  $\text{Si-H}$  and  $\text{Si-O}$  bonds on the surface is an important advantage for biomedical applications, because the surface can be functionalized by biological substances by using well-developed reactions.<sup>204,205</sup> This is an important feature for the efficient and selective cellular uptake in biological applications.<sup>206</sup> Only sample D has a peak at  $2410\text{ cm}^{-1}$ , which is assigned to the B-H stretching mode.<sup>207,208</sup> Observation of B-H modes also suggests that the surface structure of sample D is different from others. No detectable signal from sample E is observed, indicating that BP nanocrystals are highly resistant to oxidation.



*Figure 8-4. XPS spectra of sample A-E after HF etching. (a) Si 2p, (b) B 1s and (c) P 2p. (d) IR absorption spectra of sample A-E after HF etching.*

We perform a focused study on sample D from the comparison with sample A and sample E. Figure 8-5 (a) shows the optical transmittance spectrum of colloidal dispersion of sample D. The photo in the inset displays a yellowish clear dispersion. Nearly 100% transmittance around 1000 nm evidences the absence of light scattering by agglomerates. In Figure 8-5 (b), we show a high-resolution TEM image of sample D

drop-casted on a carbon-coated TEM grid. We can clearly see the lattice fringes, which confirm single-crystalline nature of the particles. The average diameter estimated from the images is 3.8 nm with the standard deviation of 0.6 nm (see the histogram in Figure 8-5 (c)). We analyzed the high-resolution TEM images very carefully and precisely measured the lattice spacing. Figure 8-5 (d)-(f) shows the typical images of nanocrystals in samples A, D and E. In Figure 8-5 (d) (sample A), the lattice fringe corresponds to the {111} plane of diamond structure Si (0.31 nm). The lattice fringes of nanocrystals in samples B and C can be also assigned to Si crystal (see Figure 8-6). The lattice spacing of the nanocrystal in Figure 8-5 (f) (sample E) is 0.26 nm, which corresponds to cubic BP crystal (0.26 nm).<sup>200</sup> On the other hand, in Figure 8-5 (e), we observed two kinds of lattice fringes; one has the spacing of 0.31 nm and the other 0.28 nm (see Figure 8-7, the distribution of lattice spacing). The former one can be assigned to Si crystal, while the latter one can be assigned neither to Si nor BP crystal. This can be confirmed in the electron diffraction patterns. Figure 8-5 (g) shows the intensity profile of an electron diffraction pattern of sample D obtained from hundreds of nanocrystals. The JCPDS data of diamond structure Si (JCPDS No. 27-1402) and cubic BP (JCPDS No. 11-0119) are shown below the figure by red and green bars. The peaks labeled by ● (red) are assigned to Si (JCPDS No. 27-1402), while others labeled by ▲ (blue) cannot be assigned neither to Si nor BP. Although we carefully investigated the compounds consisting of B, Si, P and O, no crystal structures attributable to the peaks labeled by ▲ exist.

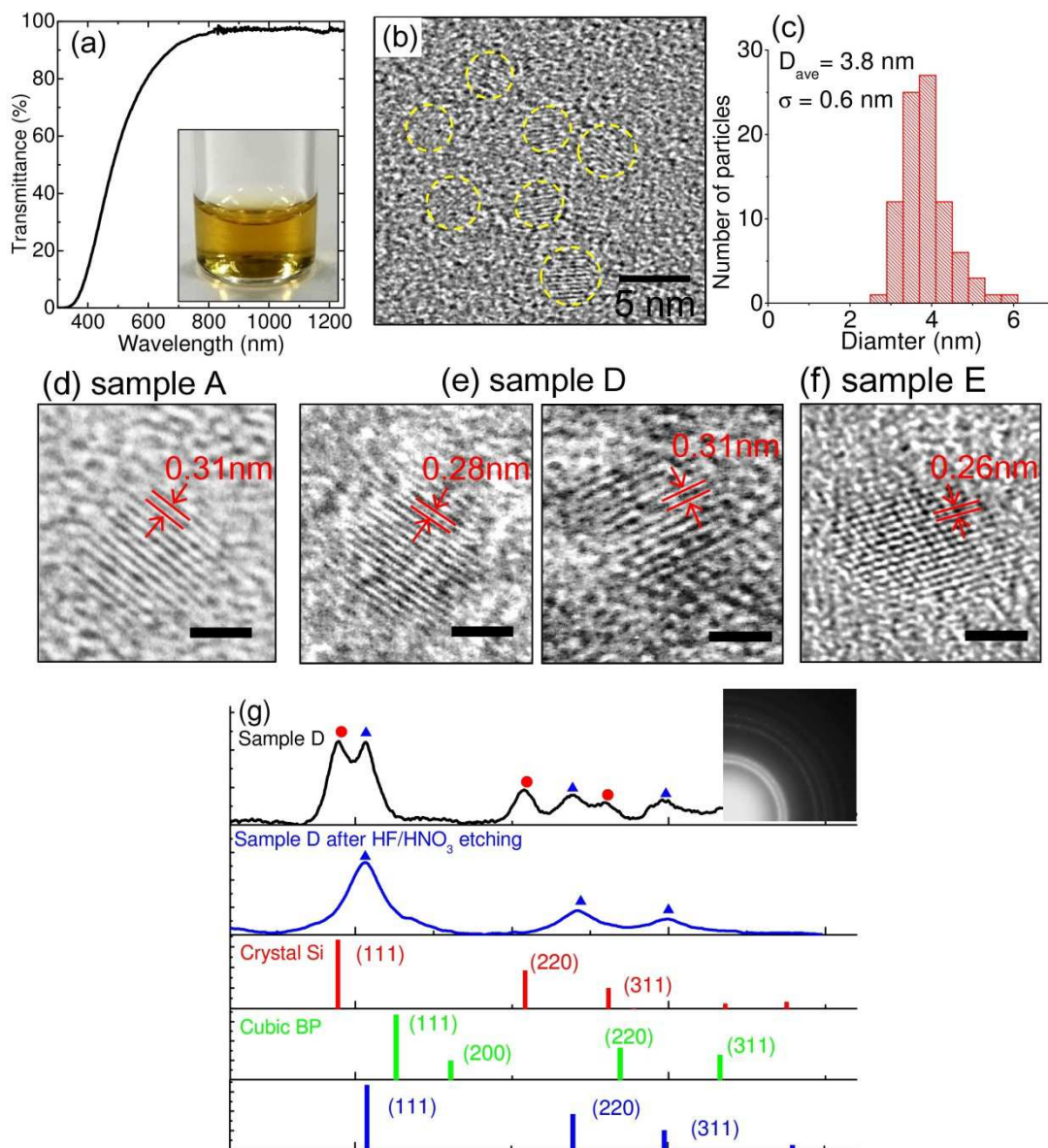


Figure 8-5 (a) Transmittance spectrum of sample D. Inset: Photograph of colloidal dispersion in water. (b) HRTEM image and (c) size distribution of sample D. (d)-(f) HRTEM images of nanocrystals in samples A, D and E. (g) Intensity profile of electron diffraction pattern of sample D (black) as-produced and (blue) after etching by the mixture solution of HF/HNO<sub>3</sub>. The bars represent diamond structure Si crystal (red) and cubic BP crystal (green). Blue bars show virtual crystal with 9% smaller lattice constant than Si crystal.

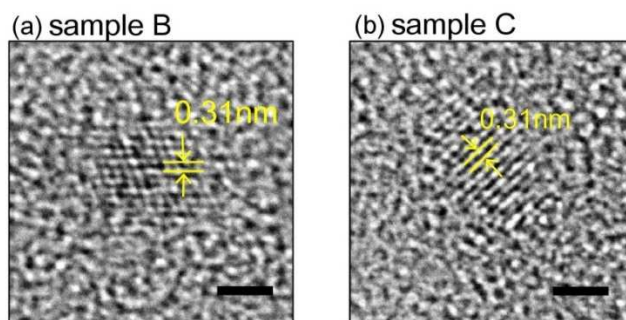


Figure 8-6 Typical HRTEM images of (a) sample B and (b) sample C. The scale bars are 2 nm.

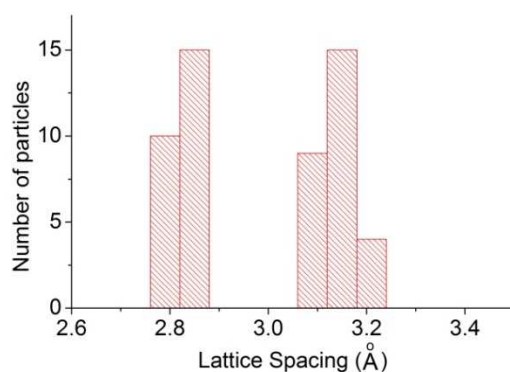


Figure 8-7 Distribution of lattice spacing of nanocrystals in sample D.

In order to extract nanocrystals exhibiting the electron diffraction pattern labeled by ▲, we etched out Si nanocrystals in sample D by the mixture solution of HF/HNO<sub>3</sub>. 10 μL of HF (46 wt.%) and HNO<sub>3</sub> (60 wt.%) solutions were added to 100 μL of sample D and the mixture was kept for 30 seconds. The electron diffraction pattern after the etching is shown in Figure 8-5 (g). Only the nanocrystals labeled by ▲ remains.

Therefore, these nanocrystals have high resistance to HF/HNO<sub>3</sub>, and are apparently different from B and P codoped Si nanocrystals.

The blue bars in Figure 8-5 (g) correspond to virtual crystal, whose lattice constant is 9% smaller than that of Si crystal. The peaks labeled by ▲ matches almost perfectly with the blue bars. This indicates that the unknown crystal most likely has zinc-blend type crystal structure. Considering the composition data obtained from XPS measurements, new crystal composed of almost the same amount of B, Si, P is formed. Unfortunately, within this work, the structure is not fully elucidated. Detailed studies including theoretical modeling of nanocrystals composed of B, Si and P are necessary to analyze the structure. It should be stressed here that lattice contraction of 9% by doping is not possible in Si crystal. In bulk Si crystal, at most 0.2% contraction of lattice is reported when B is doped very heavily (1.6 at.%).<sup>209</sup> No notable change of lattice constant is observed in B and P codoped Si nanocrystals (samples A–C).

In Figure 8-8, the PL spectra of samples A-D in solution excited at 450 nm are shown. All the samples exhibit a broad PL within a biological window. Despite the relatively small size distribution shown in Figure 8-8 (c), the PL is much broader than that of Si nanocrystals reported so far<sup>22,23</sup> and the full width at half maximum is in the range of 400 to 500 meV. The PL spectra depend slightly on B and P contents and have a tendency to shift to longer wavelength with increasing their contents. The PL quantum yield of sample D is 1.1 %, which is slightly smaller than others. The origin of the PL of B and P codoped Si nanocrystals is considered to be electron-hole recombination via

donor and acceptor states in the bandgap.<sup>103</sup> Since sample D consists of two different types of nanocrystals, it is not clear whether either or both of them contribute to the PL.

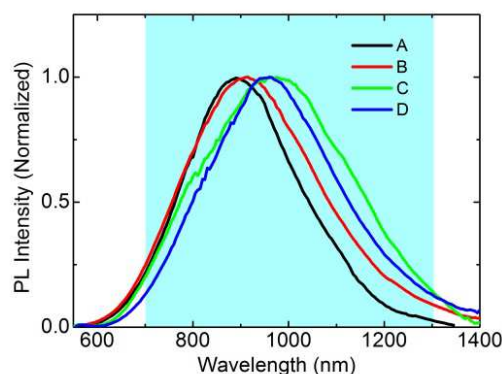


*Figure 8-8 PL spectra of samples A-D. Filled area shows the biological transparent window.*

## 8-4 Conclusion

In summary, formation of different types of B-rich nanocrystals by annealing O-deficient BPSG was systematically studied. In between the conditions of the growth of two known nanocrystals, *i.e.*, B and P codoped Si nanocrystals and cubic BP nanocrystals, we found a new type of B-rich nanocrystals containing more than 30 at.% of B. The nanocrystals were dispersible in water and exhibited broad PL centered at ~900 nm. The nanocrystals have Si-H and Si-O bonds on the surface, which can be functionalized by biomolecules with well-established processes. These properties



suggest that the B-rich nanocrystals developed in this work have a potential to be a multifunctional biomaterial used for imaging, diagnosis and BNCT.

## Chapter 9

### Outlook

Throughout this thesis, we have developed novel Si nanocrystal-based functional nanomaterials targeting for biological and optoelectronic applications. We have succeeded in producing all-inorganic colloidal Si nanocrystals with controlled size and PL energy by simultaneously doping B and P. From the detailed structural and PL properties, we have demonstrated the potential of B and P codoped Si nanocrystals for a variety of applications. However, there are many open questions remaining to be answered. Here we identify and highlight few ideas and some possible experiments that might clarify the problems.

- (a) We have studied the structural properties by TEM, STEM-EELS, IR-absorption, XPS and Raman spectroscopy, and suggested the structural model of heavily doped surface shell, which inorganically modifies the surface and provides the solution-dispersibility to Si nanocrystals. To further clarify the structure of codoped Si nanocrystals such as distribution of dopants in nm scale, atom probe tomography<sup>210</sup> would be a very powerful tool.
- (b) It has been also found that codoping modifies the energy state structure of Si nanocrystals, and enables them to exhibit widely size-tunable PL (0.85 to 1.85 eV) across the bulk Si bandgap. The PL energy of codoped Si nanocrystals is ~300 meV smaller than that of undoped nanocrystals with an identical size. The PL lifetimes

are much shorter than that of undoped Si nanocrystals. The samples in this work are ensemble and thus the distribution of size and doping concentration causes inhomogeneous broadening of the PL data. The technique of single-dot spectroscopy of individual nanocrystals<sup>211</sup>, in particular at low temperatures, could identify the origin of PL in codoped samples by excluding such inhomogeneous broadening.

- (c) In Chapter 4, we have studied the colloidal and photo-stability of codoped Si nanocrystals in a wide range of pH, which demonstrates the ultra-stable properties of the nanocrystals suitable for the bioimaging application. However, the quantum efficiency is limited up to 13% and excitation cross-section of Si nanocrystals is inherently low due to the indirect bandgap nature. As an answer to improve them, we developed the hybrid structures consisting of Si nanocrystals and plasmonic nanoparticles in Chapter 5 and 6. The plasmon-enhanced PL of Si nanocrystals dispersed in water-dispersible and biocompatible media demonstrated the promise of their use in bioimaging applications. To obtain further enhanced PL, the controlled system of Si nanocrystals coupled to the strongly-enhanced local fields by the gap-mode of coupled plasmonic structures<sup>128,212</sup> is desirable.
- (d) In Chapter 7, by expanding the preparation method of codoped Si nanocrystals, we have succeeded in producing cubic BP nanocrystals with different size. This is the first experimental demonstration of the formation of free-standing BP nanocrystals smaller than 10 nm. Furthermore, in chapter 8, we expanded the possibility of the application of Si-based nanocrystal materials in BNCT. Water-dispersible and

near-IR luminescent B-rich (36 at%) nanocrystals have been successfully prepared. Detailed structural analyses have demonstrated the formation of Si-B-P ternary alloy nanocrystals. There are still many questions and tasks to be achieved such as, i) the relation between size and quantum confinements of BP nanocrystals, ii) the development of colloidal BP nanocrystals in solution, iii) the structure and coordination of Si-B-P ternary alloy nanocrystals by theoretical calculations, and iv) the origin of PL of Si-B-P ternary alloy nanocrystals.

## References

- (1) Talapin, D. V.; Lee, J.-S.; Kovalenko, M. V.; Shevchenko, E. V. Prospects of Colloidal Nanocrystals for Electronic and Optoelectronic Applications. *Chem. Rev.* **2010**, *110*, 389–458.
- (2) Talapin, D. V.; Murray, C. B. PbSe Nanocrystal Solids for N- and P-Channel Thin Film Field-Effect Transistors. *Science* **2005**, *310*, 86–89.
- (3) Tang, J.; Kemp, K. W.; Hoogland, S.; Jeong, K. S.; Liu, H.; Levina, L.; Furukawa, M.; Wang, X.; Debnath, R.; Cha, D.; *et al.* Colloidal-Quantum-Dot Photovoltaics Using Atomic-Ligand Passivation. *Nat. Mater.* **2011**, *10*, 765–771.
- (4) Semonin, O. E.; Luther, J. M.; Choi, S.; Chen, H.-Y.; Gao, J.; Nozik, A. J.; Beard, M. C. Peak External Photocurrent Quantum Efficiency Exceeding 100% via MEG in a Quantum Dot Solar Cell. *Science* **2011**, *334*, 1530–1533.
- (5) Gur, I.; Fromer, N. A.; Geier, M. L.; Alivisatos, P. A. Air-Stable All-Inorganic Nanocrystal Solar Cells Processed from Solution. *Science* **2005**, *310*, 462–465.
- (6) Chung, D. S.; Lee, J.-S.; Huang, J.; Nag, A.; Ithurria, S.; Talapin, D. V. Low Voltage, Hysteresis Free, and High Mobility Transistors from All-Inorganic Colloidal Nanocrystals. *Nano Lett.* **2012**, *12*, 1813–1820.
- (7) Kwak, J.; Bae, W. K.; Lee, D.; Park, I.; Lim, J.; Park, M.; Cho, H.; Woo, H.; Yoon, D. Y.; Char, K.; *et al.* Bright and Efficient Full-Color Colloidal Quantum Dot Light-Emitting Diodes Using an Inverted Device Structure. *Nano Lett.* **2012**, *12*, 2362–2366.
- (8) Zhitomirsky, D.; Kramer, I. J.; Labelle, A. J.; Fischer, A.; Debnath, R.; Pan, J.; Bakr, O. M.; Sargent, E. H. Colloidal Quantum Dot Photovoltaics: The Effect of Polydispersity. *Nano Lett.* **2012**, *12*, 1007–1012.
- (9) Kagan, C.; Murray, C.; Bawendi, M. Long-Range Resonance Transfer of Electronic Excitations in Close-Packed CdSe Quantum-Dot Solids. *Phys. Rev. B* **1996**, *54*, 8633–8643.
- (10) Crooker, S. A.; Hollingsworth, J. A.; Tretiak, S.; Klimov, V. I. Spectrally Resolved Dynamics of Energy Transfer in Quantum-Dot Assemblies: Towards Engineered Energy Flows in Artificial Materials. *Phys. Rev. Lett.* **2002**, *89*, 186802.

- (11) Beard, M. C.; Knutsen, K. P.; Yu, P.; Luther, J. M.; Song, Q.; Metzger, W. K.; Ellingson, R. J.; Nozik, A. J. Multiple Exciton Generation in Colloidal Silicon Nanocrystals. *Nano Lett.* **2007**, *7*, 2506–2512.
- (12) Liu, Y.; Gibbs, M.; Puthussery, J.; Gaik, S.; Ihly, R.; Hillhouse, H. W.; Law, M. Dependence of Carrier Mobility on Nanocrystal Size and Ligand Length in PbSe Nanocrystal Solids. *Nano Lett.* **2010**, *10*, 1960–1969.
- (13) Liu, Y.; Gibbs, M.; Perkins, C. L.; Tolentino, J.; Zarghami, M. H.; Bustamante, J.; Law, M. Robust, Functional Nanocrystal Solids by Infilling with Atomic Layer Deposition. *Nano Lett.* **2011**, *11*, 5349–5355.
- (14) Oh, S. J.; Wang, Z.; Berry, N. E.; Choi, J.-H.; Zhao, T.; Gauding, E. A.; Paik, T.; Lai, Y.; Murray, C. B.; Kagan, C. R. Engineering Charge Injection and Charge Transport for High Performance PbSe Nanocrystal Thin Film Devices and Circuits. *Nano Lett.* **2014**, *14*, 6210–6216.
- (15) Nag, A.; Kovalenko, M. V.; Lee, J. S.; Liu, W.; Spokoyny, B.; Talapin, D. V. Metal-Free Inorganic Ligands for Colloidal Nanocrystals: S<sup>2-</sup>, HS<sup>-</sup>, Se<sup>2-</sup>, HSe<sup>-</sup>, Te<sup>2-</sup>, HTe<sup>-</sup>, TeS<sub>3</sub><sup>2-</sup>, OH<sup>-</sup>, and NH<sub>2</sub><sup>-</sup> as Surface Ligands. *J. Am. Chem. Soc.* **2011**, *133*, 10612–10620.
- (16) Lee, J.-S.; Kovalenko, M. V.; Huang, J.; Chung, D. S.; Talapin, D. V. Band-like Transport, High Electron Mobility and High Photoconductivity in All-Inorganic Nanocrystal Arrays. *Nat. Nanotechnol.* **2011**, *6*, 348–352.
- (17) Fafarman, A. T.; Koh, W. K.; Diroll, B. T.; Kim, D. K.; Ko, D. K.; Oh, S. J.; Ye, X.; Doan-Nguyen, V.; Crump, M. R.; Reifsnyder, D. C.; *et al.* Thiocyanate-Capped Nanocrystal Colloids: Vibrational Reporter of Surface Chemistry and Solution-Based Route to Enhanced Coupling in Nanocrystal Solids. *J. Am. Chem. Soc.* **2011**, *133*, 15753–15761.
- (18) Canham, L. T. Silicon Quantum Wire Array Fabrication by Electrochemical and Chemical Dissolution of Wafers. *Appl. Phys. Lett.* **1990**, *57*, 1046.
- (19) Takeoka, S.; Fujii, M.; Hayashi, S. Size-Dependent Photoluminescence from Surface-Oxidized Si Nanocrystals in a Weak Confinement Regime. *Phys. Rev. B - Condens. Matter Mater. Phys.* **2000**, *62*, 16820–16825.
- (20) Kovalev, D.; Heckler, H.; Polisski, G.; Koch, F. Optical Properties of Si Nanocrystals. *Phys. Status Solidi* **1999**, *215*, 871–932.

- (21) Valenta, J.; Juhasz, R.; Linnros, J. Photoluminescence from Single Silicon Quantum Dots at Room Temperature. *J. Lumin.* **2002**, *98*, 15–22.
- (22) Hannah, D. C.; Yang, J.; Podsiadlo, P.; Chan, M. K. Y.; Demortière, A.; Gosztola, D. J.; Prakapenka, V. B.; Schatz, G. C.; Kortshagen, U.; Schaller, R. D. On the Origin of Photoluminescence in Silicon Nanocrystals: Pressure-Dependent Structural and Optical Studies. *Nano Lett.* **2012**, *12*, 4200–4205.
- (23) Hessel, C. M.; Reid, D.; Panthani, M. G.; Rasch, M. R.; Goodfellow, B. W.; Wei, J.; Fujii, H.; Akhavan, V.; Korgel, B. A. Synthesis of Ligand-Stabilized Silicon Nanocrystals with Size-Dependent Photoluminescence Spanning Visible to Near-Infrared Wavelengths. *Chem. Mater.* **2012**, *24*, 393–401.
- (24) Mastronardi, M. L.; Maier-Flaig, F.; Faulkner, D.; Henderson, E. J.; Kübel, C.; Lemmer, U.; Ozin, G. A. Size-Dependent Absolute Quantum Yields for Size-Separated Colloidally-Stable Silicon Nanocrystals. *Nano Lett.* **2012**, *12*, 337–342.
- (25) Mangolini, L.; Kortshagen, U. Plasma-Assisted Synthesis of Silicon Nanocrystal Inks. *Adv. Mater.* **2007**, *19*, 2513–2519.
- (26) Mocatta, D.; Cohen, G.; Schattner, J.; Millo, O.; Rabani, E.; Banin, U. Heavily Doped Semiconductor Nanocrystal Quantum Dots. *Science* **2011**, *332*, 77–81.
- (27) Mimura, A.; Fujii, M.; Hayashi, S.; Yamamoto, K. Photoluminescence from Si Nanocrystals Dispersed in Phosphosilicate Glass Thin Films. *J. Lumin.* **2000**, *87-89*, 429–431.
- (28) Mimura, A.; Fujii, M.; Hayashi, S.; Kovalev, D.; Koch, F. Photoluminescence and Free-Electron Absorption in Heavily Phosphorus-Doped Si Nanocrystals. *Phys. Rev. B* **2000**, *62*, 12625–12627.
- (29) Pi, X. D.; Gresback, R.; Liptak, R. W.; Campbell, S. A.; Kortshagen, U. Doping Efficiency, Dopant Location, and Oxidation of Si Nanocrystals. *Appl. Phys. Lett.* **2008**, *92*, 123102.
- (30) Fujii, M.; Mimura, A.; Hayashi, S.; Yamamoto, Y.; Murakami, K. Hyperfine Structure of the Electron Spin Resonance of Phosphorus-Doped Si Nanocrystals. *Phys. Rev. Lett.* **2002**, *89*, 206805.
- (31) Stegner, A. R.; Pereira, R. N.; Lechner, R.; Klein, K.; Wiggers, H.; Stutzmann, M.; Brandt, M. S. Doping Efficiency in Freestanding Silicon Nanocrystals from the

- Gas Phase: Phosphorus Incorporation and Defect-Induced Compensation. *Phys. Rev. B* **2009**, *80*, 165326.
- (32) Pereira, R. N.; Almeida, A. J.; Stegner, A. R.; Brandt, M. S.; Wiggers, H. Exchange-Coupled Donor Dimers in Nanocrystal Quantum Dots. *Phys. Rev. Lett.* **2012**, *108*, 126806.
  - (33) Kanzawa, Y.; Fujii, M.; Hayashi, S.; Yamamoto, K. Doping of B Atoms into Si Nanocrystals Prepared by Rf Cosputtering. *Solid State Commun.* **1996**, *100*, 227–230.
  - (34) Sato, K.; Fukata, N.; Hirakuri, K. Doping and Characterization of Boron Atoms in Nanocrystalline Silicon Particles. *Appl. Phys. Lett.* **2009**, *94*, 25–27.
  - (35) Zhou, S.; Pi, X.; Ni, Z.; Luan, Q.; Jiang, Y.; Jin, C.; Nozaki, T.; Yang, D. Boron- and Phosphorus-Hyperdoped Silicon Nanocrystals. *Part. Part. Syst. Charact.* **2015**, *32*, 213–221.
  - (36) Gnaser, H.; Gutsch, S.; Wahl, M.; Schiller, R.; Kopnarski, M.; Hiller, D.; Zacharias, M. Phosphorus Doping of Si Nanocrystals Embedded in Silicon Oxynitride Determined by Atom Probe Tomography. *J. Appl. Phys.* **2014**, *115*, 034304.
  - (37) Pereira, R. N.; Stegner, A. R.; Andlauer, T.; Klein, K.; Wiggers, H.; Brandt, M. S.; Stutzmann, M. Dielectric Screening versus Quantum Confinement of Phosphorus Donors in Silicon Nanocrystals Investigated by Magnetic Resonance. *Phys. Rev. B* **2009**, *79*, -.
  - (38) Gresback, R.; Kramer, N. J.; Ding, Y.; Chen, T.; Kortshagen, U. R.; Nozaki, T. Controlled Doping of Silicon Nanocrystals Investigated by Solution-Processed Field Effect Transistors. *ACS Nano* **2014**, *8*, 5650–5656.
  - (39) Zhou, S.; Pi, X.; Ni, Z.; Ding, Y.; Jiang, Y.; Jin, C.; Delerue, C.; Yang, D.; Nozaki, T. Comparative Study on the Localized Surface Plasmon Resonance of Boron- and Phosphorus-Doped Silicon Nanocrystals. *ACS Nano* **2015**, *9*, 378–386.
  - (40) Rowe, D. J.; Jeong, J. S.; Mkhoyan, K. A.; Kortshagen, U. R. Phosphorus-Doped Silicon Nanocrystals Exhibiting Mid-Infrared Localized Surface Plasmon Resonance - Supplementary Information. *Nano Lett.* **2013**, Supplementary Information.
  - (41) Fujii, M.; Toshikiyo, K.; Takase, Y.; Yamaguchi, Y.; Hayashi, S. Below



- Bulk-Band-Gap Photoluminescence at Room Temperature from Heavily P- and B-Doped Si Nanocrystals. *J. Appl. Phys.* **2003**, *94*, 1990–1995.
- (42) Fujii, M.; Yamaguchi, Y.; Takase, Y.; Ninomiya, K.; Hayashi, S. Control of Photoluminescence Properties of Si Nanocrystals by Simultaneously Doping N- and P-Type Impurities. *Appl. Phys. Lett.* **2004**, *85*, 1158.
- (43) Fujii, M.; Yamaguchi, Y.; Takase, Y.; Ninomiya, K.; Hayashi, S. Photoluminescence from Impurity Codoped and Compensated Si Nanocrystals. *Appl. Phys. Lett.* **2005**, *87*, 211919.
- (44) Fukuda, M.; Fujii, M.; Sugimoto, H.; Imakita, K.; Hayashi, S. Surfactant-Free Solution-Dispersible Si Nanocrystals Surface Modification by Impurity Control. *Opt. Lett.* **2011**, *36*, 4026–4028.
- (45) Iori, F.; Degoli, E.; Magri, R.; Marri, I.; Cantele, G.; Ninno, D.; Trani, F.; Pulci, O.; Ossicini, S. Engineering Silicon Nanocrystals: Theoretical Study of the Effect of Codoping with Boron and Phosphorus. *Phys. Rev. B - Condens. Matter Mater. Phys.* **2007**, *76*, 1–14.
- (46) Cantele, G.; Degoli, E.; Luppi, E.; Magri, R.; Ninno, D.; Iadonisi, G.; Ossicini, S. First-Principles Study of N- and P-Doped Silicon Nanoclusters. *Phys. Rev. B* **2005**, *72*, 113303.
- (47) Pompa, P. P.; Martiradonna, L.; Torre, a Della; Sala, F. Della; Manna, L.; De Vittorio, M.; Calabi, F.; Cingolani, R.; Rinaldi, R. Metal-Enhanced Fluorescence of Colloidal Nanocrystals with Nanoscale Control. *Nat. Nanotechnol.* **2006**, *1*, 126–130.
- (48) Lakowicz, J. R. Plasmonics in Biology and Plasmon-Controlled Fluorescence. *Plasmonics* **2006**, *1*, 5–33.
- (49) Kinkhabwala, A.; Yu, Z.; Fan, S.; Avlasevich, Y.; Müllen, K.; Moerner, W. E. Large Single-Molecule Fluorescence Enhancements Produced by a Bowtie Nanoantenna. *Nat. Photonics* **2009**, *3*, 654–657.
- (50) Jin, Y.; Gao, X. Plasmonic Fluorescent Quantum Dots. *Nat. Nanotechnol.* **2009**, *4*, 571–576.
- (51) Ayala-Orozco, C.; Liu, J. G.; Knight, M. W.; Wang, Y.; Day, J. K.; Nordlander, P.; Halas, N. J. Fluorescence Enhancement of Molecules inside a Gold Nanomatrix. *Nano Lett.* **2014**, *14*, 2926–2933.

- (52) Yao, J.; Yang, M.; Duan, Y. Chemistry, Biology, and Medicine of Fluorescent Nanomaterials and Related Systems: New Insights into Biosensing, Bioimaging, Genomics, Diagnostics, and Therapy. *Chem. Rev.* **2014**, *114*, 6130–6178.
- (53) Cohen-Hoshen, E.; Bryant, G. W.; Pinkas, I.; Sperling, J.; Bar-Joseph, I. Exciton-Plasmon Interactions in Quantum Dot-Gold Nanoparticle Structures. *Nano Lett.* **2012**, *12*, 4260–4264.
- (54) Nepal, D.; Drummy, L. F.; Biswas, S.; Park, K.; Vaia, R. a. Large Scale Solution Assembly of Quantum Dot-Gold Nanorod Architectures with Plasmon Enhanced Fluorescence. *ACS Nano* **2013**, *7*, 9064–9074.
- (55) Focsan, M.; Gabudean, A. M.; Vulpoi, A.; Astilean, S. Controlling the Luminescence of Carboxyl-Functionalized CdSe/ZnS Core–Shell Quantum Dots in Solution by Binding with Gold Nanorods. *J. Phys. Chem. C* **2014**, *118*, 25190–25199.
- (56) Biteen, J. S.; Pacifici, D.; Lewis, N. S.; Atwater, H. a. Enhanced Radiative Emission Rate and Quantum Efficiency in Coupled Silicon Nanocrystal-Nanostructured Gold Emitters. *Nano Lett.* **2005**, *5*, 1768–1773.
- (57) Takeda, E.; Fujii, M.; Nakamura, T.; Mochizuki, Y.; Hayashi, S. Enhancement of Photoluminescence from Excitons in Silicon Nanocrystals via Coupling to Surface Plasmon Polaritons. *J. Appl. Phys.* **2007**, *102*.
- (58) Mertens, H.; Biteen, J. S.; Atwater, H. A.; Polman, A. Polarization-Selective Plasmon-Enhanced Silicon Quantum-Dot Luminescence. *Nano Lett.* **2006**, *6*, 2622–2625.
- (59) Walters, R. J.; Van Loon, R. V. a; Brunets, I.; Schmitz, J.; Polman, A. A Silicon-Based Electrical Source for Surface Plasmon Polaritons. *IEEE Int. Conf. Gr. IV Photonics GFP* **2009**, *9*, 74–76.
- (60) Goffard, J.; Gérard, D.; Miska, P.; Baudrion, A.-L.; Deturche, R.; Plain, J. Plasmonic Engineering of Spontaneous Emission from Silicon Nanocrystals. *Sci. Rep.* **2013**, *3*, 2672.
- (61) Erogbogbo, F.; Yong, K.; Roy, I.; Xu, G.; Prasad, P. N.; Swihart, M. T. Biocompatible Luminescent Silicon. *ACS Nano* **2008**, *2*, 873–878.
- (62) Pi, X.; Zhang, L.; Yang, D. Enhancing the Efficiency of Multicrystalline Silicon Solar Cells by the Inkjet Printing of Silicon-Quantum-Dot Ink. *J. Phys. Chem. C*

- 2012**, *116*, 21240–21243.
- (63) Pi, X.; Yu, T.; Yang, D. Water-Dispersible Silicon-Quantum-Dot-Containing Micelles Self-Assembled from an Amphiphilic Polymer. *Part. Part. Syst. Charact.* **2014**, *31*, 751–756.
  - (64) Clark, R. J.; Dang, M. K. M.; Veinot, J. G. C. Exploration of Organic Acid Chain Length on Water-Soluble Silicon Quantum Dot Surfaces. *Langmuir* **2010**, *26*, 15657–15664.
  - (65) Lakowicz, J. R. *Principles of Fluorescence Spectroscopy*; 2006.
  - (66) Tenney, A. S. Nondestructive Determination of the Composition and Thickness of Thin Films of Pyrolytically Deposited Borosilicate Glass by Infrared Absorption. *J. Electrochem. Soc.* **1971**, *118*, 1658.
  - (67) Sze, S. M.; Ng, K. K. Frontmatter. In *Physics of Semiconductor Devices*; John Wiley & Sons, Inc.: Hoboken, NJ, USA, 2006; pp. i – x.
  - (68) Hayashi, S.; Yamamoto, K. Optical Properties of Si-Rich SiO<sub>2</sub> Films in Relation with Embedded Si Mesoscopic Particles. *J. Lumin.* **1996**, *70*, 352.
  - (69) Nesbit, L. A. Annealing Characteristics of Si-Rich SiO<sub>2</sub> Films. *Appl. Phys. Lett.* **1985**, *46*, 38–40.
  - (70) Lu, Z. H.; McCaffrey, J. P.; Brar, B.; Wilk, G. D.; Wallace, R. M.; Feldman, L. C.; Tay, S. P. SiO<sub>2</sub> Film Thickness Metrology by X-Ray Photoelectron Spectroscopy. *Appl. Phys. Lett.* **1997**, *71*, 2764–2766.
  - (71) Hessel, C. M.; Wei, J.; Reid, D.; Fujii, H.; Downer, M. C.; Korgel, B. A. Raman Spectroscopy of Oxide-Embedded and Ligand-Stabilized Silicon Nanocrystals. *J. Phys. Chem. Lett.* **2012**, *3*, 1089–1093.
  - (72) M. Chandrasekhar, H. R. Chandrasekhar, M. Grimsditch, M. C. Study of the Localized Vibrations of Boron in Heavily Doped Si. *Phys. Rev. B* **1980**, *22*, 4825–4833.
  - (73) Newman, R. C.; Smith, R. S. Local Mode Absorption from Boron Arsenic and Boron Phosphorus Pairs in Silicon. *Solid State Commun.* **1967**, *5*, 723–726.
  - (74) Tsvetov, V. LOCALIZED VIBRATIONAL MODES IN SILICON: B-P PAIR BANDS. *Appl. Phys. Lett.* **1967**, *10*, 326.
  - (75) De k, P.; Gali, A.; S lyom, A. S.; Ordej n, P.; Kamar s, K.; Battistig, G. Studies of Boron–interstitial Clusters in Si. *J. Phys. Condens. Matter* **2003**, *15*, 4967–4977.

- (76) Adey, J.; Goss, J.; Jones, R.; Briddon, P. Identification of Boron Clusters and Boron-Interstitial Clusters in Silicon. *Phys. Rev. B* **2003**, *67*, 1–5.
- (77) Barker, A. S.; J., S. A. Optical Studies of the Vibrational Solids Properties of Disordered. *Rev. Mod. Phys.* **1975**, *47*, S1–S179.
- (78) Guerra, R.; Ossicini, S.; Emilia, R.; Morselli, P. Preferential Positioning of Dopants and Co-Dopants in Embedded. *J. Am. Chem. Soc.* **2014**, *136*, 4404–4409.
- (79) Peelaers, H.; Partoens, B.; Peeters, F. M. Formation and Segregation Energies of B and P Doped and BP Codoped Silicon Nanowires. *Nano Lett.* **2006**, *6*, 2781–2784.
- (80) Schoeters, B.; Leenaerts, O.; Pourtois, G.; Partoens, B. Ab-Initio Study of the Segregation and Electronic Properties of Neutral and Charged B and P Dopants in Si and Si/SiO<sub>2</sub> Nanowires. *J. Appl. Phys.* **2015**, *118*, 104306.
- (81) Arai, E.; Nakamura, H.; Terunuma, Y. Interface Reactions of {B}-{O}-{S}<sub>i</sub> System and Boron Diffusion into Silicon. *J. Electrochem. Soc.* **1973**, *120*, 980–987.
- (82) Jurbergs, D.; Rogojina, E.; Mangolini, L.; Kortshagen, U. Silicon Nanocrystals with Ensemble Quantum Yields Exceeding 60%. *Appl. Phys. Lett.* **2006**, *88*, 233116.
- (83) Wagner, J. Photoluminescence and Excitation Spectroscopy in Heavily Doped N- and P-Type Silicon. *Phys. Rev. B* **1984**, *29*, 2002–2009.
- (84) Wagner, J.; Del Alamo, J. a. Band-Gap Narrowing in Heavily Doped Silicon: A Comparison of Optical and Electrical Data. *J. Appl. Phys.* **1988**, *63*, 425–429.
- (85) Chan, T.-L.; Tiago, M. L.; Kaxiras, E.; Chelikowsky, J. R. Size Limits on Doping Phosphorus into Silicon Nanocrystals. *Nano Lett.* **2008**, *8*, 596–600.
- (86) Diarra, M.; Niquet, Y.-M.; Delerue, C.; Allan, G. Ionization Energy of Donor and Acceptor Impurities in Semiconductor Nanowires: Importance of Dielectric Confinement. *Phys. Rev. B* **2007**, *75*, 045301.
- (87) Iori, F.; Degoli, E.; Palummo, M.; Ossicini, S. Novel Optoelectronic Properties of Simultaneously N- and P-Doped Silicon Nanostructures. *Superlattices Microstruct.* **2008**, *44*, 337–347.
- (88) Delerue, C.; Lannoo, M.; Allan, G.; Martin, E.; Mihalcescu, I.; Vial, J. C.; Romestain, R.; Muller, F.; Bsiesy, A. Auger and Coulomb Charging Effects in Semiconductor Nanocrystallites. *Phys. Rev. Lett.* **1995**, *75*, 2228–2231.

- (89) Semonin, O. E.; Johnson, J. C.; Luther, J. M.; Midgett, A. G.; Nozik, A. J.; Beard, M. C. Absolute Photoluminescence Quantum Yields of IR-26 Dye, PbS, and PbSe Quantum Dots. *J. Phys. Chem. Lett.* **2010**, *1*, 2445–2450.
- (90) Hessel, C. M.; Henderson, E. J.; Veinot, J. G. C.; Uni, V.; February, R. V.; Re, V.; Recei, M.; August, V. Hydrogen Silsesquioxane : A Molecular Precursor for Nanocrystalline Si - SiO<sub>2</sub> Composites and Freestanding Hydride-Surface-Terminated Silicon Nanoparticles. *Chem. Mater.* **2006**, 6139–6146.
- (91) Sugimoto, H.; Fujii, M.; Imakita, K.; Hayashi, S.; Akamatsu, K. All-Inorganic Near-Infrared Luminescent Colloidal Silicon Nanocrystals: High Dispersibility in Polar Liquid by Phosphorus and Boron Codoping. *J. Phys. Chem. C* **2012**, *116*, 17969–17974.
- (92) Lucovsky, G. Structural Interpretation of the Vibrational Spectra of a-Si:H Alloys. *Phys. Rev. B* **1979**, *19*, 2064–2073.
- (93) Tsu, D. V., G. Lucovsky, B. N. D. Effects of the Nearest Neighbors and the Alloy Matrix on. *Phys. Rev. B* **1989**, *40*, 1795–1805.
- (94) Pi, X.; Mangolini, L.; Campbell, S.; Kortshagen, U. Room-Temperature Atmospheric Oxidation of Si Nanocrystals after HF Etching. *Phys. Rev. B* **2007**, *75*, 085423.
- (95) Canaria, C. A.; Lees, I. N.; Wun, A. W.; Miskelly, G. M.; Sailor, M. J. Characterization of the Carbon–silicon Stretch in Methylated Porous Silicon—observation of an Anomalous Isotope Shift in the FTIR Spectrum. *Inorg. Chem. Commun.* **2002**, *5*, 560–564.
- (96) Durrani, S. M. A.; Al-Kuhaili, M. F.; Khawaja, E. E. Characterization of Thin Films of a-SiO<sub>x</sub> (1.1 < x < 2.0) Prepared by Reactive Evaporation of SiO<sub>2</sub>. *J. Phys. Condens. Matter* **2003**, *15*, 8123–8135.
- (97) Lu, Z. H.; McCaffrey, J. P.; Brar, B.; Wilk, G. D.; Wallace, R. M.; Feldman, L. C.; Tay, S. P. SiO<sub>2</sub> Film Thickness Metrology by X-Ray Photoelectron Spectroscopy. *Appl. Phys. Lett.* **1997**, *71*, 2764.
- (98) Fujii, M.; Sugimoto, H.; Hasegawa, M.; Imakita, K. Silicon Nanocrystals with High Boron and Phosphorus Concentration Hydrophilic shell—Raman Scattering and X-Ray Photoelectron Spectroscopic Studies. *J. Appl. Phys.* **2014**, *115*, 084301.

- (99) Newman, R. C.; Smith, R. S. PHOSPHORUS PAIRS IN SILICON. *Solid State Commun.* **1967**, *5*, 723–726.
- (100) Deak, P.; Gali, A.; Solyom, A.; Ordejon, P.; Kamaras, K.; Battistig, G. Studies of Boron–interstitial Clusters in Si. *J. Phys. Condens. Matter* **2003**, *15*, 4967–4977.
- (101) Arai, E.; Nakamura, H.; Terunuma, Y. No Title. *J. Electrochem. Soc.* **1973**, *120*, 980–987.
- (102) Kessler, M. A.; Ohrdes, T.; Wolpensinger, B.; Harder, N.-P. Charge Carrier Lifetime Degradation in Cz Silicon through the Formation of a Boron-Rich Layer during BBr<sub>3</sub> Diffusion Processes. *Semicond. Sci. Technol.* **2010**, *25*, 055001.
- (103) Sugimoto, H.; Fujii, M.; Imakita, K.; Hayashi, S.; Akamatsu, K. Codoping N- and P-Type Impurities in Colloidal Silicon Nanocrystals: Controlling Luminescence Energy from below Bulk Band Gap to Visible Range. *J. Phys. Chem. C* **2013**, *117*, 11850–11857.
- (104) Fukuda, M.; Fujii, M.; Hayashi, S. Room-Temperature below Bulk-Si Band Gap Photoluminescence from P and B Co-Doped and Compensated Si Nanocrystals with Narrow Size Distributions. *J. Lumin.* **2011**, *131*, 1066–1069.
- (105) van Driel, A.; Nikolaev, I.; Vergeer, P.; Lodahl, P.; Vanmaekelbergh, D.; Vos, W. Statistical Analysis of Time-Resolved Emission from Ensembles of Semiconductor Quantum Dots: Interpretation of Exponential Decay Models. *Phys. Rev. B* **2007**, *75*, 035329.
- (106) Medintz, I. L.; Uyeda, H. T.; Goldman, E. R.; Mattoussi, H. Quantum Dot Bioconjugates for Imaging, Labelling and Sensing. *Nat. Mater.* **2005**, *4*, 435–446.
- (107) Li, Z. F.; Ruckenstein, E. Water-Soluble Poly(acrylic Acid) Grafted Luminescent Silicon Nanoparticles and Their Use as Fluorescent Biological Staining Labels. *Nano Lett.* **2004**, *4*, 1463–1467.
- (108) He, Y.; Zhong, Y.; Peng, F.; Wei, X.; Su, Y.; Lu, Y.; Su, S.; Gu, W.; Liao, L.; Lee, S. One-Pot Microwave Synthesis of Water-Dispersible, Ultraphoto- and pH-Stable, and Highly Fluorescent Silicon Quantum Dots. *J. Am. Chem. Soc.* **2011**, *133*, 14192–14195.
- (109) Lin, S. W.; Chen, D. H. Synthesis of Water-Soluble Blue Photoluminescent Silicon Nanocrystals with Oxide Surface Passivation. *Small* **2009**, *5*, 72–76.
- (110) Erogbogbo, F.; Yong, K.; Roy, I.; Xu, G.; Prasad, P. N.; Swihart, M. T.

- Biocompatible Luminescent Silicon Quantum Dots for Imaging of Cancer Cells. *ACS Nano* **2008**, *2*, 873–878.
- (111) Albright, P. S.; Gosting, L. J. Dielectric Constants of the Methanol-Water System from 5 to 55° 1. *J. Am. Chem. Soc.* **1946**, *68*, 1061–1063.
- (112) He, Y.; Lu, H. T.; Sai, L. M.; Su, Y. Y.; Hu, M.; Fan, C. H.; Huang, W.; Wang, L. H. Microwave Synthesis of Water-Dispersed CdTe/CdS/ZnS Core-Shell-Shell Quantum Dots with Excellent Photostability and Biocompatibility. *Adv. Mater.* **2008**, *20*, 3416–3421.
- (113) Gaponik, N.; Talapin, D. V.; Rogach, A. L.; Hoppe, K.; Shevchenko, E. V.; Kornowski, A.; Eychmüller, A.; Weller, H. Thiol-Capping of CdTe Nanocrystals: An Alternative to Organometallic Synthetic Routes. *J. Phys. Chem. B* **2002**, *106*, 7177–7185.
- (114) Lindsey, C. P.; Patterson, G. D. Detailed Comparison of the Williams–Watts and Cole–Davidson Functions. *J. Chem. Phys.* **1980**, *73*, 3348.
- (115) Miller, J. B.; Van Sickle, A. R.; Anthony, R. J.; Kroll, D. M.; Kortshagen, U. R.; Hobbie, E. K. Ensemble Brightening and Enhanced Quantum Yield in Size-Purified Silicon Nanocrystals. *ACS Nano* **2012**, *6*, 7389–7396.
- (116) Jin, S.; Demarco, E.; Pellin, M. J.; Farha, O. K.; Wiederrecht, G. P.; Hupp, J. T. Distance-Engineered Plasmon-Enhanced Light Harvesting in CdSe Quantum Dots. *J. Phys. Chem. Lett.* **2013**, *4*, 3527–3533.
- (117) Abadeer, N. S.; Brennan, M. R.; Wilson, W. L.; Murphy, C. J. Distance and Plasmon Wavelength Dependent Fluorescence of Molecules Bound to Silica-Coated Gold Nanorods. *ACS Nano* **2014**, 8392–8406.
- (118) Schubert, O.; Becker, J.; Carbone, L.; Khalavka, Y.; Provalska, T.; Zins, I.; Sönnichsen, C. Mapping the Polarization Pattern of Plasmon Modes Reveals Nanoparticle Symmetry. *Nano Lett.* **2008**, *8*, 2345–2350.
- (119) Ming, T.; Zhao, L.; Chen, H.; Woo, K. C.; Wang, J.; Lin, H. Experimental Evidence of Plasmaphores: Plasmon-Directed Polarized Emission from Gold Nanorod–Fluorophore Hybrid Nanostructures. *Nano Lett.* **2011**, *11*, 2296–2303.
- (120) Peng, X.; Manna, L.; Yang, W.; Wickham, J.; Scher, E.; Kadavanich, a; Alivisatos, A. Shape Control of CdSe Nanocrystals. *Nature* **2000**, *404*, 59–61.
- (121) Hu, J.; Li, L.; Yang, W.; Manna, L.; Wang, L.; Alivisatos, a P. Linearly Polarized

- Emission from Colloidal Semiconductor Quantum Rods. *Science* **2001**, 292, 2060–2063.
- (122) Walters, R. J.; Kalkman, J.; Polman, a.; Atwater, H. a.; De Dood, M. J. a. Photoluminescence Quantum Efficiency of Dense Silicon Nanocrystal Ensembles in Si O<sub>2</sub>. *Phys. Rev. B - Condens. Matter Mater. Phys.* **2006**, 73, 2–5.
- (123) Hohenester, U.; Trügler, A. MNPBEM - A Matlab Toolbox for the Simulation of Plasmonic Nanoparticles. *Comput. Phys. Commun.* **2012**, 183, 370–381.
- (124) Johnson Christy, R. W., P. B. Optical Constants of the Noble Metals. *Physical Review B*, 1972, 6, 4370–4379.
- (125) Novotny, L.; van Hulst, N. Antennas for Light. *Nat. Photonics* **2011**, 5, 83–90.
- (126) Busson, M. P.; Rolly, B.; Stout, B.; Bonod, N.; Bidault, S. Accelerated Single Photon Emission from Dye Molecule-Driven Nanoantennas Assembled on DNA. *Nat. Commun.* **2012**, 3, 962.
- (127) Purcell, E. M. Spontaneous Emission Probabilities at Radio Frequencies. *Phys. Rev.* **1946**, 69, 674–674.
- (128) Akselrod, G. M.; Argyropoulos, C.; Hoang, T. B.; Ciracì, C.; Fang, C.; Huang, J.; Smith, D. R.; Mikkelsen, M. H. Probing the Mechanisms of Large Purcell Enhancement in Plasmonic Nanoantennas. *Nat. Photonics* **2014**, 8, 1–15.
- (129) Lu, D.; Kan, J. J.; Fullerton, E. E.; Liu, Z. Enhancing Spontaneous Emission Rates of Molecules Using Nanopatterned Multilayer Hyperbolic Metamaterials. *Nat. Nanotechnol.* **2014**, 9, 48–53.
- (130) Govorov, A. O.; Bryant, G. W.; Zhang, W.; Skeini, T.; Lee, J.; Kotov, N. a; Slocik, J. M.; Naik, R. R. Exciton Plasmon Interaction and Hybrid Excitons in Semiconductor Metal Nanoparticle Assemblies. *Nano Lett.* **2006**, 6, 984–994.
- (131) Bharadwaj, P.; Novotny, L.; Bharadwaj, P.; Novotny, L. Spectral Dependence of Single Molecule Fluorescence Enhancement. *Opt. Express* **2007**, 15, 14266.
- (132) Sugimoto, H.; Fujii, M.; Fukuda, Y.; Imakita, K.; Akamatsu, K. All-Inorganic Water-Dispersible Silicon Quantum Dots: Highly Efficient near-Infrared Luminescence in a Wide pH Range. *Nanoscale* **2014**, 6, 122–126.
- (133) Caswell, K. K.; Wilson, J. N.; Bunz, U. H. F.; Murphy, C. J. Preferential End-to-End Assembly of Gold Nanorods by Biotin- Streptavidin Connectors. *J. Am. Chem. Soc.* **2003**, 125, 13914–13915.



- (134) Fu, Y.; Zhang, J.; Lakowicz, J. R. Plasmon-Enhanced Fluorescence from Single Fluorophores End-Linked to Gold Nanorods. *J. Am. Chem. Soc.* **2010**, *132*, 5540–5541.
- (135) Chang, J.-Y.; Wu, H.; Chen, H.; Ling, Y.-C.; Tan, W. Oriented Assembly of Au Nanorods Using Biorecognition System. *Chem. Commun. (Camb)*. **2005**, 1092–1094.
- (136) Wang, P.; Wang, Y.; Tong, L. Functionalized Polymer Nanofibers: A Versatile Platform for Manipulating Light at the Nanoscale. *Light Sci. Appl.* **2013**, *2*, e102.
- (137) Di Benedetto, F.; Camposeo, A.; Pagliara, S.; Mele, E.; Persano, L.; Stabile, R.; Cingolani, R.; Pisignano, D. Patterning of Light-Emitting Conjugated Polymer Nanofibres. *Nat. Nanotechnol.* **2008**, *3*, 614–619.
- (138) Meng, C.; Xiao, Y.; Wang, P.; Zhang, L.; Liu, Y.; Tong, L. Quantum-Dot-Doped Polymer Nanofibers for Optical Sensing. *Adv. Mater.* **2011**, *23*, 3770–3774.
- (139) Li, M.; Zhang, J.; Zhang, H.; Liu, Y.; Wang, C.; Xu, X.; Tang, Y.; Yang, B. Electrospinning: A Facile Method to Disperse Fluorescent Quantum Dots in Nanofibers without Förster Resonance Energy Transfer. *Adv. Funct. Mater.* **2007**, *17*, 3650–3656.
- (140) Camposeo, A.; Di Benedetto, F.; Stabile, R.; Cingolani, R.; Pisignano, D. Electrospun Dye-Doped Polymer Nanofibers Emitting in the near Infrared. *Appl. Phys. Lett.* **2007**, *90*, 88–91.
- (141) Fasano, V.; Polini, A.; Morello, G.; Moffa, M.; Camposeo, A.; Pisignano, D. Bright Light Emission and Waveguiding in Conjugated Polymer Nanofibers Electrospun from Organic Salt Added Solutions. *Macromolecules* **2013**, *46*, 5935–5942.
- (142) Gu, F.; Yu, H.; Wang, P.; Yang, Z.; Tong, L. Light-Emitting Polymer Single Nanofibers via Waveguiding Excitation. *ACS Nano* **2010**, *4*, 5332–5338.
- (143) Liu, H.; Edel, J. B.; Bellan, L. M.; Craighead, H. G. Electrospun Polymer Nanofibers as Subwavelength Optical Waveguides Incorporating Quantum Dots. *Small* **2006**, *2*, 495–499.
- (144) Camposeo, A.; Benedetto, F. Di; Stabile, R.; Neves, A. a R.; Cingolani, R.; Pisignano, D. Laser Emission from Electrospun Polymer Nanofibers. *Small* **2009**, *5*, 562–566.

- (145) Di Camillo, D.; Fasano, V.; Ruggieri, F.; Santucci, S.; Lozzi, L.; Campoese, A.; Pisignano, D. Near-Field Electrospinning of Light-Emitting Conjugated Polymer Nanofibers. *Nanoscale* **2013**, *5*, 11637–11642.
- (146) Slinker, J. D.; Defranco, J. A.; Verbridge, S. S.; Ilic, R.; Flores-torres, S. Electrospun Light-Emitting Nanofibers. *Nano Lett.* **2007**, *7*, 458–463.
- (147) Gu, F.; Zhang, L.; Yin, X.; Tong, L. Polymer Single-Nanowire Optical Sensors. *Nano Lett.* **2008**, *8*, 2757–2761.
- (148) Wang, P.; Zhang, L.; Xia, Y.; Tong, L.; Xu, X.; Ying, Y. Polymer Nano Fibers Embedded with Aligned Gold Nanorods: A New Platform for Plasmonic Studies and Optical Sensing. *Nano Lett.* **2012**, *8*–13.
- (149) Aslan, K.; Gryczynski, I.; Malicka, J.; Matveeva, E.; Lakowicz, J. R.; Geddes, C. D. Metal-Enhanced Fluorescence: An Emerging Tool in Biotechnology. *Curr. Opin. Biotechnol.* **2005**, *16*, 55–62.
- (150) Yang, X.; Xu, R.; Bao, D.; Li, B. Gold Nanorod-Enhanced Light Emission in Quantum-Dot-Doped Polymer Nanofibers. *ACS Appl. Mater. Interfaces* **2014**, *6*, 11846–11850.
- (151) Viste, P.; Plain, J.; Jaffiol, R.; Vial, A.; Adam, P. M.; Royer, P. Enhancement and Quenching Regimes in Metal-Semiconductor Hybrid Optical Nanosources. *ACS Nano* **2010**, *4*, 759–764.
- (152) Dulkeith, E.; Morteani, C.; Niedereichholz, T.; Klar, T. a; Feldmann, J.; Levi, S. a; van Veggel, F. C. J. M.; Reinhoudt, D. N.; Möller, M.; Gittins, D. I. Fluorescence Quenching of Dye Molecules near Gold Nanoparticles: Radiative and Nonradiative Effects. *Phys. Rev. Lett.* **2002**, *89*, 203002.
- (153) Li, S. T.; Silvers, S. J.; ElShall, M. S. Surface Oxidation and Luminescence Properties of Weblike Agglomeration of Silicon Nanocrystals Produced by a Laser Vaporization-Controlled Condensation Technique. *J. Phys. Chem. B* **1997**, *101*, 1794–1802.
- (154) Brus, L. E.; Szajowski, P. F.; Wilson, W. L.; Harris, T. D.; Schuppler, S.; Citrin, P. H. Electronic Spectroscopy and Photophysics of Si Nanocrystals: Relationship to Bulk c-Si and Porous Si. *J. Am. Chem. Soc.* **1995**, *117*, 2915–2922.
- (155) Mishima, O.; Tanaka, J.; Yamaoka, S.; Fukunaga, O. High-Temperature Cubic Boron Nitride P-N Junction Diode Made at High Pressure. *Science* **1987**, *238*,

181–183.

- (156) Kumashiro, Y. Refractory Semiconductor of Boron Phosphide. *J. Mater. Res.* **2011**, *5*, 2933–2947.
- (157) Wang, S.; Swingle, S. F.; Ye, H.; Fan, F. R. F.; Cowley, A. H.; Bard, A. J. Synthesis and Characterization of a P-Type Boron Arsenide Photoelectrode. *J. Am. Chem. Soc.* **2012**, *134*, 11056–11059.
- (158) Wettling, W.; Windscheif, J. Elastic Constants and Refractive Index of Boron Phosphide. *Solid State Commun.* **1984**, *50*, 33–34.
- (159) Popper, P.; Ingles, T. A. Boron Phosphide, a III–V Compound of Zinc-Blende Structure. *Nature* **1957**, *179*, 1075.
- (160) Shohno, K.; Takigawa, M.; Nakada, T. Epitaxial Growth of BP Compounds on Si Substrates Using the B<sub>2</sub>H<sub>6</sub>-PH<sub>3</sub>-H<sub>2</sub> System. *J. Cryst. Growth* **1974**, *24-25*, 193–196.
- (161) Kumashiro, Y.; Okada, Y.; Okumura, H. Isotope Effects on Boron Phosphide Single-Crystal Wafers. *J. Cryst. Growth* **1993**, *132*, 611–613.
- (162) Schmitt, J. O.; Edgar, L. J. H.; Liu, L.; Nagarajan, R.; Szyszko, T.; Podsiadlo, S.; Wojciech, G. Close-Spaced Crystal Growth and Characterization of BP Crystals. *Phys. Status Solidi* **2005**, *2*, 1077–1080.
- (163) Chu, T. L.; Jackson, J. M.; Smeltzer, R. K. The Crystal Growth of Boron Monophosphide from Metal Phosphide Solutions. *J. Electrochem. Soc.* **1973**, *120*, 3–5.
- (164) Chu, T. L.; Gill, M.; Smeltzer, R. K. Growth of Boron Monophosphide Crystals with the Accelerated Container Rotation Technique. *J. Cryst. Growth* **1976**, *33*, 53–57.
- (165) Kumashiro, Y.; Yao, T.; Gonda, S. Crystal Growth of Boron Phosphide by High Pressure Flux Method. *J. Cryst. Growth* **1984**, *70*, 515–518.
- (166) Schroten, E.; Goossens, a.; Schoonman, J. Photo- and Electreflectance of Cubic Boron Phosphide. *J. Appl. Phys.* **1998**, *83*, 1660.
- (167) Yugo, S.; Sato, T.; Kimura, T. Thermoelectric Figure of Merit of Boron Phosphide. *Appl. Phys. Lett.* **1985**, *46*, 842.
- (168) Fan, F.-J.; Wang, Y.-X.; Liu, X.-J.; Wu, L.; Yu, S.-H. Large-Scale Colloidal Synthesis of Non-Stoichiometric Cu<sub>2</sub>ZnSnSe<sub>4</sub> Nanocrystals for

- Thermoelectric Applications. *Adv. Mater.* **2012**, *24*, 6158–6163.
- (169) Chen, L.; Gu, Y.; Shi, L.; Ma, J.; Yang, Z.; Qian, Y. A Convenient Low-Temperature Route to Nanocrystalline Boron Phosphide. *Chem. Lett.* **2003**, *32*, 1188–1189.
- (170) Gu, Y.; Zheng, H.; Guo, F.; Qian, Y.; Yang, Z. A Benzene-Thermal Synthesis of Cubic Boron Phosphide (BP) Ultrafine Powders. *Chem. Lett.* **2002**, 724–724.
- (171) Feng, X.; Shi, L.-Y.; Hang, J.-Z.; Zhang, J.-P.; Fang, J.-H.; Zhong, Q.-D. Low Temperature Synthesis of Boron Phosphide Nanocrystals. *Mater. Lett.* **2005**, *59*, 865–867.
- (172) Durrani, S. M. A.; Al-Kuhaili, M. F.; Khawaja, E. E. Characterization of Thin Films of  $\alpha$ -SiO<sub>x</sub> ( $1.1 < x < 2.0$ ) Prepared by Reactive Evaporation of. *J. Phys. Condens. Matter* **2003**, *15*, 8123–8135.
- (173) Metwalli, E.; Karabulut, M.; Sidebottom, D. L.; Morsi, M. M.; Brow, R. K. Properties and Structure of Copper Ultraphosphate Glasses. *J. Non. Cryst. Solids* **2004**, *344*, 128–134.
- (174) Liu, H. S.; Chin, T. S.; Yung, S. W. FTIR and XPS Studies of Low-Melting PbO-ZnO-P2O5 Glasses. *Mater. Chem. Phys.* **1997**, *50*, 1–10.
- (175) Sanjurjo, A.; Lopez-Cruz, E.; Vogl, P.; Cardona, M. Dependence on Volume of the Phonon Frequencies and the Ir Effective Charges of Several III-V Semiconductors. *Phys. Rev. B* **1983**, *28*, 4579–4584.
- (176) Tallant, D. R.; Aselage, T. L.; Campbell, A. N.; Emin, D. Boron Carbide Structure by Raman Spectroscopy. *Phys. Rev. B* **1989**, *40*, 5649–5656.
- (177) Nesheva, D.; Raptis, C.; Perakis, S.; Bineva, I.; Aneva, Z.; Levi, Z.; Alexandrova, S.; Hofmeister, H. Raman Scattering and Photoluminescence from Si Nanoparticles in Annealed SiO<sub>x</sub> Thin Films. *J. Appl. Phys.* **2002**, *92*, 4678.
- (178) Hayashi, S.; Nagareda, T.; Kanzawa, Y.; Yamamoto, K. Photoluminescence of Si-Rich SiO<sub>2</sub> Films: Si Clusters as Luminescent Centers. *Jpn. J. Appl. Phys.* **1993**, *32*, 3840.
- (179) Kanzawa, Y.; Kageyama, T.; Takeoka, S.; Fujii, M.; Hayashi, S.; Yamamoto, K. Size-Dependent near-Infrared Photoluminescence Spectra of Si Nanocrystals Embedded in SiO<sub>2</sub> Matrices. *Solid State Commun.* **1997**, *102*, 533–537.
- (180) Scamarcio, G.; Lugara, M. Size-Dependent Lattice Contraction in CdS<sub>1-x</sub>Se

- Nanocrystals Embedded in Glass Observed by Raman Scattering Gaetano. *Phys. Rev. B* **1992**, *45*, 792–795.
- (181) Hessel, C. M.; Wei, J.; Reid, D.; Fujii, H.; Downer, M. C.; Korgel, B. a. Raman Spectroscopy of Oxide-Embedded and Ligand-Stabilized Silicon Nanocrystals. *J. Phys. Chem. Lett.* **2012**, *3*, 1089–1093.
- (182) Archer, R. J.; Koyama, R. Y.; Loebner, E. E.; Lucas, R. C. OPTICAL ABSORPTION, ELECTROLUMINESCENCE, AND THE BAND GAP OF BP. *Phys. Rev. Lett.* **1964**, *12*, 11–13.
- (183) Wang, C. C.; Cardona, M.; Fischer, A. G. Preparation, Optical Properties, and Band Structure of Boron Monophosphide. *RCA Rev.* **1964**, *XXV*, 159.
- (184) Sugimoto, H.; Fujii, M.; Imakita, K. Synthesis of Boron and Phosphorus Codoped All-Inorganic Colloidal Silicon Nanocrystals from Hydrogen Silsesquioxane. *Nanoscale* **2014**, *6*, 12354–12359.
- (185) Barth, R. F.; H Vicente, M. G.; Harling, O. K.; Kiger, W.; Riley, K. J.; Binns, P. J.; Wagner, F. M.; Suzuki, M.; Aihara, T.; Kato, I.; *et al.* Current Status of Boron Neutron Capture Therapy of High Grade Gliomas and Recurrent Head and Neck Cancer. *Radiat. Oncol.* **2012**, *7*, 146.
- (186) Barth, R. F. A Critical Assessment of Boron Neutron Capture Therapy: An Overview. *J. Neurooncol.* **2003**, *62*, 1–5.
- (187) Barth, R. F. Boron Neutron Capture Therapy at the Crossroads: Challenges and Opportunities. *Appl. Radiat. Isot.* **2009**, *67*, 67–70.
- (188) Soloway, A. H.; Others. The Chemistry of Neutron Capture Therapy. *Chem. Rev.* **1998**, *98*, 1515–1562.
- (189) Barth, R. F.; Soloway, A. H.; Goodman, J. H.; Gahbauer, R. A.; Gupta, N.; Blue, T. E.; Yang, W.; Tjarks, W. Boron Neutron Capture Therapy of Brain Tumors: An Emerging Therapeutic Modality. *Neurosurgery* **1999**, *44*, 433–450.
- (190) Maruyama, K.; Ishida, O.; Kasaoka, S.; Takizawa, T.; Utoguchi, N.; Shinohara, A.; Chiba, M.; Kobayashi, H.; Eriguchi, M.; Yanagie, H. Intracellular Targeting of Sodium Mercaptoundecahydrododecaborate (BSH) to Solid Tumors by Transferrin-PEG Liposomes, for Boron Neutron-Capture Therapy (BNCT). *J. Control. Release* **2004**, *98*, 195–207.
- (191) Kabalka, G. W.; Smith, G. T.; Dyke, J. P.; Reid, W. S.; Longford, C. P.; Roberts, T.

- G.; Reddy, N. K.; Buonocore, E.; Hübner, K. F. Evaluation of Fluorine-18-BPA-Fructose for Boron Neutron Capture Treatment Planning. *J. Nucl. Med.* **1997**, *38*, 1762–1767.
- (192) Irvine, D. J. Drug Delivery: One Nanoparticle, One Kill. *Nat. Mater.* **2011**, *10*, 342–343.
- (193) Anker, J. N.; Hall, W. P.; Lyandres, O.; Shah, N. C.; Zhao, J.; Van Duyne, R. P. Biosensing with Plasmonic Nanosensors. *Nat. Mater.* **2008**, *7*, 442–453.
- (194) Smith, A. M.; Mancini, M. C.; Nie, S. Bioimaging: Second Window for in Vivo Imaging. *Nat. Nanotechnol.* **2009**, *4*, 710–711.
- (195) Lee, J. E.; Lee, N.; Kim, H.; Kim, J. H. J. H.; Choi, S. H.; Kim, T.; Song, I. C.; Park, S. P.; Moon, W. K.; Hyeon, T. Uniform Mesoporous Dye-Doped Silica Nanocrystals for Simultaneous Enhanced Magnetic Resonance Imaging, Fluorescence Imaging, and Drug Delivery. *J. Am. Chem. Soc.* **2010**, *132*, 552–557.
- (196) Chen, G.; Yang, J.; Lu, G.; Liu, P. C.; Chen, Q.; Xie, Z.; Wu, C. One Stone Kills Three Birds: Novel Boron-Containing Vesicles for Potential BNCT, Controlled Drug Release, and Diagnostic Imaging. *Mol. Pharm.* **2014**, *11*, 3291–3299.
- (197) Grandi, S.; Spinella, a.; Tomasi, C.; Bruni, G.; Fagnoni, M.; Merli, D.; Mustarelli, P.; Guidetti, G. F.; Achilli, C.; Balduini, C. Synthesis and Characterisation of Functionalized Borosilicate Nanoparticles for Boron Neutron Capture Therapy Applications. *J. Sol-Gel Sci. Technol.* **2012**, *64*, 358–366.
- (198) Mortensen, M. W.; Sørensen, P. G.; Björkdahl, O.; Jensen, M. R.; Gundersen, H. J. G.; Bjørnholm, T. Preparation and Characterization of Boron Carbide Nanoparticles for Use as a Novel Agent in T Cell-Guided Boron Neutron Capture Therapy. *Appl. Radiat. Isot.* **2006**, *64*, 315–324.
- (199) Achilli, C.; Grandi, S.; Ciana, A.; Guidetti, G. F.; Malara, A.; Abbonante, V.; Cansolino, L.; Tomasi, C.; Balduini, A.; Fagnoni, M.; *et al.* Biocompatibility of Functionalized Boron Phosphate (BPO<sub>4</sub>) Nanoparticles for Boron Neutron Capture Therapy (BNCT) Application. *Nanomedicine Nanotechnology, Biol. Med.* **2014**, *10*, 589–597.
- (200) Sugimoto, H.; Fujii, M.; Imakita, K. Size-Controlled Growth of Cubic Boron Phosphide Nanocrystals. *RSC Adv.* **2015**, *5*, 8427–8431.
- (201) Tsutsui, K.; Matsuda, T.; Watanabe, M.; Jin, C.-G.; Sasaki, Y.; Mizuno, B.;

- Ikenaga, E.; Kakushima, K.; Ahmet, P.; Maruizumi, T.; *et al.* Activated Boron and Its Concentration Profiles in Heavily Doped Si Studied by Soft X-Ray Photoelectron Spectroscopy and Hall Measurements. *J. Appl. Phys.* **2008**, *104*, 093709.
- (202) Soraru, G. D.; Babonneau, F.; Gervais, C. Hybrid  $\text{RSiO}_{1.5} / \text{B}_2\text{O}_3$  Gels from Modified Silicon Alkoxides and Boric Acid. *J. Sol-Gel Sci. Technol.* **2000**, *18*, 11–19.
- (203) Soraru, G. D.; Dallabona, N.; Gervais, C.; Babonneau, F. Organically Modified  $\text{SiO}_2\text{-B}_2\text{O}_3$  Gels Displaying a High Content of Borosiloxane (= B-O-Si ) Bonds. *Chem. Mater.* **1999**, *11*, 910–919.
- (204) Hyam, R. S.; Subhedar, K. M.; Pawar, S. H. Effect of Particle Size Distribution and Zeta Potential on the Electrophoretic Deposition of Boron Films. *Colloids Surfaces A Physicochem. Eng. Asp.* **2008**, *315*, 61–65.
- (205) Dasog, M.; De los Reyes, G. B.; Titova, L. V.; Hegmann, F. A.; Veinot, J. G. C. Size vs Surface: Tuning the Photoluminescence of Freestanding Silicon Nanocrystals Across the Visible Spectrum via Surface Groups. *ACS Nano* **2014**, *8*, 9636–9648.
- (206) Montalti, M.; Cantelli, a.; Battistelli, G. Nanodiamonds and Silicon Quantum Dots: Ultrastable and Biocompatible Luminescent Nanoprobes for Long-Term Bioimaging. *Chem. Soc. Rev.* **2015**, *44*, 4853–4921.
- (207) Shubina, E. S.; Bakhmutova, E. V.; Filin, a M.; Sivaev, I. B.; Teplitskaya, L. N.; Chistyakov, a L.; Stankevich, I. V.; Bakhmutov, V. I.; Bregadze, V. I.; Epstein, L. M. Dihydrogen Bonding of Decahydro-Closo-Decaborate (2-) and Dodecahydro-Closo-Dodecaborate (2-) Anions with Proton Donors: Experimental and Theoretical Investigation. *J. Organomet. Chem.* **2002**, *657*, 155–162.
- (208) Tague, T. J.; Andrews, L. Reactions of Pulsed-Laser Evaporated Boron Atoms with Hydrogen - Infrared-Spectra of Boron Hydride Intermediate Species in Solid Argon. *J Am Chem Soc* **1994**, *116*, 4970–4976.
- (209) Pearson, G. L.; Bardeen, J. Electrical Properties of Pure Silicon and Silicon Alloys Containing Boron and Phosphorus. *Phys. Rev.* **1949**, *75*, 865–883.
- (210) Khelifi, R.; Mathiot, D.; Gupta, R.; Muller, D.; Roussel, M.; Duguay, S. Efficient N-Type Doping of Si Nanocrystals Embedded in  $\text{SiO}_2$  by Ion Beam Synthesis. *Appl. Phys. Lett.* **2013**, *102*, 013116.

- (211) Valenta, J.; Juhasz, R.; Linnros, J. Photoluminescence Spectroscopy of Single Silicon Quantum Dots. *Appl. Phys. Lett.* **2002**, *80*, 1070.
- (212) Ciraci, C.; Hill, R. T.; Mock, J. J.; Urzhumov, Y.; Fernandez-Dominguez, A. I.; Maier, S. A.; Pendry, J. B.; Chilkoti, A.; Smith, D. R. Probing the Ultimate Limits of Plasmonic Enhancement. *Science* **2012**, *337*, 1072–1074.



# List of Achievements

## Journal Papers

\*Papers relevant to this thesis

- [1] Hiroshi Sugimoto, Minoru Fujii, Masatoshi Fukuda, Kenji Imakita, and Shinji Hayashi,  
"Acceptor-related low-energy photoluminescence from boron-doped Si nanocrystals"  
Journal of Applied Physics, Vol. 110, 063528, pp. 1–6 (2011)
- [2] Masatoshi Fukuda, Hiroshi Sugimoto, Minoru Fujii, Kenji Imakita, and Shinji Hayashi,  
"Surfactant-free solution-dispersible Si nanocrystals -surface modification by impurity control"  
Optics Letters, Vol. 36, No. 20, pp. 4014–4016 (2011).
- [3] \*Hiroshi Sugimoto, Minoru Fujii, Kenji Imakita, Shinji Hayashi, and Kensuke Akamatsu,  
"All-Inorganic Near-Infrared Luminescent Colloidal Silicon Nanocrystals -High Dispersibility in Polar Liquid by Phosphorus and Boron Codoping"  
The Journal of Physical Chemistry C, Vol. 116, pp. 17969–17975 (2012).  
(Chapter 2)
- [4] \*Hiroshi Sugimoto, Minoru Fujii, Kenji Imakita, Shinji Hayashi, and Kensuke Akamatsu,  
"Phosphorus and Boron Codoped Colloidal Silicon Nanocrystals with Inorganic Ligands"

The Journal of Physical Chemistry C, Vol. 117, No. 13, pp. 6807–6813 (2013).  
(Chapter 2)

- [5] \*Hiroshi Sugimoto, Minoru Fujii, Kenji Imakita, Shinji Hayashi, and Kensuke Akamatsu

"Codoping n- and p-Type Impurities in Colloidal Silicon Nanocrystals -Controlling Luminescence Energy from below Bulk Band Gap to Visible Range"

The Journal of Physical Chemistry C, Vol. 117, No. 22, pp. 11850–11857 (2013).  
(Chapter 2)

- [6] \*Hiroshi Sugimoto, Minoru Fujii, Yuki Fukuda, Kenji Imakita, and Kensuke Akamatsu

"All-Inorganic Water-Dispersible Silicon Quantum Dots: Highly Efficient Near-Infrared Luminescence in a Wide pH Range"

Nanoscale, Vol. 6, Issue 1, pp. 122–126 (2014).  
(Chapter 4)

- [7] \*Minoru Fujii, Hiroshi Sugimoto, Masataka Hasegawa and Kenji Imakita  
"Silicon Nanocrystals with High Boron and Phosphorus Concentration Hydrophilic Shell -Raman Scattering and X-Ray Photoelectron Spectroscopic Studies"

Journal of Applied Physics, Vol. 115, pp. 084301 (2014).  
(Chapter 2)

- [8] Takashi Kanno, Minoru Fujii, Hiroshi Sugimoto, and Kenji Imakita,  
"Colloidal Silicon Germanium Alloy Nanocrystals with High Boron and Phosphorus Concentration Hydrophilic Shell",

Journal of Materials Chemistry C, Vol. 2, Issue 28, pp. 5644–5650 (2014).

- [9] \*Hiroshi Sugimoto, Kenji Imakita, Minoru Fujii

"Synthesis of Boron and Phosphorus Codoped All-Inorganic Colloidal Silicon Nanocrystals from Hydrogen Silsesquioxane"

Nanoscale, Vol. 6, Issue 6, pp. 12354–12359 (2014).

(Chapter 3)

- [10] \*Hiroshi Sugimoto, Kenji Imakita, Minoru Fujii

"Size-Controlled Growth of Cubic Boron Phosphide Nanocrystals"

RSC Advances, Vol. 5, Issue 11, pp. 8427–8431 (2015).

(Chapter 7)

- [11] Toshihiro Nakamura, Sadao Adachi, Minoru Fujii, Hiroshi Sugimoto, K. Miura and S. Yamamoto

"Size and dopant-concentration dependence of photoluminescence properties of ion-implanted phosphorus- and boron-codoped Si nanocrystal"

Physical Review B, Vol. 91, Issue 16, pp. 165424 (2015).

- [12] Yu Wang, Hiroshi Sugimoto, Sandeep Inampudi, Antonio Capretti, Minoru Fujii, and Luca Dal Negro

"Broadband enhancement of local density of states using silicon-compatible hyperbolic metamaterials"

Applied Physics Letters, Vol. 106, Issue 24, pp. 241105 (2015).

- [13] Kenta Furuta, Minoru Fujii, Hiroshi Sugimoto, and Kenji Imakita

"Energy Transfer in Silicon Nanocrystal Solids Made from All-Inorganic Colloidal Silicon Nanocrystals"

The Journal of Physical Chemistry Letters, Vol. 6, Issue 14, pp. 2761–2766 (2015).

- [14] Hiroshi Sugimoto, Tianhong Chen, Ren Wang, Minoru Fujii, Bejoern M. Reinhard, Luca Dal Negro

"Plasmon-Enhanced Emission Rate of Silicon Nanocrystals in Gold Nanorod Composites"

ACS Photonics, Vol. 2, Issue 9, pp. 1298–1305 (2015).

- [15] Hiroshi Sugimoto, Ran Zhang, Bjoern M. Reinhard, Minoru Fujii, Giovanni Perott , Benedetto Marelli, Fiorenzo G. Omenetto, Luca Dal Negro  
"Enhanced photoluminescence of Si nanocrystals-doped cellulose nanofibers by plasmonic light scattering"  
Applied Physics Letters, Vol. 107, Issue 4, pp. 041111 (2015).
- [16] Asuka Inoue, Minoru Fujii, Hiroshi Sugimoto, Kenji Imakita  
"Surface Plasmon-Enhanced Luminescence of Silicon Quantum Dots in Gold Nanoparticle Composites"  
The Journal of Physical Chemistry C. Vol. 119, Issue 44, pp. 25108–25113 (2015)
- [17] \*Hiroshi Sugimoto, Kenji Imakita, Minoru Fujii  
"Growth of Novel Boron-Rich Nanocrystals from Oxygen-Deficient Borophosphosilicate Glasses for Boron Neutron Capture Therapy"  
RSC Advances, Vol. 5, Issue 119, pp. 98248–98253 (2015)  
(Chapter 8)
- [18] Masato Sasaki, Shinya Kano, Hiroshi Sugimoto, Kenji Imakita, and Minoru Fujii  
"Surface Structure and Current Transport Property of Boron and Phosphorous Co-doped Silicon Nanocrystals"  
The Journal of Physical Chemistry C, Vol. 120, Issue 1, pp 195–200 (2016)

## International Conferences

- [1] Hiroshi Sugimoto, Minoru Fujii, Masatoshi Fukuda, Kenji Imakita and Shinji Hayashi,  
"Surfactant-free Silicon Nanocrystal Colloids -Controlling Dispersibility of Silicon Nanocrystals in Polar Liquids by Impurity Doping"  
2012 Materials Research Society Spring Meeting, April 9-13, 2012, Moscone West Convention Center, San Francisco, California (USA), Oral Presentation
  
- [2] **(Best Poster Paper Award)** Hiroshi Sugimoto, Minoru Fujii, Kenji Imakita, and Shinji Hayashi,  
"Photoluminescence Properties of Phosphorus and Boron Codoped Silicon Quantum Dots dispersed in solution"  
Fifth International Conference on Optical, Optoelectronic and Photonic Materials and Applications 2012, June 3-7, 2012, Nara (Japan), Poster Presentation
  
- [3] Hiroshi Sugimoto, Minoru Fujii, Masataka Hasegawa, Hiroki Shibata, Kenji Imakita and Shinji Hayashi,  
"Near-infrared Luminescent Colloidal Silicon Nanocrystals"  
Asia Student Photonics Conference, September 15-16, Osaka University Photonics Center, Poster Presentation
  
- [4] Hiroshi Sugimoto, Yuki Fukuda, Minoru Fujii, Kenji Imakita, Shinji Hayashi, and Kensuke Akamatsu,  
"Near-infrared luminescent silicon nanocrystals dispersible in water without surface functionalization"  
European Materials Research Society 2013 Spring Meeting, May 26-31, 2013, Strasbourg (France), Poster Presentation
  
- [5] **(Young Scientist Award)** Hiroshi Sugimoto, Minoru Fujii, Kenji Imakita, Shinji Hayashi and Kensuke Akamatsu,

"Colloidal silicon nanocrystals with inorganic atomic ligands" European Materials Research Society 2013 Spring Meeting, May 26-31, 2013, Strasbourg (France), Oral Presentation

- [6] Hiroshi Sugimoto, Minoru Fujii, Masataka Hasegawa, Kenji Imakita and Kensuke Akamatsu,  
"All-Inorganic Colloidal Silicon Nanocrystals-Surface Modification by Heavy Doping of Boron and Phosphorus",  
2014 Materials Research Society Spring Meeting, April 21-25 (2014), San Francisco, California (USA), Oral Presentation
- [7] Hiroshi Sugimoto, Minoru Fujii, Kenji Imakita and Kensuke Akamatsu,  
"Controlling HOMO-LUMO Gap of Colloidal Silicon Nanocrystals in a Wide Range by n- and p-Type Impurity Codoping"  
Materials Research Society 2014 Spring Meeting, April 21-25 (2014), San Francisco, California (USA), Poster Presentation
- [8] Hiroshi Sugimoto, Kenji Imakita, and Minoru Fujii,  
"Synthesis of n- and/or p-type Impurity Doped Silicon Nanocrystals from Hydrogen Silsesquioxane"  
Materials Research Society 2014 Fall Meeting, November 30-December 5 (2014), Boston, Massachusetts (USA), Poster Presentation

## Patent

「ホウ素－リン－シリコンの三元系化合物ナノ結晶、その製造方法及びそれを用いた中性子捕獲療法用材料」特願 2015－210468  
発明者：杉本 泰／藤井 稔／今北 健二 2015 年 10 月

## Award

- [1] シリコンフォトニクス研究会, 2011 年 11 月 25 日 電気通信大学  
最優秀ポスター賞
  
- [2] Fifth International Conference on Optical, Optoelectronic and Photonic Materials  
and Applications 2012 (ICOOPMA2012), June 3-7, 2012,  
Best Poster Paper Award
  
- [3] European Materials Research Society, 2013 Spring Meeting, May 26-31, 2013  
Symposium D: Advanced Inorganic Materials and Structures for Photovoltaics,  
Young Scientist Award
  
- [4] 神戸大学学生表彰, 平成 26 年度 学術研究部門, 2013 年 3 月 17 日
  
- [5] The Materials Research Society of Japan, 第 23 回日本 MRS 年次大会 2013 年 12  
月 9 日～11 日  
Award of Encourage of Research in Material Science
  
- [6] 神戸大学工学研究科海外派遣制度プレミアムプログラム, 2015 年 9 月  
Outstanding Student Award

## Acknowledgements

I am deeply indebted to my advisor Prof. Minoru Fujii for his continuous supports and guidance throughout the course of my doctoral research. I also thank him for giving me the opportunity to work on such a fascinating material, and turning me into a successful scientist. These experiences I had in his group these five years were invaluable to expand my knowledge into many different areas.

I would like to express my sincerest gratitude Prof. Shinji Hayashi for his support and deep knowledge in the research topic. I learned noble and generous spirits indispensable for research activities. I would also like to thank Prof. Kenji Imakita for his valuable advice and great encouragement in this work. Great scientific and insightful conversations with them made a profound impact on my growth and development as a scientist.

It is my pleasure to acknowledge the contributions of my collaborators all over the world, Prof. Kensuke Akamatsu at Konan University for chemical analysis of silicon nanomaterials, and Prof. Luca Dal Negro, Prof. Björn M. Reinhard and their students at Boston University for the study of plasmonic-coupled silicon based composites. I also thank the all co-authors in the paper regarding this thesis.

I would also gratefully thank all professors and colleagues in the Mesoscopic Material Laboratory, Dr. Shinya Kano, Dr. Kanna Aoki, and the students involved in the project of colloidal Si nanocrystals. In particular, I would like to thank the colleagues who are co-authored in journal articles, Mr. Masatoshi Fukuda, Masataka



Hasegawa, Takashi Kanno, Yuki Fukuda, Kenta Furuta, Masato Sasaki and Asuka Inoue.

Finally, I'm indebted to my family and all my friends for all their hearty support and enjoyable daily life.

Doctor Dissertation, Kobe University

“Engineering Novel Silicon-Based Functional Nanomaterials”

(シリコンベース機能性ナノ材料の開発に関する研究), 167 pages

Submitted on January, 19, 2016

The date of publication is printed in cover of repository version published in Kobe University Repository Kernel.

© Hiroshi Sugimoto  
All Right Reserved, 2016